POLITECNICO DI MILANO

Facoltà di Ingegneria Industriale

Dipartimento di Ingegneria Aerospaziale

TECHNOLOGY FOR ADVANCED MORPHING STRUCTURES

Mehmet Fatih Oktem

Tesi di Dottorato di Ricerca in Aerospaziale

– Ciclo XXV –

POLITECNICO DI MILANO

Dipartimento di Ingegneria Aerospaziale

Via La Masa, 34 – 20158 Milano (MI)

DOTTORATO DI RICERCA IN INGEGNERIA AEROSPAZIALE

Ciclo XXV

Coordinatore del Corso di Dottorato di Ricerca

Prof. Sergio RICCI

Relatore della Ricerca

Prof. Giuseppe SALA

Tesi presentata da

Mehmet Fatih OKTEM

Matricola: 754279

Per il conseguimento del titolo di Dottore di Ricerca

Milano, January 2013

Acknowledgements

I do believe that without the help of God, I could not have completed this thesis. I praise to him for everything that he gives me. I would like to thank to Prof. Sala as my advisor. Special thanks go to Dr. Airoldi and Dr. Bettini for their support and help. I would like to thank to the PhD School of Politecnico di Milano for their financial support during my PhD studies.
My sincere gratitude goes to my colleagues in the office for their close friendship in my three years of study. I experienced great aid from the lab workers that assisted me during the lab work I carried out.

First of all, this thesis is dedicated to my family for their encouragement and moral support which gave me courage to complete my studies.

Contents

List of Figures

List of Tables

Abstract

The objective of the morphing concept is to provide continuous controllable deformations thus changing the stiffness of the structure. A possible solution to design morphing structure can exploit the peculiar characteristics of chiral topologies, which are a relatively new design concept for composite aerospace materials. A honeycomb based on a chiral topology shows auxetic features which leads to negative Poisson coefficients

This thesis investigates the design of a technological demonstrator of a morphing wing that uses the auxetic features of chiral cells. The research is concentrating on the manufacturing of the chiral composite cell network inside a rib. The design of the technological demonstrator is composed of two ribs connected to each other by means of corrugated flexible skin. The Leading edge (LE) and Trailing Edge (TE) provide housing for two ribs. The ribs are connected to the corrugated flexible skin by means of pin – hinge mechanisms. LE and TE are filled with a foam material to provide shear and pressure resistance. The foam material thought to be utilized is Rohacell and this material offers high strength/weight ratio.

The morphing wing has the property of increasing the camber when subjected to a gust load. The aeroelastic performances have been studied in previous works, where the topology of the chiral honeycomb has been optimized. Basing on the knowledge of the aerodynamic loads this study presents the basic aspects of the technological solutions and the development of the structural design of the demonstrator. The manufacturing of the ligaments and assembly of these specific parts to form chiral cells are described. Finite element analyses are carried out based to verify the rib design and choose the best configuration. Experiments are also performed to validate the design and to verify the manufacturing techniques. The manufacturing phase started from the production of the ligaments and then assembling them in the assembly mold. The experiments were carried out on four chiral unit cells. This phase also includes the design and manufacturing of the molds of the ligaments which are used for the production of the chiral unit cells and rib. Another mold was also designed and produced for the assembly of the ligaments to form the chiral unit cell.

The production of the rib started after the exploitation of the chiral unit cells was proven. The previous production phase also gave some hints on how to proceed for the assembly of the full rib which is composed of up to three hundred ligaments. Compared with the chiral unit cell, a full rib is relatively a more complex structure and more attention is needed for the assembly of the ligaments to create defect free structure. After the production phase is completed static testing was performed on the rib. That was realized by suspending loads to the nodes of the rib and measuring the deflection by means of laser and comparator.

The recent technological demonstrator is designed as a passive structure but the next step of this research could employ the use of sensing elements and actuators to create a controllable aerodynamic surfaces. The researcher also investigated the possible use of sensing elements and polymeric materials that could change their shape under several stimulus effects. The best polymeric material to be utilized should include both the shape memory effect and self healing effect.

1 Outline of the Research

1.1 Introduction

Composite materials are becoming more common due to some advantages e.g. low weight, higher stiffness, high strength and so on. These properties provide great advantages in particular to aerospace and aeronautics industry. Design approaches and innovation of novel materials are influencing the performances of the aerospace systems. New solutions in structure can lead to decrease in operating costs by reducing the weight.

Several flight regimes occur during a typical aircraft mission so it is practically impossible to define a single configuration able to maximize aerodynamic efficiency, maneuverability, stability and fuel consumption in any circumstance. An aircraft is supposed to adapt its shape to distinct flight conditions thus able to change its shape by means of morphing from one flight mode to another. This concept is provided by continuous controllable deformations which takes its inspiration from nature.

An aircraft structure (either wing or other structural part) can be defined as morphing when it can change its shape and size during flight. Morphing structures can eliminate the need for flap type mechanisms and reduce aerodynamic drag. The objective of the morphing concept is to provide continuous controllable deformations thus changing the rigidity (stiffness) of the structure.

Chiral cells are relatively new design concept for composite aerospace materials. Chiral honeycomb composite structures can find their applications in the morphing of the aircraft structures such as airfoils. Chiral topology brings a new vision by combining the advantages of honeycomb lightweightness and flexibility of chiral structures. The final goals of the morphing concept are to increase the aerodynamic loads and extend the operative mission.

Research on auxetic chiral cells started in 2007 by researchers in Politecnico di Milano. Several attempts have been made to create a single unit cell to show the capability of the morphing cell topology. The first cells were relatively bigger and were not convenient to use in a rib so the topological optimization was initiated .The optimization process has been carried out by using several parameters to maximize C_L /α. Three points should be guaranteed during the optimization process:

- Aeroelasticity of the airfoil for the required stiffness
- Aerodynamic loads to ensure the performance of the airfoil
- Strength of the whole structure

The optimization process gave the following results:

- Four geometrical parameters of the rib were optimized. The locations of leading and trailing edge spars, the points on the leading edge and trailing edge spars where these points will be used as reference points for constraints.
- Two geometrical parameters of the chiral topology were optimized. The radius of a node and the length of ligament between two tangential points.
- Two parameters regarding the number of plies for the skin and ligaments were also optimized. Thus this gives the thickness of the ligament and CFRP (Carbon Fiber Reinforced Plastics) skin.

The composites differ from the metals in terms of the way they are manufactured. First of all they are not in their final forms for production. They need to be “processed”. The manufacturing technique for the production of the composite chiral cells is based on vacuum bagging with prepreg material. This method simplifies the overall manufacturing process for relatively low number of parts to be produced.

1.2 Final Objective: Technological Demonstrator

As already mentioned the final objective of the research is to design/manufacture and test the technological demonstrator in the wind tunnel which has two ribs connected to each other by means of corrugated flexible skin. The outer nodes of a rib are connected to the corrugated skin by using pin-hinge mechanism. LE and TE are filled with a foam material called Rohacell and this light core material which is a closed sandwich structure that provides shear and pressure resistance. Rohacell offers high strength/weight ratio. The desired aerodynamic surface can be generated with the utilization of Rohacell.
In order to reach the desired goal, three points have been identified:

- Technology for chiral cell and rib
- Numerical activities
- Design and technology of rib and skin

These three points will be detailed in the next chapter of the thesis. The Figure 1.1 shows the FE model of two rib technological demonstrator with ribs attached to the LE and TE and covered with the skin.

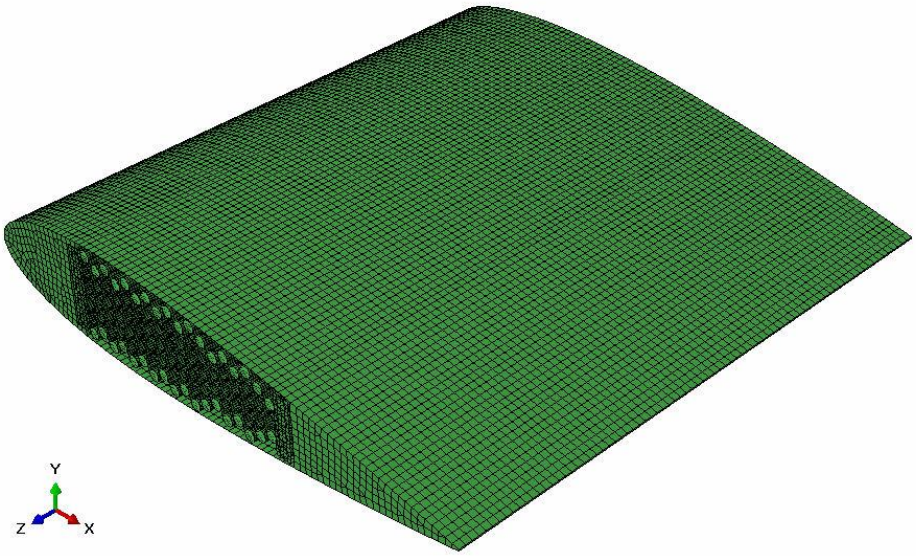

Figure 1.1 – FE Model of the 3-D demonstrator

1.3 Tools of the Project

Three important steps exist to carry out the desired goal. These steps interact with each other in terms of technological and numerical activities. These steps can be listed as below:

- Technology for the chiral cell and the rib
- Numerical activities
- Design and technology of the rib and the skin

The technological achievement of the rib was initiated by the production of the chiral unit cell. The production phase first started with the manufacturing of the ligaments needed to form a chiral unit cell. After this step was achieved, the miniaturized unit cell structure enabled to work on the bigger part which is the rib. The rib consists of several auxetic chiral cells that are connected to each other in the same structure. Numerical activities were initiated for the Finite Element Analysis (FEA) for the 2-D airfoil strip to assess the displacements and stress levels that are generated on the rib. The connection of the rib to the deformable flexible skin takes into account of the realization of the wave like corrugated structure and an elastomeric silicon rubber with stiffeners inside.

1.3.1 Technology for the Chiral Unit and Rib

Based on the previous experience, the exact manufacturing capability for the chiral unit is existed. The manufacturing technique is called vacuum bagging with prepreg material. The preimpregnated materials or prepreg materials as they are often called – fiber reinforcement preimpregnated with uncured resin - are widely used for the manufacture of composite material components. Current commercially available prepreg materials often show significant variations in adhesive strength [1]. Such inconsistencies can lead to void formation in the final composites laminate. In order to avoid possible voids vacuum bagging and flexible counter mold are utilized.
LE and TE will provide housing for the ribs that contain chiral geometries. Inside the LE and TE boxes, foam like material that is already mentioned will be utilized to prevent shear and pressure. The Figure 1.2 indicates the technological demonstrator with two ribs; the skin is not shown in order to specify the rib geometry.

1.3.2 Numerical Activities

Finite element analyses are needed to verify and to modify the model. Matlab was used to optimize the rib and chiral cell topology and also the number of plies to be used for the ligament/ skin in a previous research. Abaqus CAE was realized for the FEA of the rib, (3-D demonstrator) and for the testing of the unit cell. FE analyses are based on static linear and aerodynamic forces. The aerodynamic forces are based on the reality that the capacity of the wind tunnel in which the technological demonstrator is supposed to be tested has a velocity of 50 m/s. Several difficulties were encountered when FE model was constructed. They generate discrepancies between the real model and the FE model. The geometrical nonlinearities that cause discrepancies will be detailed in the coming chapters.

1.3.3 Design and Technology of Rib and Skin

Flexible skin is needed to ensure the stiffness of the structure. The outer nodes are connected to the corrugated skin through a pin-hinge mechanism. On the top of the corrugated skin, there is an elastomeric silicon rubber with stiffeners inside. This configuration will ensure the proper working of the chiral cells by giving the necessary rigidity. In the future configuration however, the corrugated skin will be eliminated and pre – stressed, stiffeners embedded elastomeric skin will be the sole skin solution. The skin will be connected to the chiral cells by linking the nodes on the leading and trailing edge sections to the respected spars.

1.4 Future Goals

The recent research is based on the realization of a passive morphing wing, no active control is proposed. Several researchers around the globe are trying to find a way to employ active control techniques to gain control on the aerodynamic surface of the wing. Some of the active morphing technologies are using chordwise deflection technique while some are using spanwise deflection technique. Polymeric materials like Shape Memory Polymers (SMP) or Electro Active Polymers (EAP) are now utilized as the actuators. More attention is also needed for the sensing part of the active morphing wing. The chiral geometry brings some difficulties in the application of fiber optics since the geometry is more complex than a flat plate and the thickness is relatively thin compared with the conventional composite parts.

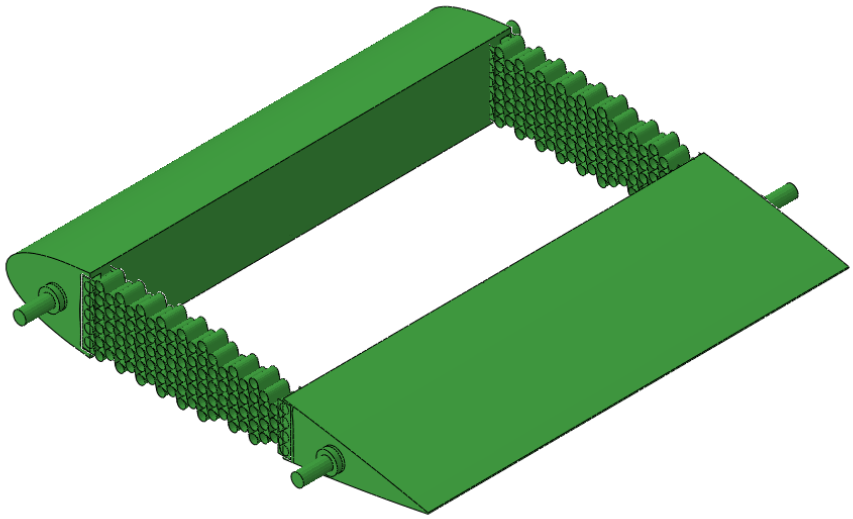

Figure 1.2 – Technological demonstrator with two ribs

1.4.1 Sensing by Fiber Optics

Monitoring structures with embedded Fiber – Optic Sensors (FOS) has found use in various applications, ranging from rotor blades of wind turbines to airplane and spacecraft structures. Such monitoring has multiple objectives, which include: observing manufacturing processes, especially curing (cross-linking of polymer chains) in fiber composite materials; structural testing prior to operation; or monitoring structural health and conditions during operation [2].
Sensing techniques such as those that use fiber Bragg gratings (FBGs) allow the strain and temperature at many points along a single optical fiber to be measured, opening up the possibility of extensive FOS networks. Via proper transfer matrices, these networks produce measured discrete values that can be mapped into displacement or temperature fields.
The history of optical fibers goes back to the 1960s. In 1969, first gradient index fibers were manufactured by the collaboration of Nippon Sheet Glass Co. and Nippon Electric Co. for telecommunications applications but these fibers still had a damping of 100 dB/km caused mainly by chemical impurity of the glass. Great progress was made in the following years and in 1976 improved fibers with less than 1 dB/km was available in Japan, USA and UK. Infrared was then used instead of visible light. Today the damping is < 0.2 dB/km. The best suited glass for fibers is fused silica (SiO_2) [3].
In 1978, Ken O. Hill found the effect of photo sensitivity for Germanium doped fibers. Exposure to ultraviolet light induces a permanent change of the refractive index. The next step was to use this effect and write Bragg gratings into fibers which can reflect very small wavelength peaks. The wavelengths of these peaks change with temperature or when such fibers are strained. First commercial Fiber Bragg Grating Sensor was available in 1995 from 3M and Photonetics. Since 2000s more than twenty companies offer these sensors.
The classical techniques of classical Non – Destructive Evaluation (NDE) are not well suited for on – line structural monitoring, because of the difficulties in making in – situ implementation. The remedy is to develop new techniques, which can perform structural health monitoring in – service. Smart materials/structures in that sense provide this possibility. They do not only have traditional structural materials' functions, but also have actuating, sensing and microprocessing capability [4]. Comparing with the common NDE methods, FOS have many evident advantages. One of the main advantages is that these sensors are very lightweight and small enough that they can be embedded in composite materials in a non – obtrusive manner which does not degrade structural integrity. FOS are an enabling technology that will allow engineers to add nervous system to their designs, detect damage and monitor the health status.
Several types of fiber optic sensors have been developed so far for the non – destructive evaluation of the of engineering structures such as Fiber Bragg Grating sensors, Extrinsic Fabry – Perot Interferometer (EFPI), multi – mode optical fiber vibrations sensor and others.
FBG sensors can measure strain as metal foil strain gages do. Like strain gages, FBG can be used to build transducers for measuring many different physical quantities. Although FBG sensors cannot compete with metal strain gages in price and precision, they provide some superior qualities making them very suited to special applications:

- FBGs match quite well with composite materials like glass or carbon fiber reinforced plastics (GFRP or CFRP). They can directly be integrated into composites (embedding sensors into host material) or can be fixed directly (surface mounted) or as patches on the surface of the test object like strain gages
- FBGs can measure very high strain (<10 000 μm/m) and are therefore very well suited to highly stressed composite structures
- FBGs are small in size and lightweight
- FBGs are immune to electromagnetic interference (even lightning interference)
- FBGs are intrinsically passive and therefore can be positioned in high voltage and potentionally explosive atmosphere areas
- FBGs signals are not distance – dependant (up to> 50 km connection length is possible)
- On a single fiber many FBGs can be located in a row (>20 FBGs, with special interrogator technologies up to >100). No return fiber is needed.
- Long term stability is very high
- Good corrosion resistance
- Special versions of FBGs can be used at very high temperatures (>700º C)
- FBGs also have advantage in cryogenic environment because of their low thermal conductivity of the single fiber feeding many sensors and their stable optical properties with very low residual temperature dependencies near to liquid helium temperatures
- Very low magnetic field interactions
- Ease of installation

Some types of fibers have photosensitivity on specific wavelength such as germanium doped and hydrogen loading fibers. The photosensitivity in optical fibers can refer to a permanent change of refractive index of fiber core when the fibers are exposed to the light with specific wavelength. A uniform FBG includes a segment of optical fiber in which a periodic modulation of the core refractive index is implemented. In the Figure 1.3 a schematic illustration of an FBG sensor is shown. Usually in – fiber FBG can be

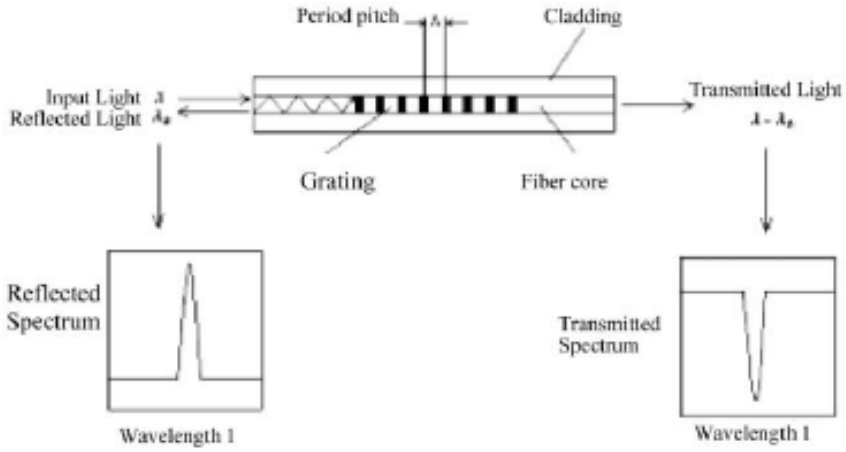

Figure 1.3 – Schematic illustration of an FBG sensor

fabricated on the germanium – doped single mode optical fiber by using the ultraviolet (UV) laser source in 240-248 nm. The fabrication technology includes interferometric method, phase – mask method, point – by – point method etc. The lengths of FBGs are normally 1 – 20 mm. When an input incident light illuminates the Bragg grating, a sort of light is reflected and other light is transmitted. Basically the principle of the FBG sensor is based on the measurement of the changes in reflective signal, which is the center wavelength of back – reflected light from a Bragg grating, and depends on the effective refractive index of the core and the periodicity of the grating. According to the Bragg condition, the Bragg wavelength can be expressed as:

$$\lambda_B = 2n_{eff}\Lambda \quad (1.1)$$

Where λ_B is Bragg grating wavelength, Λ is grating periodic spacing and n_{eff} is the effective reflective index of the fiber core. The Bragg wavelength will shift with changes in either n_{eff} or Λ. When an external mechanical or thermal deformation is subjected onto the grating area, the effective reflective as well as the periodic spacing index will be changed. The Bragg wavelength shift caused by the change of strain ($\Delta\varepsilon$) and change of temperature (ΔT) can be expressed in the form as below:

$$\Delta\lambda_B = \alpha\Delta\varepsilon + \beta\Delta T \quad (1.2)$$

Where

$$\alpha = \lambda_B(1 - P_e) \quad (1.3)$$

$$\beta = \lambda_B(\propto_\Lambda + \propto_n) \quad (1.4)$$

Where p_e is an effective strain – optic constant, $\propto_\Lambda$ is the thermal expansion coefficient for the fiber and $\propto_n$ is the thermooptic coefficient. So $\propto$ is the relevant wavelength – strain sensitive factor and β is the wavelength – temperature sensitive factor.

1.4.2 Actuation by Shape Memory Polymers (SMPs)

SMPs were first discovered in the 1980s.These materials can undergo large recoverable deformations upon the application of an external stimulus. The mechanism behind the shape memory phenomenon for the Shape Memory Alloys (SMA) is the reversible martensitic transformation i.e. transformation from lower martensite phase to higher austenite phase by heating or transformation from austenite phase to martensite phase by cooling down. The shape memory phenomenon in SMPs is based on from a dual segment system; cross links to determine the permanent shape and switching segments with transition temperature (T_{trans}) to fix the temporary shape. SMP's can be activated through many ways; heat, magnetism, electricity, light, moisture and certain chemical stimulus. These materials have some advantages over SMA's such as; up to 400% recoverable strain, low density, ease in processing, in tailoring of properties (transition temperature, stiffness, biodegradability and ease of functionally grading), programmability, controllability of recovery and relatively low cost. On the other hand they have some disadvantages compared with the SMA's. Their mechanical properties

are lower than that of SMA's. Polystyrene SMP's are a kind of materials that are actively used in the actuation of morphing wings. The following table (Table 1.1) shows some properties of polystyrene SMP's compared with NitiNol SMA's. As it can be seen from the table the main disadvantage of the polystyrene SMP is the relatively lower actuation stress value of this material. At the same time it has lower Young's Modulus compared with that of NitiNol SMA.
The first SMP was developed by CDF Chimie Company in 1984 under the trade name of polynorborene. It was commercialized by Nippon Zeon Company. Styrene butadiene based SMP was developed by the Asahi Company. Cornerstone Research Group has developed some thermosetting SMP's. Some of the materials developed by this group could be listed as; styrene based SMP (Veriflex) with a glass transition temperature of ranging from 60-70 °C, a one part epoxy SMP with a glass transition temperature of

Table 1.1 – Some properties of NiTi SMA's and Polystyrene SMP's

	NiTi SMA	**Polystyrene SMP**
T_s (Transition Temperature) °C	40 – 100	62
Transformation Strain %	Max 8	50 – 100
Actuation Stress MPa	˜100	2 – 10
Young's Modulus above T_s GPa	˜83	1.24
Young's Modulus below T_s MPa	˜28 – 41	2 – 10
Poisson's Ratio	0.33	0.30
Density, gr/cc	6.45	0.92

about 90 °C, a two parts epoxy SMP with a glass transition temperature of about 104 °C and a cyanate ester SMP with a high glass transition temperature ranging from 135 to 230 °C. Composite Technology Development Inc. has commercialized a thermosetting epoxy SMP (CTD-101 K) with a glass transition temperature of about 113 °C. Mitsubishi Heavy Industry has produced a series of thermoplastic polyurethane SMP's with glass transition temperatures ranging from 40 to 55 °C.
An SMP must consist of dual-segments, one that is highly elastic and another that is able to reduce its stiffness upon a particular stimulus. The second one can be either molecular switches or stimulus sensitive domains. Upon exposure to a specific stimulus the switching/transition is triggered and strain energy stored in the temporary shape is released which results in the shape recovery.
Figure 1.4 shows a thermo mechanical cycle of a thermo responsive SMP. In this figure, three phases could be observed. The first phase is the shaping of the SMP into its original state. The second step is heating the SMP material above the thermal transition temperature (T_{trans}) (T_{trans} could be either T_g, glass transition temperature or T_m, melting temperature) and deformation of the SMP by applying an external force, cooling below T_{trans}, removal of the constraint to obtain a temporary pre-deformed shape. The last phase is the heating of the predeformed SMP above T_{trans} and then recovery of the SMP towards its original state (recovered shape).
Although SMP's have some advantages over SMA's, there are some drawbacks of these materials such as possessing low mechanical strength and shape recovery stress

(low actuation stress) as mentioned before. The typical mechanical strength of a NiTi SMA is 700-1100 MPa (annealed) or 1300-2000 MPa (not annealed), and that of a Cu based SMA is about 800 MPa. Mechanical strength of an SMP is between 5 to 100 MPa based on different types and compositions of SMP's. The actuation stress of an SMA can reach to 800 MPa while that of an SMP is between few tenths of an MPa to a few tens of MPa. To eliminate these characteristic deficiencies SMPs could be reinforced by using high modulus organic or inorganic fillers. Some of the reinforcing methods are listed as following:

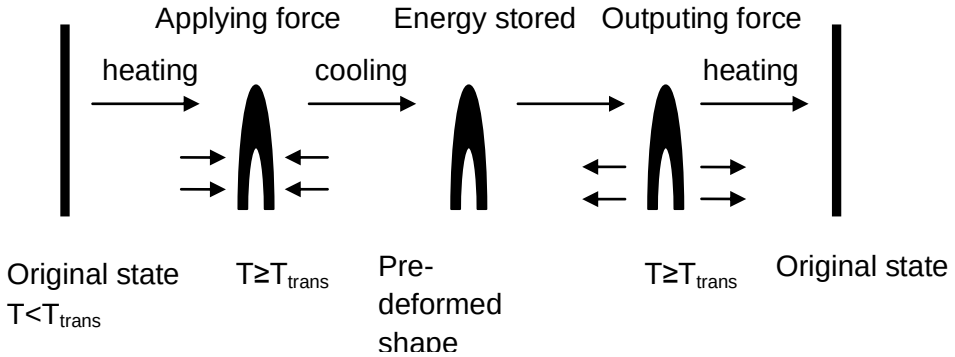

Figure 1.4 – Thermo mechanical cycle of a thermo responsive SMP

- Microfiber or fabric/SMP
- Carbon nanotube (CNT) or carbon nanofiber (CNF)/SMP
- Nanoclay/SMP
- Nano SiC/SMP
- Carbon block (CB)/SMP
- Organic filler/SMP
- Other inorganic fillers/SMP

Several researchers investigated reinforcing fillers in order to improve the mechanical properties and to diversify the applications of SMP's. Liang et al. investigated glass and Kevlar fiber reinforced SMP composites and observed increased stiffness and decreased recoverable strain as a result of incorporation of the reinforcements [5]. Gall et al. reported increase in elastic modulus by approximately a factor of 3 due to the incorporation of 40% SiC in weight. Blending carbon block or a conducting polymer with the SMP's have been going on for the reinforcement of the SMP composites. Vapor grown carbon nano fibers reinforced SMP composites have been studied by Sahoo et al., incorporation of 3.3% nanofibers in weight resulted two fold increase in the actuation stress of the SMP composites. Koerner et al. investigated polyurethanes reinforced with carbon nanotubes or carbon block of similar size and reported that the nanocomposites display increased shape fixity. The carbon nanotube – reinforced materials show

almost 100% shape recovery compared to the material, reinforced with carbon block, which exhibit only a limited shape recovery of around 30%.

SMP's can be categorized as physically or chemically linked i.e. thermoplastics or thermosets. Chemically cross linked SMP's can be achieved through a suitable cross linking chemistry, which are referred to as thermosets. Physically cross linked ones require a polymer morphology consisting of at least two segregated domains, which are referred to as thermoplastics. SMP's are typically dual shape in nature; original shape and deformed shape. The shape memory feature is resulted from a combination of the polymer's molecular architecture and a particular programming procedure that enables the formation of a temporary deformed shape. Like other polymers SMP's also possess three dimensional molecular network-like architectures. The network architectures are thought to be constructed through cross linking net points, with polymer segments connecting adjacent net points. These strongly cross linked architectures ensure that the polymer can maintain a stable shape on the macroscopic level for enabling both the original and deformed shapes. The domain of the cross - linking netpoints can be either physically or chemically cross linked structures. As was stated before physically cross linked structures are called thermoplastics while chemically cross linked ones are called thermosets. SMP's can be considered as copolymers with a hard segment acting as a fixed phase and a soft segment acting as a reversible phase. The fixed phase prevents free flow of the surrounding polymer chains upon the application of a stress. The reversible phase undergoes deformation in a shape memory cycle and is responsible for elasticity. This phase acts as a molecular switch freezing the deformed shape below the transition temperature while releasing the polymer chains towards the original shape at or above the transition temperature.

Theoretical modeling of the mechanical constitutive behavior of an SMP proves to be difficult due to the large recoverable deformation capability of SMPs and the heavy dependence of polymer properties on both time and temperature. Two approaches have been reported to develop a constitutive model for SMPs; first one is based on the linear or nonlinear viscoelastic theory while the second one is based on the micromechanical theorem of phase transformation.

The important quantities to be determined for describing shape memory properties of a material are the strain recovery rate ($R_r(N)$) and strain fixity rate ($R_f(N)$). The strain recovery rate qualifies the ability of the material to memorize its permanent shape while strain fixity rate is the ability of the switching segment to fix the mechanical deformation.

Assuming that an SMP sample is deformed to a constant strain ε_m at a constant strain rate. While maintaining the strain at ε_m, the samples were cooled down to a low temperature and unloaded. Upon removing the constraint under cooled condition, a substantial recovery of strain ε_u occurs. When SMP sample is heated above T_s and kept at that temperature allowing the recovery to take place. This completes the thermomechanical cycle leaving a residual strain ε_p. The R_r and R_f for Nth cycle can be determined from the following formulas [6]:

$$R_r(N) = \frac{\varepsilon m - \varepsilon p(N)}{\varepsilon m - \varepsilon p(N-1)} \quad (1.5)$$

$$R_f(N) = \frac{\varepsilon u(N)}{\varepsilon m} \quad (1.6)$$

Various viscoelastic and thermomechanical models have been studied to correlate the viscoelastic/thermal properties with the shape memory behavior. Shape memory effect can be described briefly as the following mathematical models:

$R_f = 1 - E_r/E_g$ (R_f, shape fixity ratio) (1.7)

Where E_r is the high rubbery modulus and E_g is high glassy state modulus

$R_r = 1 - f_{IR}/\left[\left(1 - E_r/E_g\right)f_\alpha\right]$ (R_r, shape recovery ratio) (1.8)

Where f_{IR} is the viscous flow strain and f_α is the strain when $t \geq t_r$

E_g provides the material with high shape fixity during simultaneous cooling and unloading whereas E_r provides high elastic recovery at high temperature.
SMPs have been synthesized for more than two decades and research efforts have been undertaken for the characterization and introduction of new materials to the market. Table 1.2 illustrates the classification for existing polymer networks that exhibit the shape – memory effect.

Table 1.2 – Schematics of structural categorization of SMPs

<table>
<tr><th colspan="4">Thermally Induced SMPs</th></tr>
<tr><th colspan="3">Physically Cross – Linked SMPs (Thermoplastics)</th><th>Chemically Cross – Linked SMPs (Thermosettings)</th></tr>
<tr><td colspan="2">A. Linear</td><td>B. Branched</td><td>a. Cross-linked PE</td></tr>
<tr><td>A1.Block copolymers</td><td>A2.High molecular weight polymers</td><td rowspan="13">PE nylon 6 graft copolymer</td><td>b. Partly cross-linked/thermosetting SMPU’s</td></tr>
<tr><td>A1.1.Segmented polyurethanes</td><td rowspan="12">Polynorborene</td><td>c. Cross-linked poly(ε-caprolactone)</td></tr>
<tr><td>A1.2.Polyethylene terephthalate and polyethylene oxide</td><td>d. Thermosetting epoxy resins</td></tr>
<tr><td>A1.3.Polystyrene and poly(1,4-butadiene) copolymers</td><td>e. Shape memory liquid crystalline elastomers</td></tr>
<tr><td>A1.4.Polybutadiene /PS copolymers</td><td>f. Shape memory polyolefines</td></tr>
<tr><td rowspan="2">A1.5.Triblock copolymers of poly(tetrahydrofuran)and poly(2-methyl-2-oxazoline)</td><td>g. Thermosetting polystyrene</td></tr>
<tr><td>h. Shape memory polysiloxanes</td></tr>
<tr><td rowspan="2">A1.6.Polycaprolactone-polyamide copolymers</td><td>i. Polyethylene-poly(vinyl acetate) copolymers</td></tr>
</table>

2 Morphing

The chance of exploiting the compliance of an aerodynamic surface to increase the performance of an aircraft is an attractive research field of particular interest in the aeronautical industry. In the last decades in this field several research efforts have been undertaken either by universities or by defense companies on all technologies that fall under the term morphing. This term, in the engineering sense, it is summarized that “all technologies increasing performance of an aircraft that will change some of its geometric features trying to adapt the best possible external conditions and the goal of the mission” [7]. Majority of the airplanes today are designed to operate efficiently for a specific flight condition (cruise speed and weight), which is a design parameter; if you want to try to optimize the aircraft and its architecture considering several conditions at the same time, there would inevitably be a compromising solution often with conflicting requirements. In both cases however, it still does not have the optimal behavior for a certain time within a given mission; this implies a waste of resources (fuel and time), thereby resulting higher operating costs for the aircraft. From this motivation, stems mainly the big push towards projects that exploit the advantages of the morphing technology. Speaking on the configuration of the airplane to adapt to the particular moment of the mission, it is clear that the overall efficiency of the solution will be improved.

As several flight regimes occur during a typical aircraft mission so it is practically impossible to define a single configuration able to maximize aerodynamic efficiency, maneuverability, stability and fuel consumption in any circumstance. An aircraft is supposed to adapt its shape to distinct flight conditions thus able to change its shape by means of morphing from one flight mode to another. This concept is provided by continuous controllable deformations which takes its inspiration from nature. It is often referred as bionics or bio – inspiration. Bionics is the application of biological methods and systems found in nature to the study and design of engineering systems and technology. Bio – inspired robots, morphing aircraft wings, smart fabrics, self cleaning surfaces that imitates lotus like plants are all the products of the conscious copying of examples and mechanisms from natural organisms and ecologies. The morphing wings were inspired by different bird species that have differently shaped wings according to the speed at which they fly. The morphing aircraft concept is taking its ideas from the birds and fishes, mimicking the wings of a bird and scales of a fish. Morphing structures can expand the flight envelope of a vehicle, eliminate the need for flap type mechanisms, and reduce the aerodynamic drag for the aircrafts [8].

In the aeronautics field, morphing has been used to identify those aircrafts that undergo certain geometrical changes to enhance or adapt to their mission profiles.

2.1 Definition and Classification

Sofla et al. in their recent paper have argued the definitions and challenges on shape morphing aircraft wings [9]. They concluded that there is neither an exact definition nor an agreement between the researchers about the type or the extent of the geometrical changes necessary to qualify an aircraft for shape morphing. There is also not a clear definition for an enabling shape morphing technology either but a general agreement exists that the conventional hinged control surfaces or high lift devices such as flaps or slats that provide discrete geometry changes cannot be considered as morphing. Reich and Sanders have made some descriptions based on orthodox or non – conventional approaches [10]. The term is loosely used to describe any non traditional method of moving vehicle components. In this form, the focus is typically on conformal control surfaces, camber variations, or other changes to the wing cross – sectional shape. Another more radical definition is a change of vehicle state to achieve a performance metric, whether it is shape, color, etc. In terms of shape change, this means geometry variations that go beyond sweeping wings or thrust vectoring; it means large changes in span, wing area, chord, etc. To achieve significant variations in performance, it has been shown that these parameters need to change on the order of 100%. This clearly goes beyond simple geometric changes that have been previously implemented.
It is possible to make a substantial distinction of the morphing based on geometrical scales where it is put into operation. In fact speaking of morphing on a large scale when dealing with radical changes in the configuration of the airplane; with this technique it is studied to obtain performance improvement through changes in the scope of the wing surface, planform, arrow or elongation. This phenomena influence mostly over the performance and flight mechanics of the flight of the airplane and allows adapting to the best behavior in the various phases of the mission, allowing a change of the global characteristics of the configuration.

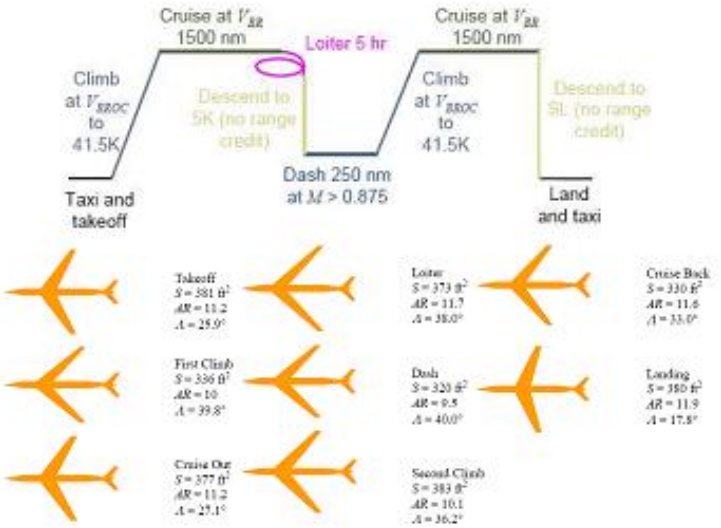

Figure 2.1 – Optimizing aircraft configuration

In Figure 2.1 [11], it can be seen that observing the result of the optimization of the main morphological characteristics of the airplane in the various phases of a mission, with the aim of minimizing the overall weight of the airplane, it is clear that the ability to change the external geometry of the aircraft would lead to significant benefits in terms of behavior of the airplane during the various stages of the mission. On the other hand, the morphing in the medium scale, geometrical changes are more localized like the changes in the medium line of the aerodynamic profile or the controlled variation of wing warping. This technique allows increasing the efficiency of the various aerodynamic surfaces going to change their behavior in a more targeted way. The main objective of this type of geometrical changes is to operate a variation in the distribution of load in the chord and opening the ways to obtain a series of advantages in the proposed design solution: for instance we can think of adopting this type of technique to reduce the stresses to which the structure is subjected by distributing the load on the surface, or it can be thought to adopt a solution of this type to improve the response to the complete gust of the system. The morphing of small scale involves changes in geometry even smaller, affecting mostly only small areas of the profile; the geometrical changes of small scale are designed to operate a more localized control on the flow; the basic idea is to modify the behavior of the boundary layer near the surface, in order to obtain a reduction in resistance of the aircraft to the airflow.
Regardless of the geometric scale on which they are designed, all of these strategies of morphing, have the goal, as already pointed out, to obtain an improvement of the characteristics in flight. The main advantages that may be used in these particular concepts could be:

- Increase the performance of the aircraft on time, while broadening the envelope of flight
- Replace the conventional control surfaces to increase the overall performance and decrease the radar traceability
- Reduce the resistance to increase the autonomy
- Reduce vibration and control the static and dynamic instability

The reasoning behind the advantage of morphing is that since current aircraft are designed with wing geometry that offers optimal performance at one critical stage of flight (and significantly lowers performance at a different stage), morphing aircraft could offer optimal performance at multiple stages of flight. Figure 2.2 is a spider plot that attempts to graphically capture the advantage of morphing aircraft [12].
The marked radii of the circle each represent a different stage of flight (take – off, landing, attack, cruise, etc.) while the wing orientation sketches on the ends of the radii represent the ideal wing configuration for the stage of flight. Specific stage of flight is not marked since the plot applied generally to many aircraft and stages of flight. The inside areas of the circle represent efficiency during the stages of flight, such as aerodynamics, range, fuel economy and endurance. The blue area represents aircraft efficiency of a highly morphable aircraft at each corresponding wing orientation during the stages of flight. The blue area is the largest area since the aircraft would be able to achieve almost exactly the desired optimal wing configuration for each stage of flight. The green and red areas represent aircraft efficiency at the same stages of flight if the

aircraft were only able to partially morph or not morph at all, respectively. Red area would correspond to current static aircraft and has extremely low performance at a few

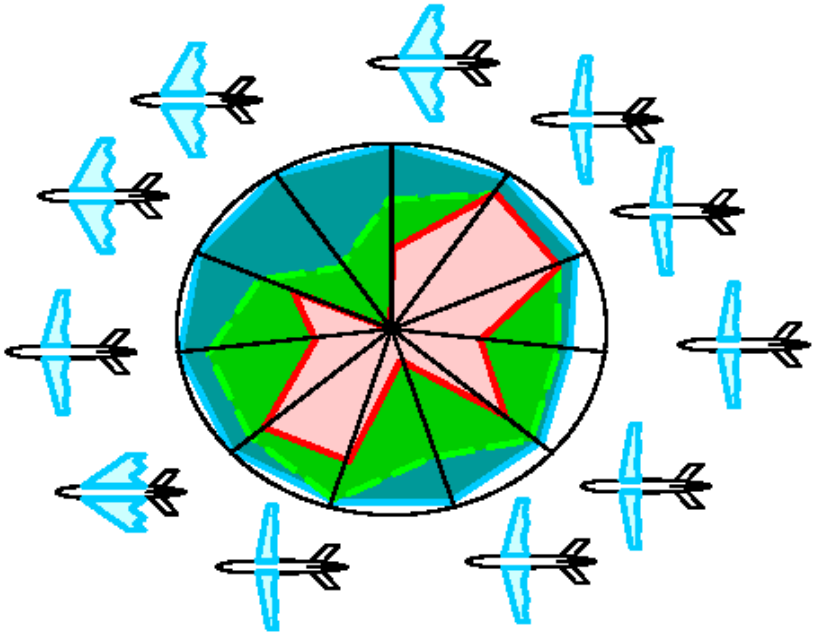

Figure 2.2 – Spider plot comparison of fixed and morphing wing aircraft

stages of flight and is unable to perform at one stage of flight. Specific stages of flight are not given in the spider plot as said before, but the general depiction of efficiency for a morphing aircraft at different stages of flight are very representative.
A review on the current and past efforts in the development of morphing aircraft will be given briefly. Included are variable sweep aircraft, the Active Aeroelastic Wing (AAW) and the Morphing Aircraft Structures (MAS) Program as well as morphing skin aircraft. Each of these programs has created aircraft that have been at least through early phases of flight testing [13].

2.1.1 Variable Sweep Aircraft

The original morphing wing came in the form of variable sweep wings, sometimes called swing wings. Aircraft with variable sweep wings employ kinematic strategies to change the wing's sweep angle. A well known morphing aircraft is the F – 14, which has variable sweep wings, other examples are F – 111 and B – 1. Figure 2.3 shows an F – 14 which performs multi – role successfully [14]. The variable sweep wing or swing wing uses kinetic and mechanical principles to change sweep angle in the wing. By decreasing sweep angle, wetted surface becomes bigger. It produces more lift force with less fuel consumption. On the other hand, by increasing sweep angle, wetted surface is getting smaller. It reduces drag, so aircraft can dash faster than conventional air craft. These variable sweep air craft have the advantage that it is easy to change the sweep angle with an easy mechanism. But this way still has some disadvantages. One of the critical problems is that it is very complex to use a hinge to make a variable wing.

The wing needs more components and control to move the hinge of the wing. It causes more components in the wing, and it results in a heavier wing that prevents lighter aircraft. The variable sweep wing allows an aircraft to operate in a small range of different flight situations.

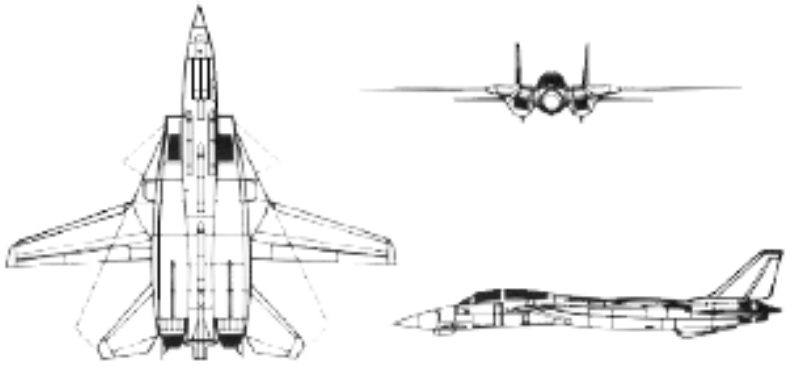

Figure 2.3 – F14, variable swing aircraft

2.1.2 Active Aeroelastic Wing

The AAW program was a joint venture between the United States Air Force Research Laboratory, Boeing's Phantom Works, and NASA. The program aimed to create an aircraft with increased roll control via purposely inducing a degree of wing twist. This technique was actually seen in the very beginnings of aviation. The Wright brothers Wright Flyer allowed for wing warping to increase the roll control. However, as aircraft speed and performance have increased, application of wing warping has become a considerably tougher puzzle to solve. An F/A – 18A hornet fighter jet was chosen as the test platform for the AAW program. This plane, originally developed by McDonnell Douglas, was designed for both air to air and air to ground combat and has the capability to take off from an aircraft carrier. The hornet was modified to allow the outer

Figure 2.4 – F/A – 18A in flight

wing to twist upward 5 degrees by using modestly softer skins. The aircraft was demonstrated in its first successful flight test at Edward's Air Force base on November 2002. In the Figure 2.4 an F/A – 18A could be seen.

2.1.3 Morphing Aircraft Structures

For Projects in the MAS program, there are specific requirements that had to be met by each aircraft. The wings had to be able to meet the following performance criterion:

- 200 % change in Aspect Ratio
- 50 % change in Surface Area
- 5º change in Wing Twist
- 20º change in Wing Sweep

The aspect ratio of a wing ($\frac{s^2}{A}$) gives a measure of slenderness from tip to tip, Where s is the wing's span and A is the wing's surface area. A high aspect ratio means a long slender wing while a low aspect ratio signifies a shorter span with a larger chord. Higher aspect ratio wings exhibit less drag because passing air flows a shorter distance across the wing surface. The MAS program produced two prototype morphing aircraft. Lockheed Martin created a morphing UAV that used a folding mechanism. During cruise mode, the wing would be completely flat like a typical airplane. However, to shift into different modes, the wing folds out of its horizontal plane and move toward the fuselage. This UAV was dubbed the "Z – Wing" because the wing resembled the shape of a 'Z' when folded against the fuselage. The Figure 2.5 shows Lockheed Martin's 'Z' wing aircraft.

Another attempt led by NextGen Aeronautics created a morphing UAV that utilized a wing that folded in the horizontal plane as shown in the Figure 2.6. This UAV was originally referred to as "BatWing" but has since been named MFX – 1 by NextGen. MFX – 1 is a 450 kg remote controlled UAV powered by a single jet engine. In order to accommodate the necessary deformations, MFX – 1 was outfitted with a flexible silicone skin. Metal ribbons were used as a support structure under the silicone so the wing could properly support aerodynamic loads.

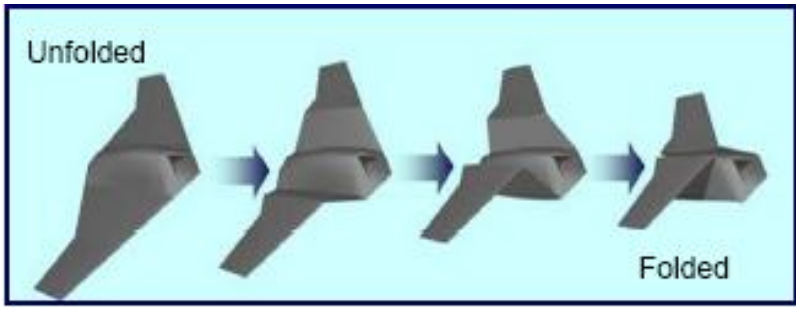

Figure 2.5 – Lockheed Martin Z – wing unmanned aircraft

In August of 2006, NextGen successfully flight tested MFX – 1 in California. The UAV sustained an area change of 40 percent, span change of 30 percent and sweep varying from 15 to 35 degrees while in flight. It also attained airspeeds of about 100 knots

during the test cycle. This was the first recorded successful test of an aircraft that morphed during flight. After MFX – 1, NextGen developed a larger 1.3 tons morphing UAV named MFX – 2. MFX – 2 used twin jet engines for propulsion and also encompassed a flight control system that allowed autonomous flight. In September 2007, a flight test of the aircraft once again obtained success while demonstrating a 40 percent change in wing area, 73 percent change in span and 177 percent change in aspect ratio.

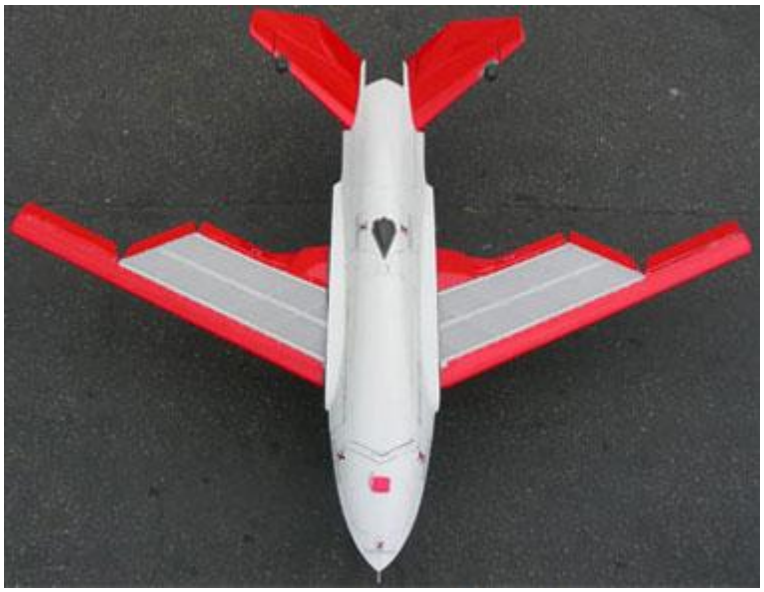

Figure 2.6 – NextGen Aeronautics MFX – 1

2.1.4 Morphing Skin Aircraft

A novel method that can transform wing shape is using flexible skin that consists of composite and fibers. Using flexible material has been researched in the Air force Research Laboratory and NASA as an effective alternative. The goal of this method is creating a morphing wing like that of birds using different material. Flaps and fuselage sometimes split or move together using actuators in this method. The main barrier and key point of this method is how to make new material that is transformable and rigid to maintain the load of the aircraft during flight.

2.2 Problem of Indirect Control of Aerodynamic Forces in Aeronautical Structures

The control of aerodynamic forces could be achieved in two ways; either direct control of lifting surfaces by a passive/active system or indirect control by means of actuators, electric motors and other standard hinged control surfaces. The conventional hinged control surfaces or high lift devices such as flaps, ailerons or slats that provide discrete geometry changes offer indirect control for the aircrafts. The Figure 2.7 shows breakdown of subassemblies of an aircraft [15]. In this figure horizontal control surfaces like aileron and flap could be seen as well as vertical control surface like rudder. Direct

control techniques such as morphing is connected with the spanwise or chordwise deflection meaning large changes in wing area, span or chord.
By far, the most important contribution which artificial stability can offer to an airplane is the use of direct force control modes. Conventional aircraft control modes are indirect; the aircraft must be pointed in a direction by means of its pitch, roll and yaw controls. The controls serve to change the aircraft's attitude, the change in attitude changes the direction of the resultant force vector acting on the aircraft and the flight path is altered. Thus translation must be generated through rotation, indirectly. In direct force control modes the control forces act directly on the aircraft, generating the desired translation.
By creating balanced couples of forces a constant attitude may be maintained in translation, enabling "pointing" without its indirect control effects. The implications for gunnery and ground attack are obvious [16].
The implementation of direct force control requires changes in aerodynamics. The direct control of the aerodynamic surfaces involves the use of non – conventional approaches. General Dynamics F – 16CCV/AFT I – 16 project uses an F – 16 with canards mounted on either side of the air intake. A configuration made by McDonnell Douglas involves the use of variable incidence wings, a beavertail elevator and vertical control surface under the nose.

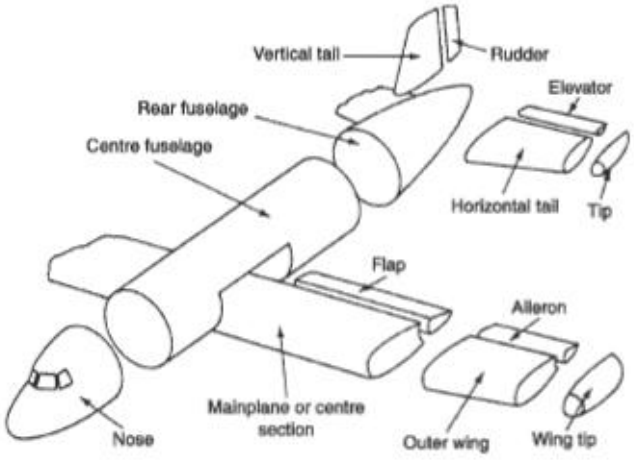

Figure 2.7 – Typical subassembly breakdown of an aircraft

2.3 Smart Materials/Structures

Smart structures – also known as active or adaptive structures- are capable of sensing and reacting to their environment in a predictable and desired manner by utilizing sensors, actuators, signal processors and communication networks. The actuators and sensors can be embedded or mounted to the structure in different ways. Recently, several research activities in the manufacturing process field have been devoted to develop smart structures that could combine high mechanical efficiency, due to composite host materials, with good functional properties of the embedded sensors and actuators [17]. The embedding of these smart devices into the structures could give some advantages compared to their bonding onto the outer skin (mounting). For example, they allow the actuation in locations hardly accessible from outside because of

shape constraints; the protection of the actuation system inside host structure from all environmental effects, which may reduce its performance, can be also achieved. In addition, active structures could be applied even in those cases where a clean and smooth surface is required (i.e. aerodynamic surfaces).
The embedding technique of these components within the load – carrying structure is still not a fully comprehended issue. Research activities are oriented to the development of manufacturing techniques, characterization of embedded sensors and the estimation of actuators invasivity (active and passive) on the smart structure performance which are of great importance. Furthermore, most of the applications are strongly dependent on the availability of useful numerical tools. In fact, all the design activities regarding structures are nowadays related to the adoption of numerical models able to predict the efficiency and performance of the systems. The characteristic of the smart composite structures underlines this problem due to the joined complexity of the active materials behavior (nonlinearity) with the composite material modeling (anisotropy, damage mechanisms).
Driven by the requirements from engineering practices, novel materials are being developed for enhanced performance and new functions. Among them there is a group of materials that are able to respond to a particular stimulus by means of altering their physical and/or chemical properties. Such stimuli include heat (thermo – responsive materials), electrical current/voltage (electro – responsive materials), magnetic field (magneto – responsive materials), stress/pressure (mechanoresponsive materials), pH change/solvent/moisture (chemo – responsive materials) and light (photo – responsive materials), etc. These materials are known as the stimulus – responsive materials [18], as represented in Figure 2.8.
Stimulus responsive materials and their composites have become a very hot topic in the recent decades due to a wide range of potential applications, from functional nano composites to drug/gene delivery. Among them, one group of material is able to change their shape at the presence of the right stimulus; this is the shape change material. Among others, Electro Active Polymer (EAP) and Piezoelectric material (PZT) are typical examples of shape change materials.
In the other group which is known as the Shape Memory Materials (SMMs); they exhibit shape memory effect, the temporary shape can be virtually held forever unless the right stimulus is applied to trigger the shape recovery. The shape memory effect can be defined as the ability to recover the original shape at the presence of the effective stimulus, after being severely and quasi – plastically distorted [19].
There are different types of SMMs that have been developed so far. Among them, Shape Memory Alloys (SMAs) and Shape Memory Polymers (SMPs) are the most important and widely used ones at present. The mechanism behind the shape memory phenomenon for the SMA's is the reversible martensitic transformation i.e. transformation from lower martensite phase to higher austenite phase by heating or transformation from austenite phase to martensite phase by cooling down. The shape memory phenomenon in SMPs is based on from a dual segment system; cross links to determine the permanent shape and switching segments with transition temperature (T_{trans}) to fix the temporary shape. One of the newest types of SMM is named Shape Memory Hybrid (SMH) which is made of at least two components but without any shape memory effect as an individual, shares the same mechanism as SMPs. Shape Memory

Ceramic (SMC) may have the same working principle as that of SMA or have a multiphase system which is thus similar to that of SMP. Gels are normally considered as

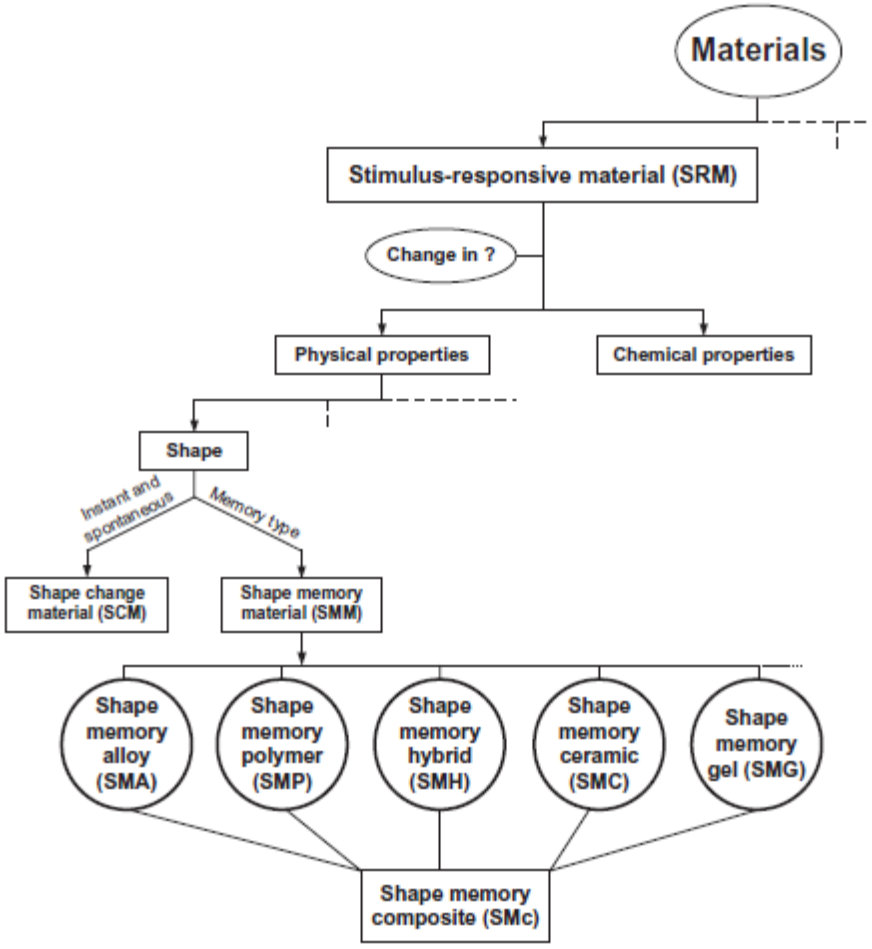

Figure 2.8 – Location of various types of Shape Memory Materials within the World of Materials

a typical Shape Change Material (SCM) due to the swelling effect and/or electrical charge that could be used to develop novel materials such as light – triggered swelling as reported in [20] and wet shrinkable material reported in [21]. Some gels have the Shape Memory Effect (SME) due to a reversible order – disorder transition.

2.3.1 Research on SMP Utilizing Morphing Wing

SMPs have many applications in the industry and research. The application areas are ranging from space to automobiles, from MEMS to temperature devices and damping elements. Recently they are being developed for deployable components and structures in aerospace (such as deployable antennas, solar panels, morphing skins, optical reflectors, hinges and trusses). Many patents filings are being done for the appliances

utilizing SMPs such as grippers, intravascular delivery system, hood/seat assembly and tunable automotive brackets in the vehicles.
Flexible skin is required for morphing wing which undergo large strains and have low in-plane stiffness. The skin must handle the out-of-plane aerodynamic loads and at the same time carrying some shear loading which is the primary function of the wing skins. SMP is a promising candidate for the skin material of the morphing wing. It becomes flexible when heated to a certain degree, and then returns to a solid state when the stimulus is terminated. Their multiple state abilities allow them to easily change shape and once cooled, to resist appreciable loads. Enabling the SMP materials to change between the rigid and the elastic states is the responsibility of the skin activation system. To activate the SMP, using embedded heating wires into the skin was developed by Cornerstone Research Group (CRG) [22]. At a specific power the wires were able to heat the SMP above its transition temperature. CRG is carrying out several concepts for the morphing wing. One of the concepts they are working on is seamless skin at the wing fold. As shown in the Figure (Figure 2.9), the feasibility of morphing SMP skin concept in a 2 – D test jig is demonstrated. In another research morphing concept of a variable camber wing was developed by Yin et al [23]. The demonstrator consists of a flexible SMP skin, a metal sheet and a honeycomb structure as shown in Figure 2.10. Metal sheet was used to replace the traditional hinges to keep the surface smooth during the camber changing. Honeycomb material which is high strain capable in one direction without dimensional change in perpendicular in – plane axis, provides distributed support to the flexible skin. The flexible SMP skin was covered to create the smooth aerodynamic surface. Utilizing SMPs in this demonstrator, chordwise deflection has been obtained whereas spanwise deflection was observed in the previous research (Figure 2.9).

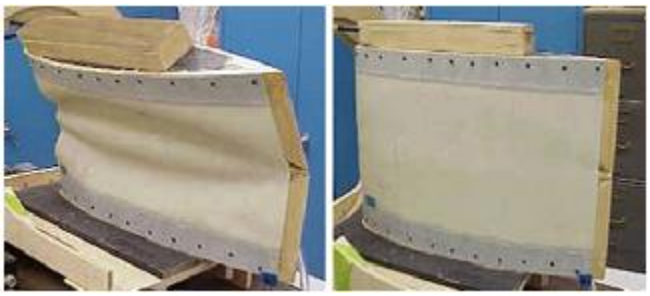

Figure 2.9 – Morphing wing covered with SMP skin on a test jig

Figure 2.10 – Picture of the original state and morphing configurations of the variable camber wing

In his thesis Gross has studied the mechanical characterization of shape memory polymers to assess candidacy as morphing aircraft skin [13]. He used Veriflex, a styrene based SMP which has a glass transition temperature of 62°C. Below this temperature Veriflex has an elastic tensile modulus of 1241 MPa and above this temperature of 0.2 MPa. This sudden change in the stiffness that is dependent on the temperature makes Veriflex a suitable candidate material for the morphing aircraft skin. The manufacturer of Veriflex is CRG industries (USA) and it is a commercially available material. Although most of the attention is given to polyurethane thermoplastic SMPs, polystyrene SMPs have been recently investigated. In his research he found out that a 20 % decrease in the Young's Modulus produces an additional 20 % deflection in the wing skin. One of the important outputs of his studies is when the wing skin material is in its soft state (over T_g); the simulation produced very large deformations in response to the out of plane aerodynamic loads. This gives the need for a supporting structure. Based on this reality he designed a honeycomb structure which is compliant to the in – plane morphing deformation and rigid in response to out-of-plane aerodynamics loads.
The following table (Table 2.1) shows the mechanical properties of the Veriflex. The values were taken from Rauscher's thesis [12].

Table 2.1 – Some properties of Veriflex

	Mechanical Properties	**Specifications ($T<T_g$)**
ASTM D 638	Tensile Strength	22.96 MPa
ASTM D 638	Tensile Modulus	1241 MPa
ASTM D 638	Elongation to Break	3.90%
ASTM D 790	Flexural Strength	31.72 MPa
ASTM D 790	Flexural Modulus	1241 MPa
ASTM D 695	Compressive Strength	32.41 MPa
ASTM D 695	Compressive Modulus	1447.9 MPa
	Thermal Conductivity	0.17 W/(m*K) at 18.6°C
	Density	0.92 gr/cm^3

Although tensile modulus of Veriflex is given as 1241 MPa ($T<T_g$) by the CRG Industries, Gross found out experimentally that the tensile modulus of this material is lower (1050 MPa) than the given value. He reasoned this problem to the curing process. The curing processes of the company and his are thought to be versatile. Rauscher in his thesis examined the possibility to use SMPs as a morphing wing skin. He also used Veriflex SMP as the candidate material. The tensile modulus ($T<T_g$) he used was 1050 MPa contrary to 1241 MPa that was reported by the CRG Industries. When $T>T_g$ tensile modulus becomes 0.2 MPa as given by the manufacturer. This value is very close to 0.24 MPa which is given by Rauscher.
Healable shape memory polymers were developed by NASA in 2005 in collaboration with Cornerstone Research Group. This material was used for intelligent structural health monitoring system in which the shape memory is able to penetrate inside the damaged surface and heal it. This technology indicates a possible collaboration of a polymer material that exhibits both the shape memory and the healing features. One of the requirements of a morphing wing skin is that the skin is placed on a support structure and therefore skin must be able to resist against abrasion due to its contact

with other wing structures. A tear in the skin during the flight can fail the wing and so as the aircraft. Another requirement states that the material should sustain large in-plane normal and shear strains. This allows the material to be stretched during morphing. After the material is stretched, it should return to its original shape without any damage. This feature will keep the wing skin from sagging after the wing returns to its original position. A dip in the wing skin would otherwise increase the drag across the wing surface thus decreasing the wing‘s efficiency. The wing skin is required not only to withstand the out-of plane aerodynamic loads during the flight to ensure the performance of the airfoil but also the required aeroelasticity of the flexible skin will ensure the stiffness of the structure.

During his MSc studies Jee investigated the SMP material for use as a morphing wing skin [14]. He, like Gross, used SMP material from Cornerstone Research Group. The SMP material he used was Veriflex E2 resin system (not the classical Veriflex). This material has a glass transition temperature of 103°C. When this material is heated above its transition temperature, it changes from a rigid plastic to an elastic rubber. In its elastic state it can reach 100% recoverable strain. When it is cooled while constrained in this new elastic shape, the polymer hardens and maintains its new deformed configuration indefinitely. When heated above its glass transition temperature, this material returns to its original shape. This process can be repeated indefinitely without the loss of shape memory properties or the material degradation.

Morphing wing structure needs to demonstrate repeated shape change during flight, the effects of cyclic thermal and mechanical loadings on response characteristics of SMP composites should be thoroughly comprehended. Stress strain response and failure mechanisms are not well understood for these materials. SMPs are operating in a wide variety of temperatures. In order to understand the behavior of SMP in these temperature ranges, thermo – mechanical testing should be carried out. A thermo – mechanical fatigue testing will help to understand the properties of these materials in a wide range of temperatures.

The following Table (Table 2.2) shows some companies/groups which their products are commercially available or hold patents in the SMP area. Cornerstone Research Group (CRG), USA and Center for Composite Materials and Structures, Science Park of Harbin Institute of Technology (HIT), China are the pioneers in the shape morphing skin research that utilize SMP material as the skin material. CRG manufactures and employs Veriflex, its own SMP brand, as a candidate material to be utilized for the space deployable mechanisms and seamless morphing wing skin. Their SMP brand Veriflex is also used by other researchers working in the field of shape morphing. Composite Materials and Structures Group from China on the other hand, is working on the field of smart materials/smart systems including morphing aircraft wing. They were able to demonstrate a mini UAV that has shape memory polymer morphing skin. In the laboratory experiments the group carried out testing of a morphing wing which has the ability of chordwise deflection and the wing skin had the styrene based SMP.

Table 2.2 – Companies/Groups producing commercially available SMPs or holding patent in this area

Company/Group	Product Name	T_g °C	Properties	Utilization
Cornerstone Research Group, USA	Veriflex Veriflex E2	62 103	Thermoset epoxy, Polystyrene SMP	Seamless morphing wing skin Deployable space mechanisms
SMP Technologies Inc., Japan	Diaplex (Mitsubishi originated)	25-90 T_g changes based on the product	Polyurethane SMP, Four types of production: molding, potting, solution, micro beads	Self deployable space structures Medical devices
Composite Technology Development, USA	Tembo	113	Thermoset epoxy	Space deployment mechanisms Morphing wing skin
Center for Composite Materials and Structures, Science Park of Harbin Institute of Technology (HIT)	Unknown, there is chance that they are using Veriflex or their own mix	54, 75, 125	Styrene based thermosetting SMP Epoxy based SMP	Morphing wing skin

3 Auxetic Materials/Structures

Much interest has recently centered on cellular assemblies featuring a negative Poisson's ratio behavior, also known as auxetics since their first release in 1987. Materials having auxetic characteristics include special subsets of foams, long-fiber composites, and microporous polymers, as well as honeycombs [24]. These materials have found potential applications in several engineering designs; such as damage tolerant laminates, microwave absorbers and medical prosthesis [25]. An auxetic (or negative Poisson's ratio) material expands in all directions when pulled in only one, behaving in an opposite way compared with "classical" materials. In contrast, when a material with a positive Poisson's ratio is stretched, it contracts in the direction of the applied load. In the Figure 3.1, materials with a positive Poisson's ratio and a negative Poisson's ratio are shown.

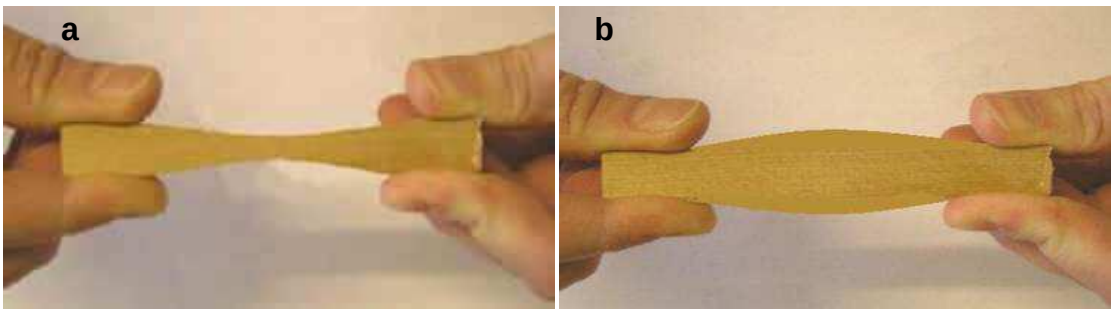

Figure 3.1 – (a) Poisson's ratio (v) >0 (b) Poisson's ratio (v) <0

In honeycombs, the negative Poisson's ratio behavior implies a stiffening geometric effect, which leads to increased in-plane indentation resistance, shear modulus and compressive strength .The auxetic behavior also leads to a sinclastic curvature feature, which is extremely useful in manufacturing curved sandwich shells.

3.1 Honeycomb Structures

Some of the lessons learned from the nature provide inspiration for technological advance as in the case of numerous hexagonal cells within a bee's nest (structural honeycomb) is one of the few examples to mention. The word "cell" derives from the Latin word "cella" meaning a small compartment or enclosed space [26]. When nature constructs things, it is often done from many cells ("cellula"). Wood, cancellous bone and sponge are good examples of this. Let us consider the bovine femur shown in Figure 3.2(a) [26]. It is stiff, strong, lightweight and multifunctional. This is just one of nature's many cellular structures. From these natural inspirations have evolved synthetic cellular solids, as shown in Figure 3.2(b) [26].

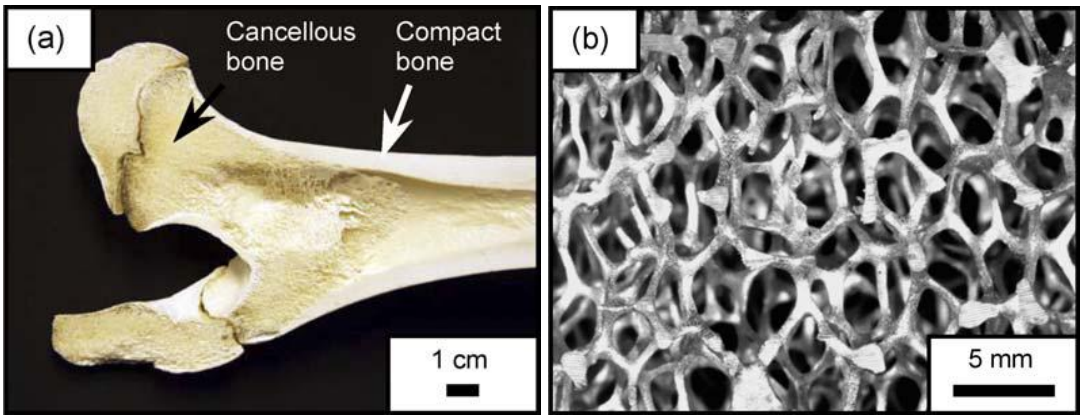

Figure 3.2 – (a) Juvenile bovine femur (b) Synthetic open cell aluminum foam

A variety of synthetic cellular solids have been made including stochastic foams, consolidated powders, vapor deposited materials, hollow sphere structures, honeycombs, prismatic materials, textile laminates and lattice block or miniature truss structures . The most common and least expensive are made from polymers. These have a stochastic cellular architecture and are often used for cushioning, thermal insulation, filtering, structural applications or for their buoyancy property amongst many other applications. Others find application as impact energy absorbers, cores of composite structural panels and even hanging household decorations. Because of imperfections, defects and inhomogeneities, mechanical properties for stochastic foams reside well below those of periodic, less defective cellular structures like hexagonal honeycomb [27].

Synthetic honeycombs are based upon the efficient design of a honeybee's nest. They are often used as the cores of sandwich structures or as impact energy absorbers since they are stiff, strong, light and absorb much energy when crushed in out-of-plane direction. Figure 3.2 shows an aramid – made honeycomb structure. Honeycombs structures could be constructed in many ways; some honeycomb structures have positive Poisson's ratio while some of them posses negative Poisson's ratio thus enabling them to be used as auxetic structures. In the Figure 3.3 two honeycomb structures are indicated; the first honeycomb cell has been designed in such a way that

when compressed in one direction, stretches in the other direction, the other honeycomb structure when stretched in one direction also stretches in the other direction which shows auxetic features.

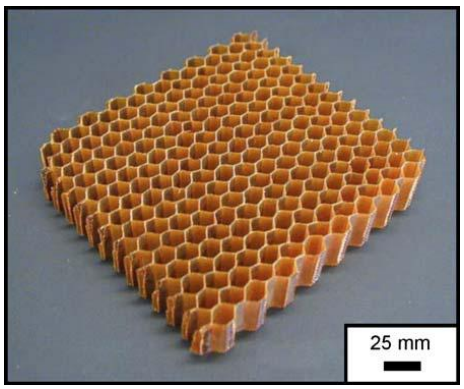

Figure 3.3 – Aramid – fiber reinforced honeycomb

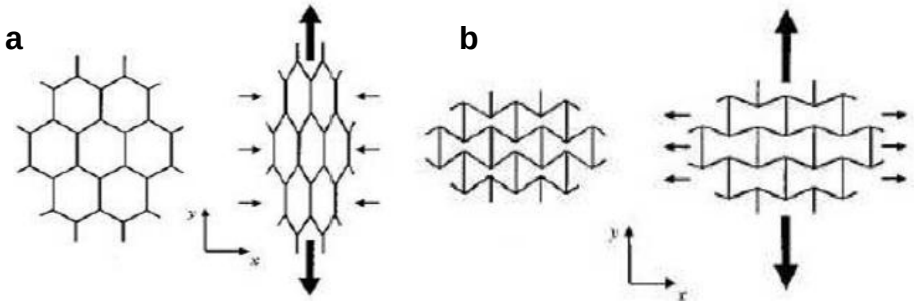

Figure 3.4 – Types of honeycombs (a) Poisson's ratio (v) >0
(b) Poisson's ratio (v) <0

3.2 Chiral Structures

A structure not super – imposable with its mirror image is defined as chiral. The word "chiral" is a terminology coming from biology. Chiral topologies represent an attractive solution for deformable internal frame of morphing structures. The chiral geometry is a non – centrosymmetric topology composed of circular elements (nodes) of equal radius joined by straight ligaments, which are at a tangent to the nodes. A chiral honeycomb features auxeticity i.e. a negative Poisson's ratio behavior in the plane. The first study of a structural chiral honeycomb has been reported by Prall and Lakes [28]. Figure 3.5 shows an example of a hexachiral topology with the main geometrical parameters highlighted. The parameters defining the chiral geometry are R, L, β, t_b and t_c that denote the distance between the centre of the nodes, the ligament length, the angle between the imaginary line connecting the circles and a ligament, thicknesses of the ligament and the node respectively [29].
These parameters are related as follows: tan β = 2r/L, sin β = 2r/R. The chiral geometry is significantly altered by changes in L/R (L/R = cos β) here denoted as the ''topology

parameter", which in turn strongly affects the mechanical behavior of the proposed truss – core airfoils.
The in – plane deformation mechanism of the honeycomb is provided by the rotation of the nodes which leads to bending and axial deformation of the attached ligaments.
Several experimental studies conducted on the chiral units have shown that the in – plane Poisson's ratio of this cellular solid remains substantially constant up to 25 per cent of applied strain in one principal direction, while the honeycomb structure recovers almost entirely its original dimensions [24]. The high deformability yet with a high in – plane shear resistance (Poisson's ration is equal to -1 theoretically), could constitute a design solution for wing boxes of morphing wings.

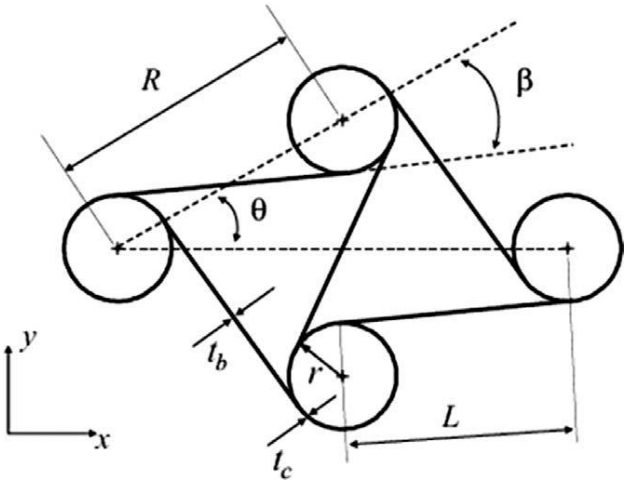

Figure 3.5 – Chiral topology

Although the theoretical Poisson's ratio of the hexagonal chiral unit is equal to -1, practically it is less than this value. The following equation gives the shear stiffness G, for an isotropic material.

$$G = \frac{E}{2(1+v)} \qquad 3.1$$

Where E is Young's modulus and v is the Poisson's ratio

As the Poisson's ratio is theoretically -1 for a hexagonal chiral unit, the expression becomes infinite. In practical applications the shear stiffness is relatively high because denominator part of the fraction becomes very small as the Poisson's ratio is close to -1. The geometry and the shape of the hexagonal chiral unit determine the configuration of the assembly and define its physical properties. Prall and Lakes have studied the in – plane properties of an isotropic chiral unit with an internal angle θ = 30º. In their study, they considered cells with t_b = 0.25 mm, R = 32mm, r/R = 0.2 and t_c = 1.25 mm. The analytical model developed to predict the in – plane Young's moduli and Poisson's ratio was validated experimentally using a 305x355 mm polystyrene model. From the test results, Prall and Lakes could verify that the considered configuration is isotropic in the

in – plane (z direction is out – of plane, x and y directions are in – plane, $E_x = E_y$ and $v_{xy} = v_{yx}$), featuring a negative Poisson's ratio behavior with $v_{xy} = v_{yx} = -1$ while the Young's moduli E_x and E_y strongly depend on ligament wall thickness t_b and r/R ratio.
Defining $\beta = t_b / r$ the relative density of the honeycomb and $\alpha = L/r$ the unit cell aspect ratio, the in – plane Young's modulus of the hexagonal non – centrosymmetric chiral honeycomb is expressed by the relation

$$E_x = E_y = E_s \frac{\sqrt{3}\beta^3}{2\ \alpha} \qquad 3.2$$

Where E_s is the Young's modulus of the core material composing the honeycomb elements. Equation 3.2 is physically consistent with the in – plane properties of centrosymmetric cellular structures because of the cubic dependence of the relative density β. In fact, hexagonal – like structures have a relative density defined as the ratio between the cell wall thickness and cell wall length.

4 Production, Testing and Analysis of Chiral Unit

In this chapter both the technological and numerical studies that were carried out for the design and the production of the hexagonal chiral units will be explained. After the manufacturing process, several tests have been performed to estimate the mechanical behavior of the structure and to validate the modeling approaches. The strength and the compliance of such chiral composite elements have been assessed by means of tensile and compressive cycles performed at very low velocity. Moving from these results, the research acted on the identification of the design configuration for a morphing vertical empennage that was studied from the aero dynamical and structural point of view in a previous work [30]. Optimization process has been carried out to maximize $C_L - \alpha$ by using the airfoil profile of NACA0018 and several parameters were optimized by using numerical calculations. The production technology for the chiral units is based on the technological knowledge that was acquired before. In the previous attempts, larger chiral units were obtained; these hexagonal units were produced without any optimization, nodes and ligaments were separately produced and then bonded together in a second assembly phase. A second attempt was realized to produce only the ligaments and to obtain the nodes by superimposing the ligaments onto each other. The optimization process made the chiral unit smaller and the production technology of the second attempt was used i.e. producing only the ligaments and then superimposing two ligaments onto each other in which the ligaments are put around a circular cylinder to complete the node and a ligament follows another ligament in a 60º circular path.

4.1 Design and Production of the Chiral Unit

As stated before a honeycomb structure with a chiral topology will behave, at the macro scale level, as an auxetic material (the composite materials like carbon or glass fibers do not exhibit auxetic features but the geometrical structure behaves like an auxetic material at the macro scale level) with a negative Poisson coefficient that can be close to the theoretical limit -1.
An important consequence of such response on the mechanical properties is an expected increment of the shear modulus, in accordance with the relation $G = E/2(1+\nu)$. The relatively higher shear modulus causes the opposition of the structure to the distortion of chiral units; such behavior can be effectively exploited for morphing purposes. In fact, if a displacement is applied to a structure having a chiral core, the local inherent resistance to shape change will lead to a diffused strain state over the entire core, without strain localizations in the weak points of the structure.
Such considerations are at the basis of the employment of chiral structure for morphing airfoils. The experimental activities performed on chiral structures, which have been manufactured to show morphing capabilities, confirmed that such structures can undergo large displacement while keeping the maximum strains at acceptable levels.
One of the features of the chiral topologies is the design flexibility that can be obtained by changing the geometrical parameters as well as the ligament thickness and material. Such flexibility allows a fine regulation of structural compliance in order to meet different morphing and global stiffness requirements.
The purpose of the optimization for the morphing sail was to find the set of parameters that maximize the slope of the airfoil lift – curve slope, C_L – α, for the compliant configuration. In order to accomplish the optimization process three basic points should be ensured:

- Aeroelasticity of the airfoil for the required stiffness
- Aerodynamic loads to ensure the performance of the airfoil
- Strength of the whole structure

The design parameters are a set of topological and material variables. In particular, the response of the morphing airfoil is evaluated as function of:

- r and L geometrical dimensions of the chiral unit; which yields the miniaturization
- x_F and x_A fore and aft spar positions that limit the extension of the chiral box; the locations of Leading Edge (LE) and Trailing Edge (TE) spars
- x_{pF} and x_{pA} fore and aft positions of the ground pin points
- n_c and n_s, the number of composite plies used respectively for the ligaments and the skin, in order to influence the structural stiffness

The optimization process was carried out taking into account the operative speed for the system is 50 m/s which comes from the knowledge of the speed of the wind tunnel belonging to the Department of Aerospace Engineering, Politecnico di Milano. The parameter values obtained in the optimization process is shown in Table 4.1. The CL – α curve, shown in Figure 4.1, shows that for low angle of attack the $C_{L\alpha}$ is almost doubled. For values of α higher than 6°, a reduction of the slope is observed due to the beginning of a smooth separation at the trailing.

Table 4.1 – Optimization parameters ranges and optimal values

Parameter	Min	Max	Optimal
x_1, [%]	0.075	0.225	0.200
x_2 [%]	0.540	0.900	0.900
r [mm]	7.200	14.400	10.300
L [mm]	18.750	37.500	19.300
x_{g1} [%]	0.0500	0.95* x_1	0.120
x_{g2} [%]	1.05* x_2	0.950	0.780
n_c	2	10	5
n_s	2	6	2

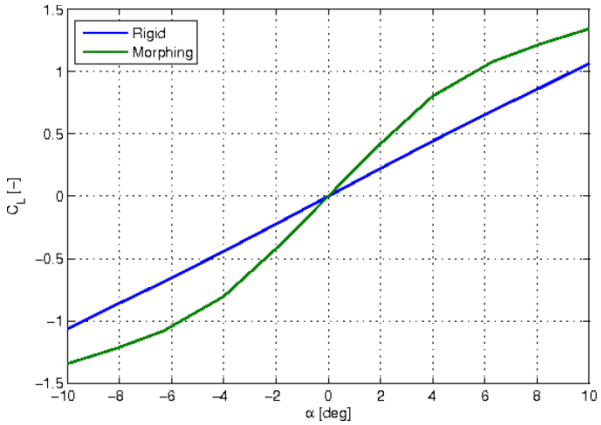

Figure 4.1 – C_L – α curve for the optimized section

Chiral units based on chiral topologies could be developed by utilizing the technological process developed by Bettini et al. for the manufacturing of chiral honeycombs made of carbon/glass composite laminates [29]. The original of the process was developed for relatively large chiral unit cells with L = 75 mm and r = 18 mm, while the new optimized solution has a smaller miniaturized configuration with dimensions of L = 19.3 mm and r = 10.3 mm. The first attempt for obtaining relatively larger chiral unit was made by the production of ligaments and nodes separately and then bonding them in a final phase. In order to simplify the process a new methodology was realized; only the ligaments were produced and nodes were obtained by superimposing the ligaments onto each other. This new technological method was also used for the miniaturized chiral units. In the Figure 4.2 two chiral units could be seen; the first one was obtained by producing the ligaments and nodes separately and bonding them to form the assembly while the second one was obtained by producing only the ligaments and bonding them by superimposing the ligaments in a second step to form the nodes.
The process that was developed before consists of a step for the production of thin curved laminates according to the classical vacuum bag technology and a subsequent phase to assemble and bond the laminates to obtain the chiral topology. Such a process has been refined and set up for the application to the miniaturized chiral geometry, which is characterized by a significantly smaller size of ligaments. In

particular, the technological activities have been aimed at producing chiral units, which have been subsequently tested in order to investigate their performances and to validate the numerical approaches applied in the technological demonstrator design.

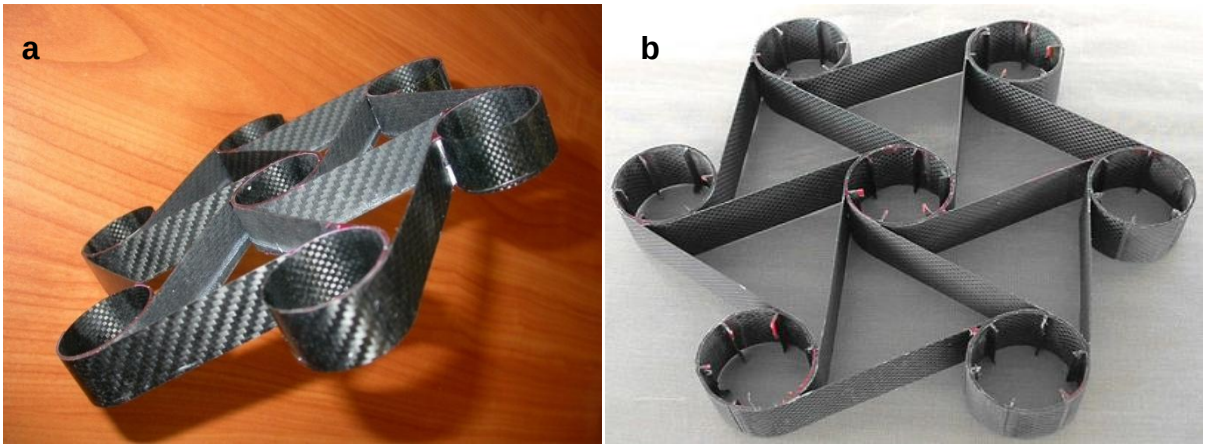

Figure 4.2 – Chiral composite unit made of CFRP (a) Ligaments and nodes separately produced (b) Only ligaments produced

Relatively higher stress values are generated on the ligament's straight section compared with the node section; it was intended to decrease the number of plies on the node by dropping – off several plies in the curved region of each ligament. Such modification brings a considerable weight saving, but the strength of the configuration has to be assessed. In order to realize the drop – off, several plies were laminated only on the straight section of the mold and the remaining plies were laminated as complete. This procedure does not yield a precise tapering because of sudden drop – off but reliable enough in a relatively thin section to guarantee stress – concentrating free spots.

The production process consists of three steps:

1. The production of ligaments (Figure 4.3 (a), (b)) by means of a conventional vacuum bag technology by using prepreg composite laminates
2. Pre-assembly of ligaments (without adhesives) and forming of elastomeric rubber mold (Figure 4.4 (a),(b))
3. Final bonding process with the help of autoclave (Figure 4.5)

Two molds for ligament production were designed and manufactured taking into account the tapering of the ligaments. The first mold is double sided and the second one is one sided. In order to increase the production rate, double sided mold which has two surfaces and a wider dimension (50 cm in width while the first mold is 35 cm wide) was produced. The molds were cleaned by acetone and release agents of two types were applied on the surfaces of the molds to secure the release of the cured plies from the molds after the autoclave process.

The first phase of the production is the lamination of composite plies onto the molds of the ligament. Composite plies in different orientations and several ply numbers were laminated.

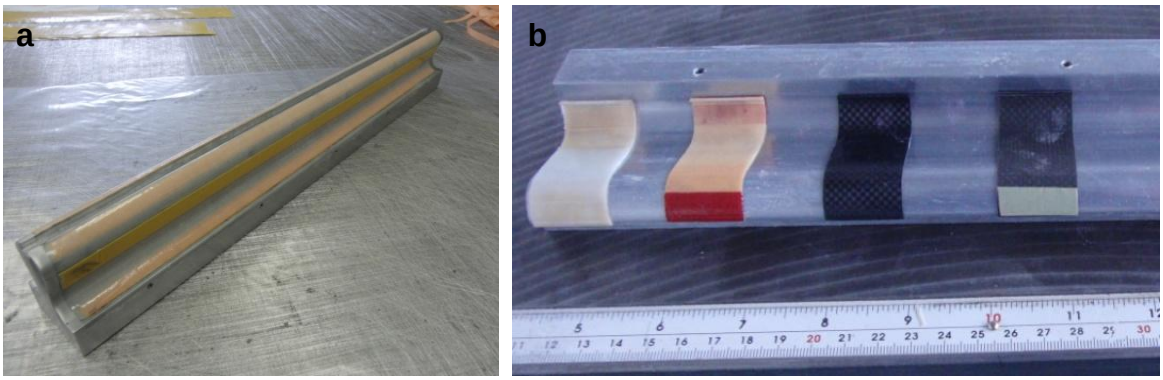

Figure 4.3 – (a) GFRP laminates on the ligament mold (b) GFRP and CFRP ligaments on the ligament mold

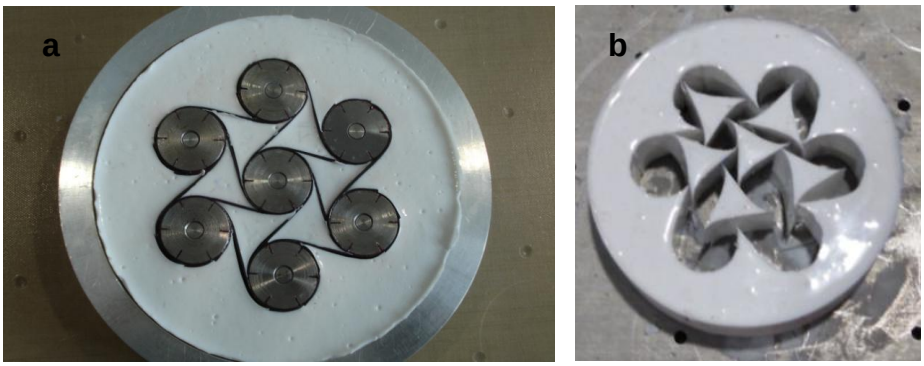

Figure 4.4 – (a) Pre – assembly of the chiral unit and elastomeric rubber insert (b) Formed elastomeric rubber insert

The long ligament piece would be cut into smaller pieces (25 wide) for the assembly of the whole chiral unit. By using both ligament molds, several ligaments were produced enough for four chiral cells. Carbon Fiber Reinforced Polymers (CFRP) and Glass Fiber Reinforced Polymers (GFRP) were used for production of chiral units. Table (Table 4.2) shows the configuration of each chiral unit whereas Table (Table 4.3) summarizes some of the properties of these materials. A total of four chiral units were produced.

Two CFRP chiral unit cells were produced with an orientation of 0 – 90° (cross ply), the first one is laminated with seven plies and the second one is laminated with three plies only. GFRP chiral unit cells have somewhat different orientations; the first cell was made by seventeen plies with 0 – 90° (cross ply) and the second cell was made by ten plies with +45 /-45° orientation.

In order to produce a ligament, several plies in different dimensions were cut. According to the FEM results seven plies on the straight part and six plies on the ligament node (because of drop-off in the curved region) is the optimized solution for CFRP. So a total of seven plies were cut; three plies of 70 mm and four plies of 16 mm. Later one of the 70 mm ply was reduced to 58 mm in order to decrease the thickness of the ligament extension so that the extension could be inserted into the slot of the cylinder without any problem. The plies with a length of 16 mm were used in order to create the tapering in the node section of the ligament. After all the ligaments were laminated on the mold, the

mold was put into the vacuum bag for about five minutes to guarantee the void free lamination and better sticking of all plies. The design of the vacuum bag for the autoclave process was carried out as it is shown in figure (Figure 4.6).
The placement of peel plies were of great importance in order to obtain the convenient roughness on the material surface. Peel plies were laminated on the material surfaces where there would be the implementation of the structural adhesive or two

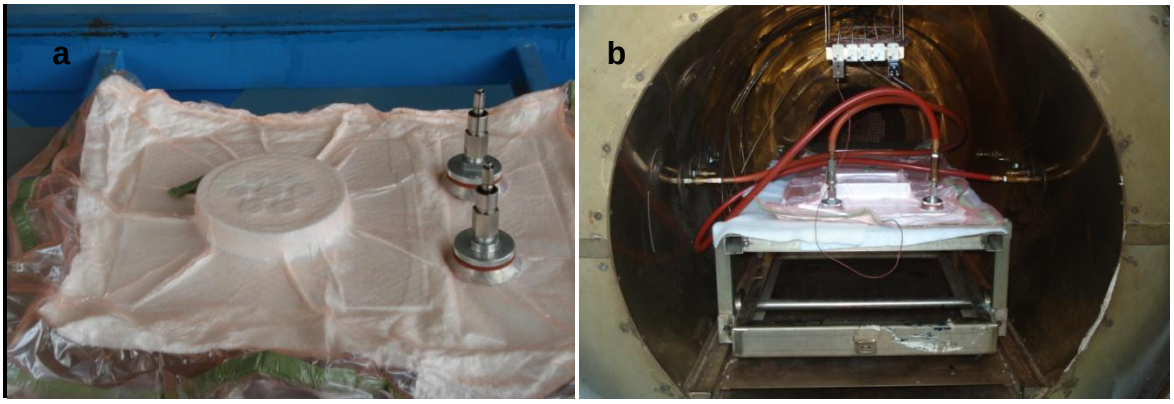

Figure 4.5 – (a) Chiral cell assembly inside the vacuum bag (b) Vacuum bag inside the autoclave

Table 4.2 – The configuration of chiral cells

Material	**Ligament thickness(thickness at the straight part)**	**Lay-up**	**Drop-offs**
CFRP (stiff)	0.70 mm	$[\text{cross ply}]_7$	4 drop offs(3 plies in the curved section)
GFRP (stiff)	0.95 mm	$[\text{cross ply}]_{17}$	10 drop offs(7 plies in the curved section)
CFRP(compliant)	0.30 mm	$[\text{cross ply}]_3$	1 drop off(2 plies in the curved section)
GFRP(compliant)	0.50 mm	$([+45][-45])_{5S}$	6 drop offs(4 plies in the curved section)

Table 4.3 – Some of the properties of prepreg materials used

Material	**Cured ply thickness**	**Young modulus($E_{11}\approx E_{22}$)**	**Resin content**	**Poisson's ratio(v_{12})**
E glass	0.055 mm	22 GPa	%60	0.2
Carbon	0.1 mm	56 GPa	%48	0.05

superimposed ligaments were in contact with each other. The remaining surfaces were peel ply free. After the production of the first ligament it was seen that the surfaces close to the ligament extension section had some defects. The accumulation of resin in some regions was clearly visible. A counter flexible mold made from an elastic material that could be used inside the autoclave was produced to exert pressure on the surfaces of the prepreg material. The following Figures (Figures 4.7 (a) and (b)) show an illustrated drawing of a ligament mold where the peel plies are located and the figure of a flexible counter mold on the top of the ligament mold.

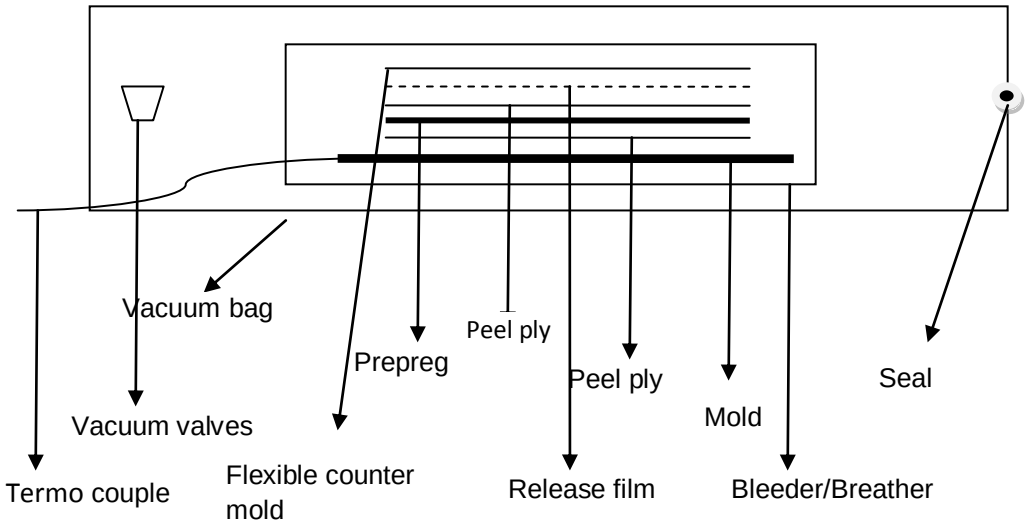

Figure 4.6 – Vacuum bag lay up for prepreg material

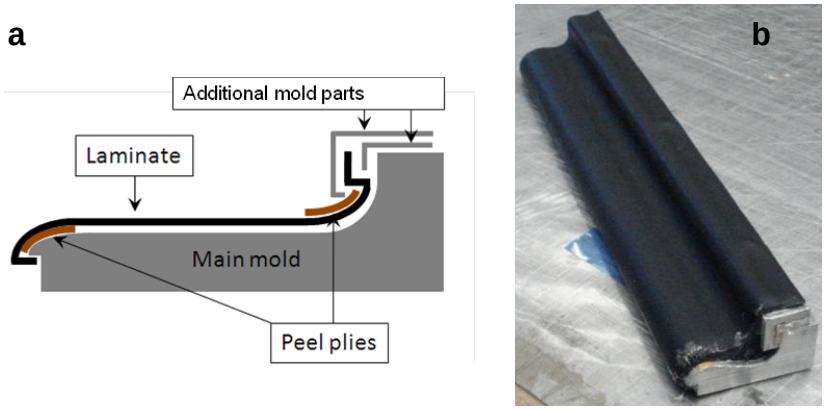

Figure 4.7 – (a) The ligament mold and the location of peel plies (b) Flexible counter mold

For the two subsequent phases of unit production, two chiral cell assembly molds have also been produced. The assembly molds consists of a light alloy plate, with lateral

dams, and a series of placement cylinders, which are shown in Figure 4.4 (a). In the second phase of the technological process a set of elastomeric rubber insert were produced. The inserts, shown in Figure 4.4 (b), are fundamental for exerting an adequate and uniform pressure during the final bonding process, which join the ligaments together and forms the chiral network. This insert was formed by using the same mold and then introduced into the gaps of assembly after the ligaments are put to their dedicated spots while the adhesives are mounted on them. The assembly is then accommodated into a vacuum bag and adhesive is cured inside the autoclave by applying pressure-heat cycle. The elastomeric rubber insert has a considerable Coefficient of Thermal Expansion (CTE) and provides pressure on the adherents during curing. Variable volume method exploits the large difference between the CTE of the elastomeric rubber and the CTE of metal [31]. This method ensures that the internal pressure of autoclave is transferred to the adhesive passing through the rubber. Bonding is obtained by means of structural adhesive tapes, which are placed between two superimposed ligaments. The first phase for the production of this elastomeric rubber mold was the assembly of ligaments.

To form a unit chiral cell which is composed of seven nodes (one inner node and six outer nodes), full ligaments and curved sections of the ligaments are needed. As a chiral unit has seven nodes and only the central node is made by superimposing the full ligaments onto each other by an angle of 60° while six other nodes are made by superimposing three full ligaments and three curved sections of the ligaments onto each other. The ligament configuration for a chiral cell is described below, this gives us the total number of ligaments we need for a chiral unit. From Figure 4.2 (b), it can be seen that there are six inner and six outer full ligaments; total number of full ligaments is twelve. For each outer node three curved sections of the ligaments are also needed. For six outer nodes 18 curved sections of the ligaments are needed. As two curved sections of the ligaments could be obtained from one full ligament, a total of 9 full ligaments are needed for the outer nodes. For a complete chiral cell 21 full ligaments are needed. Each curved sections of the ligament covers 60° around a node.

After the ligaments were put into the mold of the assembly by inserting the extensions of the composite ligaments (no structural adhesive was mounted on the ligaments yet) inside the slots of cylinders, silicon rubber was poured inside the mold of the assembly by using an injector. The mixture was then left for vulcanization for eight hours. After the silicon rubber became solid elastomeric silicon mold was cut into pieces in order to remove the rubber out of the chiral cell assembly easily. The elastomeric rubber mold was intended to generate pressure on the adherents during bonding process inside the autoclave. The pre – assembled ligaments in the chiral unit assembly mold were removed after the production of elastomeric rubber mold to apply the structural adhesive on the surfaces of each ligament (both full ligaments and curved sections of the ligaments were applied with adhesive strips). The adhesive structural strips were mounted on the outer section of each ligament close to the ligament extension to ensure that when the pressure and heat would be applied, the adhesive layer would stick two ligaments together. After the assembly of all ligaments with adhesive strips, elastic rubber mold was placed again to be put inside the autoclave.

Two versions of the assembly mold were produced. For the first assembly mold two 5 mm cylinders in height for each node with 0.3 mm wide electro – erosioned slots were

used. For the second assembly mold, one 25 mm cylinders in height for each node with 0.5 mm wide electro – erosioned slots were utilized. The dimension of 0.3 mm for the slots of the cylinders were improved and increased to 0.5 mm for the second cell after having seen that the extensions of composite ligaments that enter these slots were experienced difficulty while inserting them inside these slots. 25 mm cylinders in height were used after it was observed that the product of chiral unit assembly that has two 5 mm in height cylinders had some imperfections in the outer cylinders.
During the bonding process in the autoclave, pressure exerted on the composite part distorts the nodes of the chiral cell. For the case of using two 5 mm cylinders, there is a 15 mm gap between the two cylinders. This gap is susceptible to distortion when an external pressure is exerted on the nodes of the chiral cell. For the final version, two molds of chiral cell assembly were produced to increase the production phase so that two assemblies could be put together inside the autoclave.
The third step in the production phase of the chiral unit is putting the assembly of the ligaments inside the autoclave while the adhesive strips are on for the final bonding process. The following Figures (Figures 4.8, 4.9 and 4.10) define the autoclave curing cycles for CFRP, GFRP and structural adhesive material used for the bonding of two superimposed ligaments [32,33].

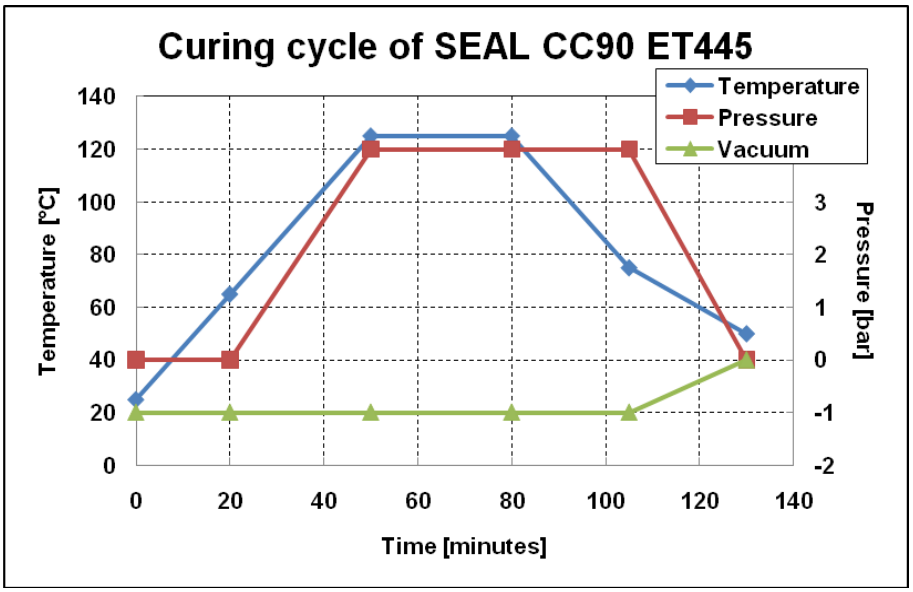

Figure 4.8 – Curing cycle of CFRP

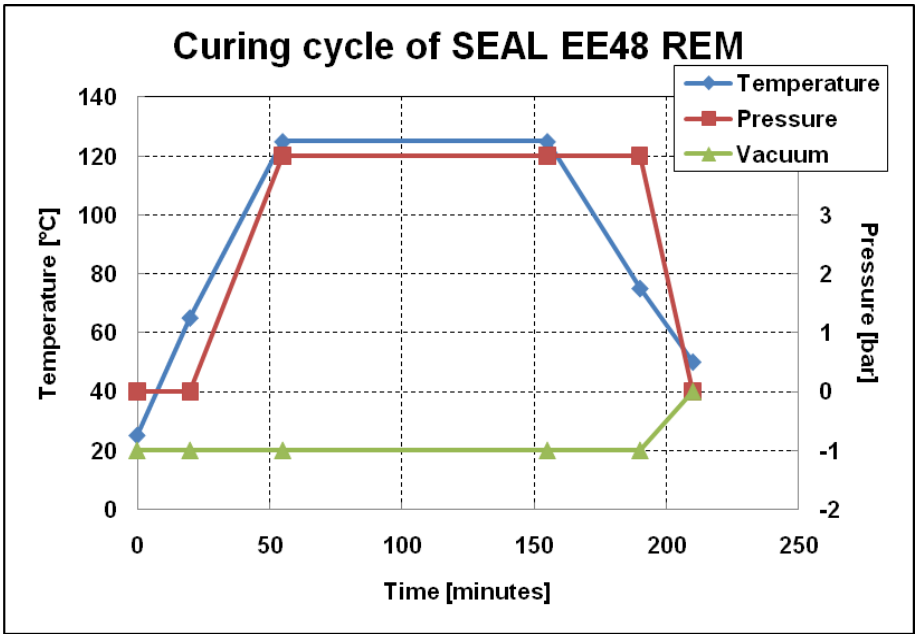

Figure 4.9 – Curing cycle of GFRP

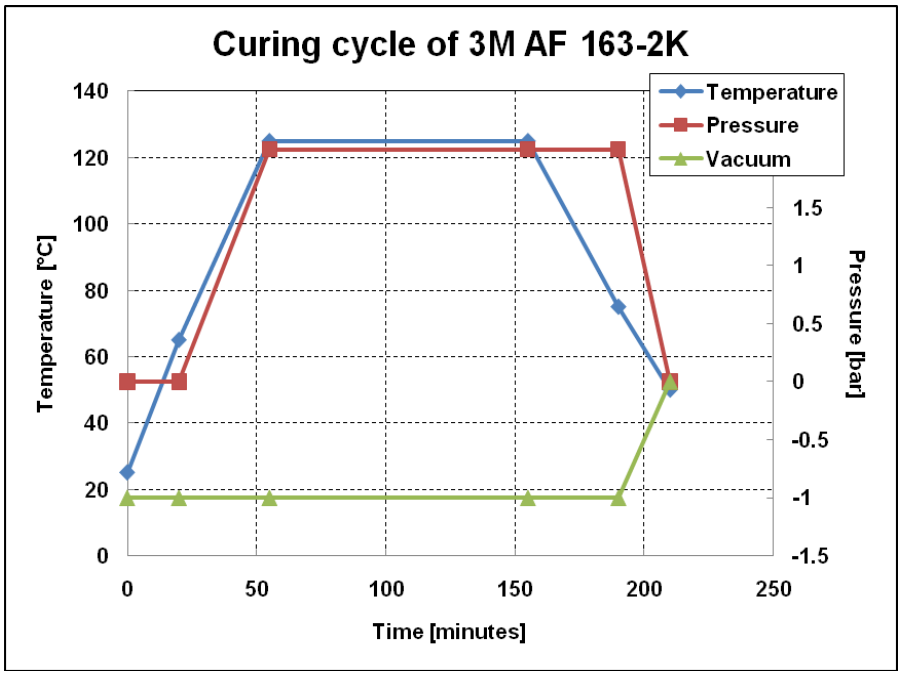

Figure 4.10 – Curing cycle of structural adhesive

After the production phase is completed, some drawbacks of using the metallic cylinders could be seen during the extraction of the chiral units from the assembly mold. The residuary amount of resin could be problematic between the cylinders and the nodes as the resin sticks on the metallic cylinders and this prevents the chiral cells to be

separated from the assembly mold easily. A remedy to this problem was implemented; using PTFE (Teflon) made cylinders instead of metallic cylinders in the assembly mold. In the Figure 4.11 two produced chiral units could be seen; the first one is made from CFRP and the second one is made from GFRP.

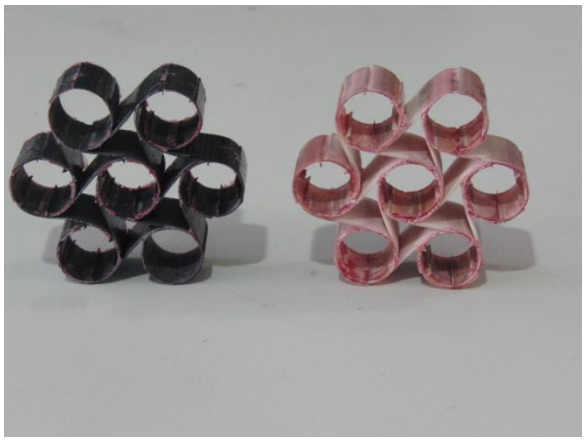

Figure 4.11 – Two chiral units made of CFRP and GFRP

4.2 Testing of Chiral Unit

As already said, a total of four chiral units were produced. They were tested considering the results of the previous tests with larger cells. The main objectives of the experiments were the following:

- To assess the mechanical response, changing the thickness of the plies, material and orientation
- To demonstrate the ability of the cells to undergo significant global displacements with limited local strains
- To study the possible non – linear deformation modes and weak points
- To build a database to be used for the numerical/experimental correlation
- Evaluation of stiffness in linear range for assessment of numerical approaches

Tension and compression tests were carried out at relatively low speeds in order to obtain the stiffness curve for each unit. The testing machine was MTS 858 and a displacement rate of 1 mm/min was used to avoid the effects of a dynamic deformation and to reproduce quasi-static loading condition. The constraints between the chiral cell and the testing machine were realized by means of two pins, inserted in the upper and the lower nodes; this method ensures that the cylinders are free to rotate about their axis, which is also the main requirement for the operating condition of the real structure. Also, it helps to avoid stress concentrations and non – realistic deformations. During the tests the lower pin was fixed to the ground while a vertical displacement is enforced to the upper cylinder; for each displacement step a force is sampled by means of a load cell positioned in the upper part of the testing system. Gripped nodes were filled with epoxy resin in stiffer specimens while metallic cylinders were used in thinner specimens. Using two identical cylinders in the pins of the assembly mold for housing

curved section of the ligament caused distortion of the nodes of the chiral unit during the autoclave process under pressure. This practice was later abandoned by replacing two 5 mm identical cylinders for each pin with 25 mm monoblock cylinders to be used in the same pin. Realizing metallic cylinders in the nodes of the thinner chiral units and epoxy resin in the nodes of the thicker chiral units are shown in Figure 4.12 (a) and (b).
The Figure 4.13 (a) and (b) below were taken during the testing of some chiral unit cells. Only the stiff cells were tested until tensile failure. Ligament unwinding can cause debonding in tension. As was expected chiral cells under compression loading

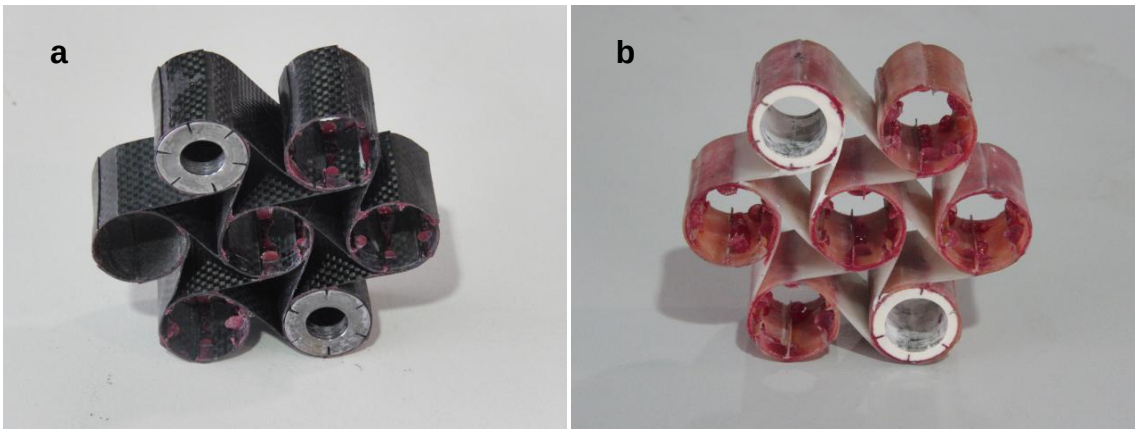

Figure 4.12 – (a) Chiral unit with metallic cylinders for fixing to the test machine
(b) Chiral unit with epoxy resin bushings for fixing to the test machine

showed more displacement without failure compared with tension loading. Carbon stiff unit showed the highest strength levels in the same displacements. After the first failure of stiff cells during tension, loading dropped considerably and second failure was observed for higher displacements levels. The displacement levels range from -10 mm for compression and +10 mm for tension. The highest force that was experienced to be around 400 N which was the case for 7 plies CFRP cell. In each test, force and displacement values were recorded. Figure 4.14 (a) and (b) show graphs of displacement versus force for four chiral cells. In the first graph, values of GFRP cells are given while second graph shows the values of CFRP cells. As it can be seen for the GFRP stiff cell, the first failure was experienced when the displacement was less than 2 mm. Second and third failures were observed for the same stiff cell. However, the compliant GFRP cell did not experience any failure even in the higher displacements both for tension and compression. The second graph indicates displacement versus force for two CFRP chiral cells. Carbon made stiff cell has its first failure in a higher force compared with the glass made stiff cell. The first failure was experienced in about 3.5 mm and a sudden drop in the loading was seen for this cell. Large displacements were obtained for compliant CFRP cell without any failure as expected.

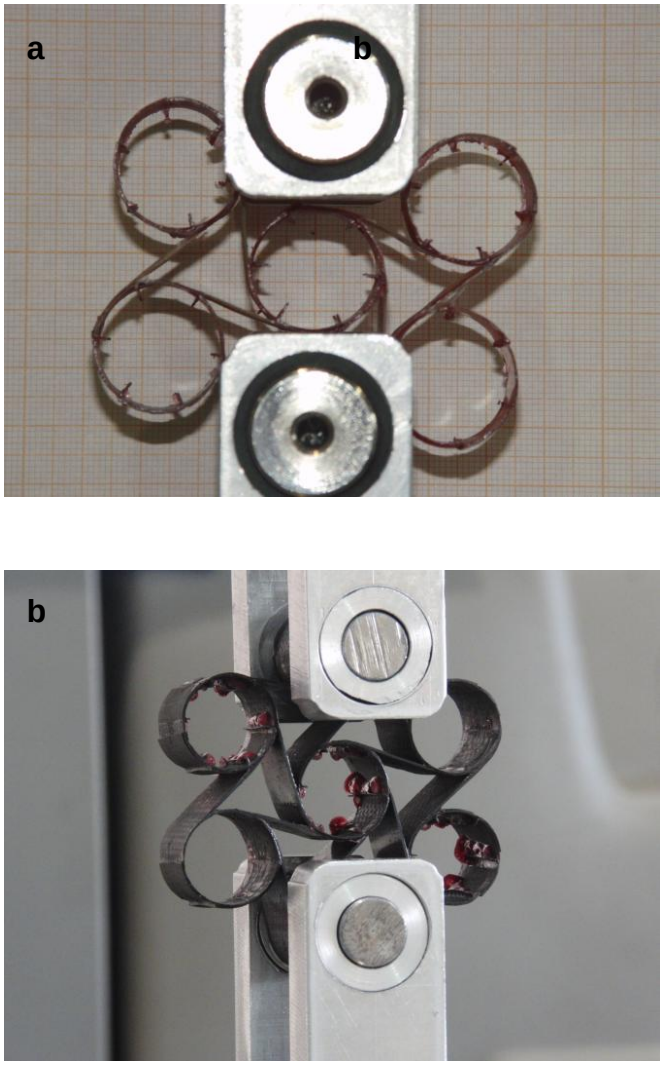

Figure 4.13 – Chiral unit cells under tension – compression testing (a) GFRP chiral unit (b) CFRP chiral unit

In the following table (Table 4.4), a summary of the results of the tension – compression testing is given. The table gives the values and the percentage rates for the maximum strain levels.

Table 4.4 – Summary of the maximum strains of the tested chiral units

Test Number	Chiral Unit	Compression		Tension	
		D (mm)	ε (%)	D (mm)	ε (%)
1	GFRP$([+45][-45])_{5S}$	10	13.3	7.25	9.7
2	GFRP$[\text{cross ply}]_{17}$	2	2.7	2	2.7 (ruptured)
3	CFRP$[\text{cross ply}]_{7}$	3	4	3.54	4.7 (ruptured)
4	CFRP$[\text{cross ply}]_{3}$	2.85	3.8	3	4

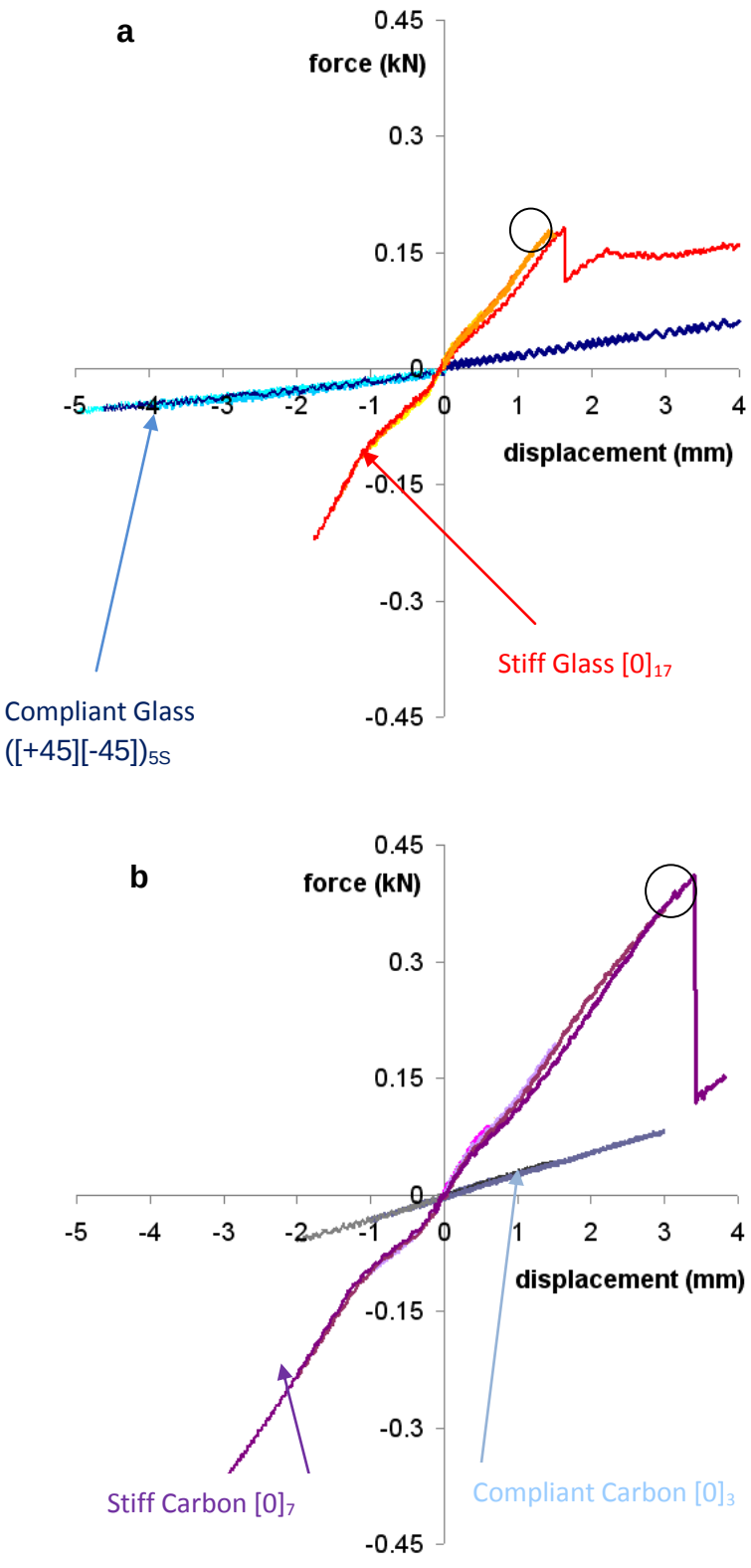

Figure 4.14 – Displacement versus force during tension – compression testing of chiral units

4.3 Analysis of Chiral Unit

Abaqus is used for numerical modeling by using second order shell elements while their sections are defined specifying the materials and the lamination sequences (thickness and orientation of each ply). The properties of the materials are defined directly through the stiffness matrix of the single composite orthotropic lamina. In the testing, pins were used to connect chiral cell to the test bench from the upper and lower nodes. In the FEA, pins were modeled by beams and kinematically coupled to upper and lower cylinders (rotations allowed). Some geometrical difficulties between real model and FEA model have given rise to geometrical nonlinearities. This caused the discrepancies for the FEA model. In the Figure 4.15, discrepancies for the FEA model of CFRP and GFRP chiral cells could be seen. The geometrical nonlinearities are listed as below:

- Structural adhesive between two superimposed ligaments have not been modeled
- Drop – off is tapered in the real model (continuous reduction from straight section to the beginning of the node section) while FE model assumes instant drop – off only in the node section
- Thickness along the ligament is not same in the real model. Accumulation of resin makes some sections thicker while some regions become thinner because of resin depletion. FE model does not take the thickness variation into account; the same thickness is expected in the whole sections

Figure 4.16 shows the finite element model of the chiral unit cell. A mesh sensitivity analysis, by using two different refined models, was performed to check whether there is a significant difference between the results. In the Figure 4.16, the meshed model is shown with its fourteen elements through the direction of the thickness of the chiral unit cell. Table 4.5 is also formed to compare the vertical displacements based on the same criteria.

Non – linear analyses were performed to compare the results with the linear ones; in these analyses only geometrical non – linearities were taken into account. The results showed that the non – linear cell model is stiffer in tension and more compliant in compression. It is to be noted that these differences are significant only for large displacements. The loading procedure is different in non – linear analysis as the loading is given in an incremental way instead of an instant loading as it is the case in the linear analysis. In the Figure 4.17, force versus displacement is demonstrated for the linear and nonlinear analyses for the comparison purposes.

As it can be seen from Figure 4.18; the deflection is almost pure bending. Deflection in a given point on the curve can be formulated as following [34]:

$$\delta = Kt^{-2.939} \qquad 4.1$$

Where δ, K, t are deflection, constant and thickness of the ligament, respectively.

Such a polynomial form can be interpreted considering the deflection in a single cantilever beam, which can be rewritten as:

$$\delta = FL^3/3EI \qquad 4.2$$

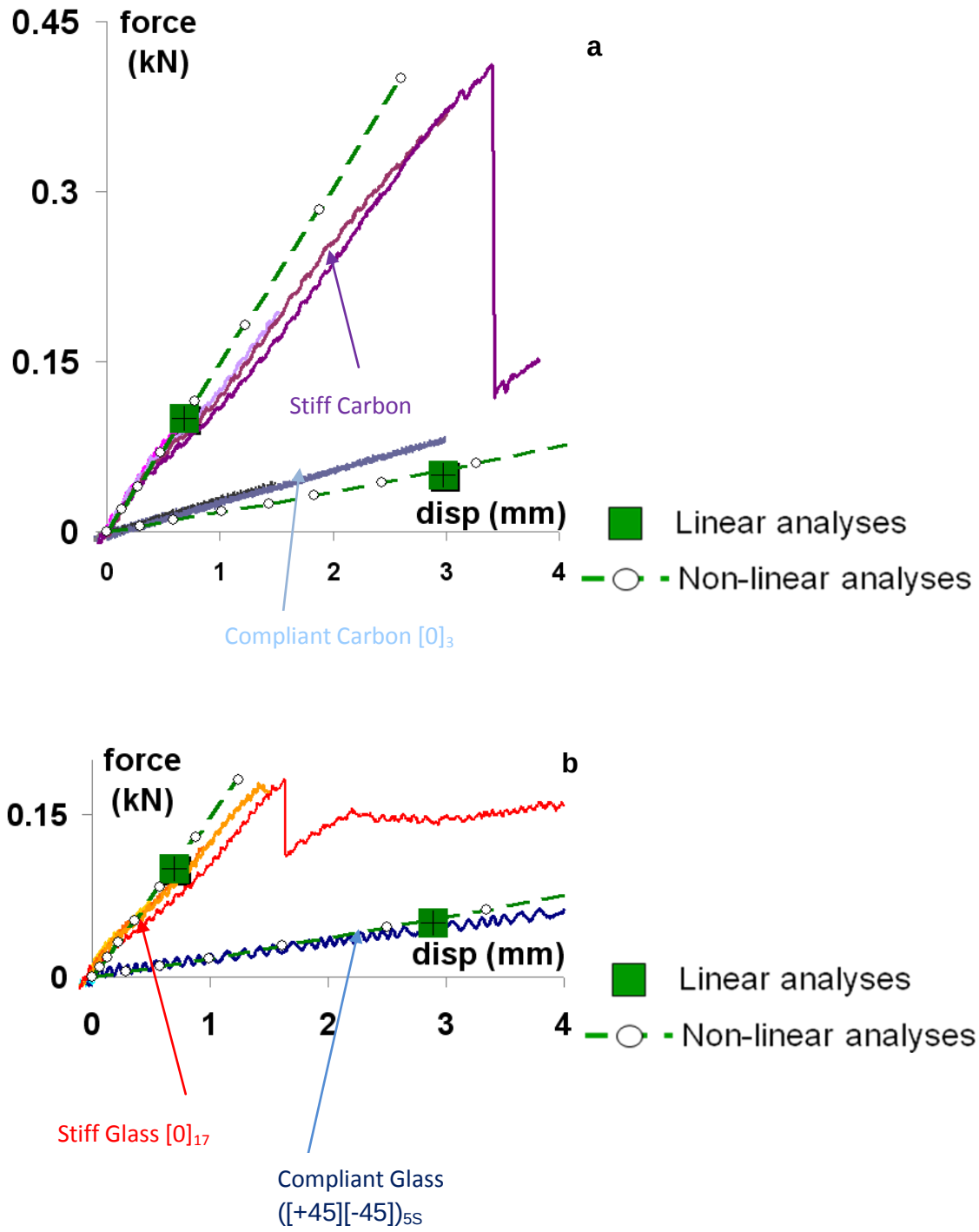

Figure 4.15 – Comparison of numerical results with testing (a) CFRP chiral units (b) GFRP chiral units

Where δ, F, L, E, I are deflection, force, length of the beam, Young's Modulus, moment of inertia of the beam, respectively.
Moment of inertia of the beam for a rectangular section can be expressed as:

$$I = bh^3/12 \qquad 4.3$$

Where h is the dimension in the plane bending of bending, i.e. in the axis in which the bending moment is applied and b is the second dimension.
In our case h becomes t which is the thickness of the ligament.
Deflection becomes:

$$\delta = 4FL^3/Eb\,t^3 \qquad 4.4$$

$4FL^3/Eb$ can be rewritten as K and the deflection becomes,
$\delta = K/t^3$ which is the same as $\delta = Kt^{-3}$

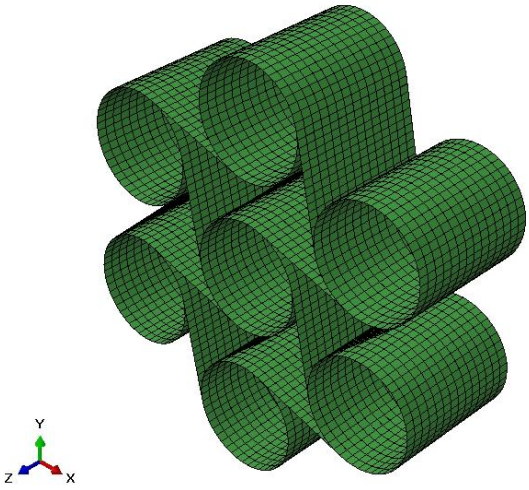

Figure 4.16 – Finite element model of the chiral unit

Based on the results of the numerical studies some conclusions could be obtained:

- Results indicate that numerical compliance is governed by ligament bending stiffness
- Numerical-experimental correlation using nominal cured ply thickness is acceptable
- Linear approaches are suitable for design purposes at moderate deflection levels
- Models can be used to investigate stress fields at failure load levels
- For failure stress is higher than 600 MPa in the stiff carbon unit and more than 150 MPa for stiff glass unit: failure occurs by debonding, but the strength potential of ligaments is well exploited

- Unwinding moments in the ligaments at failure are more than 50 N/mm for carbon stiff unit and more than 20 N/mm for glass stiff unit (Figure 4.19 (a), (b)): such values can be taken as a reference to evaluate the risk of debonding in a more complex chiral structure

Table 4.5 – Results of the mesh sensitivity analysis

Cell	N. of elements through thickness	Vertical displacement [mm]
CFRP $[0°/90°]_3$	7	6.136
	14	6.525
CFRP $[0°/90°]_7$	7	0.6461
	14	0.6848
GFRP $[0°/90°]_{17}$	7	0.7187
	14	0.7634
GFRP $[\pm45°]_7$	7	13.25
	14	14.15

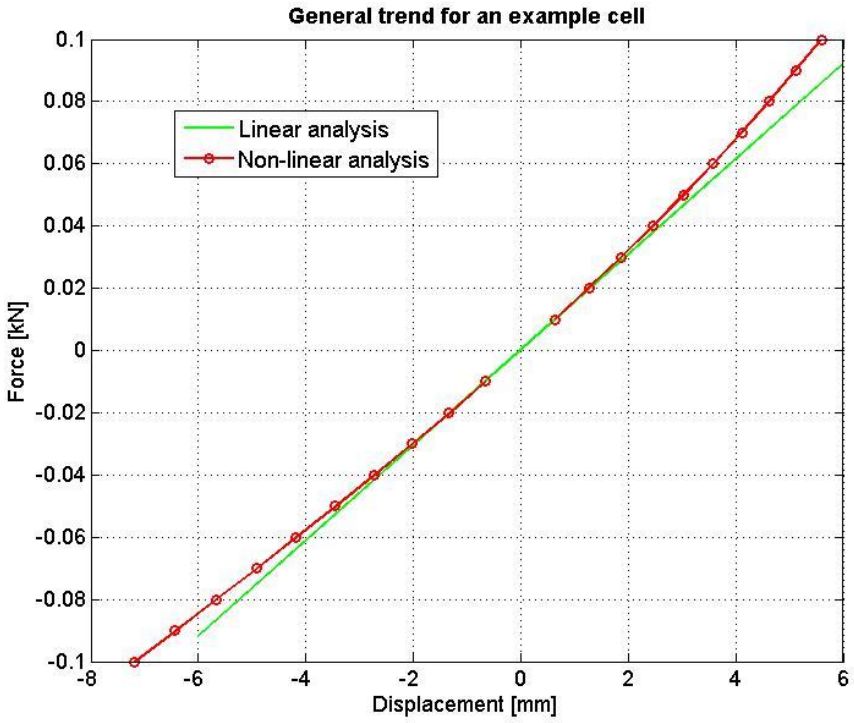

Figure 4.17 – Comparison between linear and nonlinear analysis

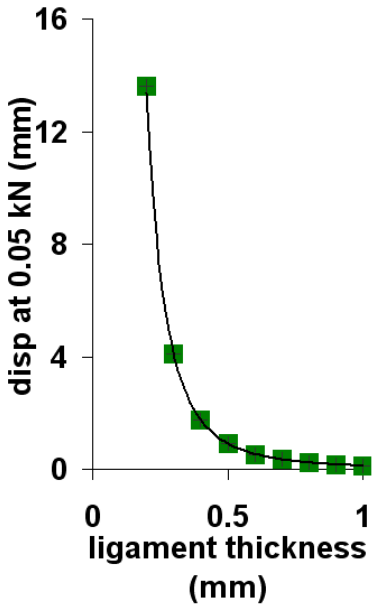

Figure 4.18 – Ligament thickness versus displacement at 50 N

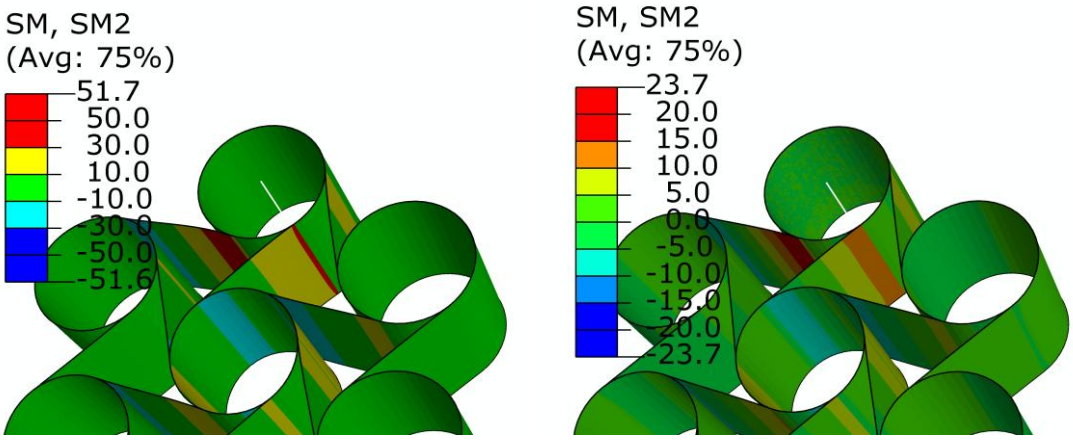

Figure 4.19 – Unwinding moments for the chiral units (a) CFRP $[\text{cross ply}]_7$ (b) GFRP $[\text{cross ply}]_{17}$

5 Numerical Activities on the Rib

The design process that will ultimately lead to the definition of the final configuration for the technological demonstrator of the morphing sail, several finite element analysis have been realized, each of them with their own peculiarities and specific purposes. Abaqus CAE was utilized for the finite element analysis and linear (implicit) method was employed. Each of these models has enabled to study the behavior of the rib with chiral topology, verifying the performance of the structure in terms of displacements, but at the same time providing important information on the distribution of the loading. In this chapter the results of the solutions obtained from the analysis and investigation of various models will be presented. The analyses have been conducted by using the numerical model of the optimized structure which provides the parameters to arrive at the final configuration of the airfoil profile. The model was revised by a post – processor software to accommodate the profile depth and correct minor aspects related to the skin. Several models have been analyzed based on their depth to study the deflection and stress levels of the structure to assess their candidacy as the primary structure of the morphing wing. The optimization of the rib has also been carried out to redistribute the load acting on the rib.

5.1 Finite Element Analysis of the Rib

In this section the modeling techniques used for the construction of the finite element model are illustrated. The Finite Element (FE) model was created by using Matlab software. The mesh on the surface was automatically generated and transferred to Abaqus for the analysis. FE model of the airfoil used in the analysis is shown in Figure 5.1.

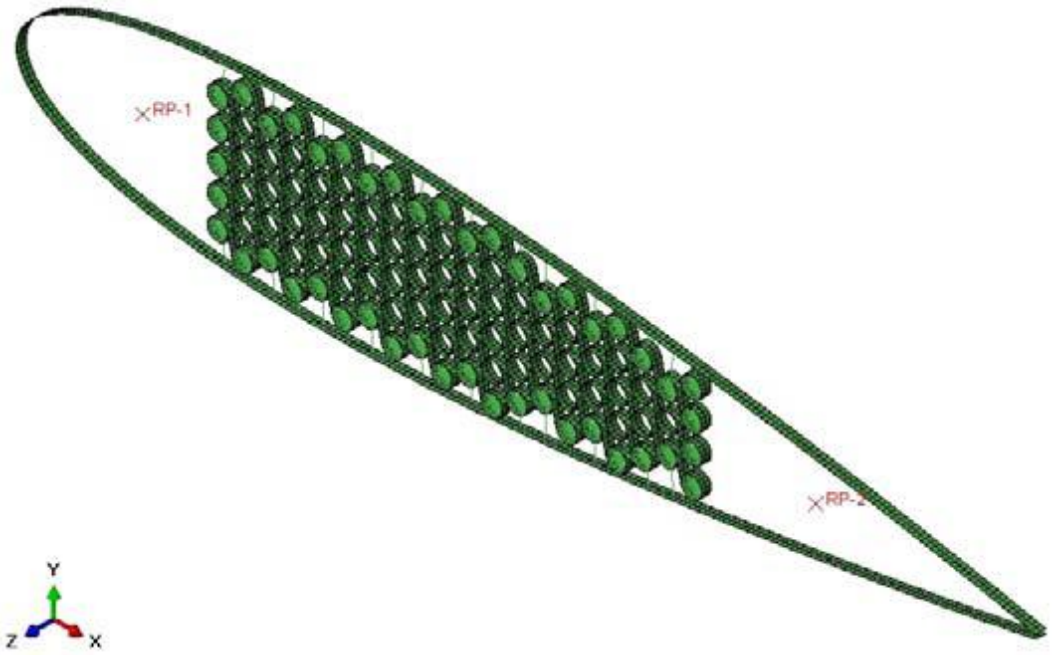

Figure 5.1 – FE model of the bi – dimensional airfoil

The generation of chiral network that forms the core of the profile is due to parametric code through MATLAB, which requires geometric parameters and technology as input data, selection of modeling and characteristic values of the materials used, summarized in Table 5.1 [35].
This method of generation of the mesh as shown schematically in Figure 5.2, has particularly been beneficial, both because it has allowed the construction model in a flexible and fast way, and owing to the fact that it worked very well in the subsequent optimization procedures. Nodes, ligaments and flexible skin have been modeled using four – node shell elements. The implementation of this type of elements in Abaqus provides that the formulation is adapted automatically according to the relationship between thicknesses and characteristical dimensions of the shell where the ratio of characteristic dimensions over thickness is practically 15:1. The external nodes through which the load is introduced into the structure have been equipped by beam elements that connect the center of the node to the other internal nodes and which very high elastic modulus is attributed with the aim of making them practically rigid.
The Leading/Trailing edges of the profile are made of rigid bodies, which belong to the two respective points of reference; these nodes were then fixed to the ground in such a manner that it was only possible to rotate around the Z axis (out – of – plane axis), giving the profile possibility of deflection.

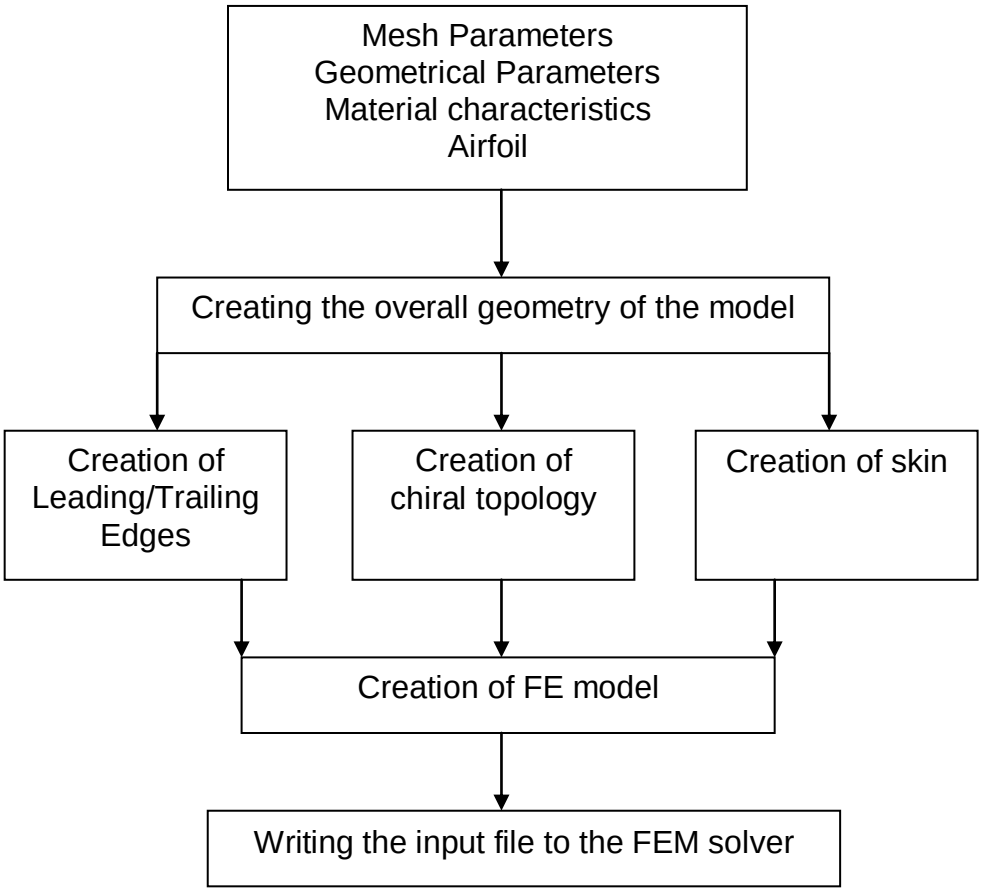

Figure 5.2 – Diagram for the generation of bi – dimensional model

Table 5.1 – Parameters for the generation of the chiral structure

Geometrical Parameters	
L	Length of the ligaments
r	Radius of the cylinder
c	Chord of the profile
x_1	Beginning of the chiral section
x_2	End of the chiral section
x_{g1}	Hinge of Leading Edge
x_{g2}	Hinge of Trailing Edge
Technological Parameters	
t_{carb}	Thickness of the carbon ply
n_{skin}	Number of plies of the skin
Modeling Parameters	
n_{elz}	Number of elements in the spanwise direction
n_{lig}	Number of elements departing from each node
Characteristics of Materials	
Material for the chiral structure	
Material for the skin	

The properties of the chiral structure have been specifically assigned; for nodes and ligaments, type and number of plies utilized and the adopted sequence of lamination. The utilized laminates are prepreg (pre – impregnated) with 0 – 90 ° woven carbon fiber composites. The mechanical properties of the carbon material which was used in the analysis are reported in Table 5.2.

Table 5.2 – Mechanical properties of the utilized carbon material

	Carbon Fiber Composites
E_1 (MPa)	56550
E_2 (MPa)	56550
E_3 (MPa)	10000
v_{12}	0.05
v_{23}	0.3
v_{13}	0.3
G_{12} (MPa)	4043
G_{23} (MPa)	4043
G_{13} (MPa)	4043
t (mm)	0.1

Regarding the modeling of the skin, it was chosen to define directly the equivalent stiffness matrix of the composite laminates specifying the elements. In preliminary design stage of the skin the requirements have been basically two: Minimize the axial rigidity and avoid wave like deformation mechanisms. To recall the stiffness matrix of a laminate, Classical Lamination Theory (CLT) could be rewritten as:

$$\begin{Bmatrix} N \\ M \end{Bmatrix} = \begin{bmatrix} A & B \\ B^T & D \end{bmatrix} \begin{Bmatrix} \varepsilon_0 \\ \kappa \end{Bmatrix} \qquad 5.1$$

Where ε_0 is the membranal deformation of the mid – plane of the lamina, κ is the curvature, N and M are force and moment, A, B and D are extensional stiffness, coupling stiffness and bending stiffness of the lamina respectively. The interface between the skin and the chiral structure was carried out by connecting the centers of beam elements B31, in which the outer nodes have the rotational degrees of freedom so that they operate as connecting rods, bearing axial loads only. The loads were generated by an interpolator code written in Matlab which requires flight conditions as input (velocity and angle of attack) and effective length of the component from where the loads are collected to be transmitted to the structure. In the Figure 5.3 deformed shape of the optimized bi – dimensional model is shown; maximum deflection is close to 22 mm in the vertical direction.

For the rib model, sensitivity analysis was conducted similar to the one that was performed for the chiral unit with the aim of verifying the stiffness of the structure follows the cubic power of the thickness of the ligament. In this case however, as can be observed in Figure 5.4, the curve fitting does not follow the third power of the thickness, but it is characterized by an exponent less than the cubic power. This indicates that the overall rigidity is not solely determined by the deformation mechanism due to bending of

the chiral units, but also influenced by the properties of the skin, although it is characterized by a limited membranal stiffness.

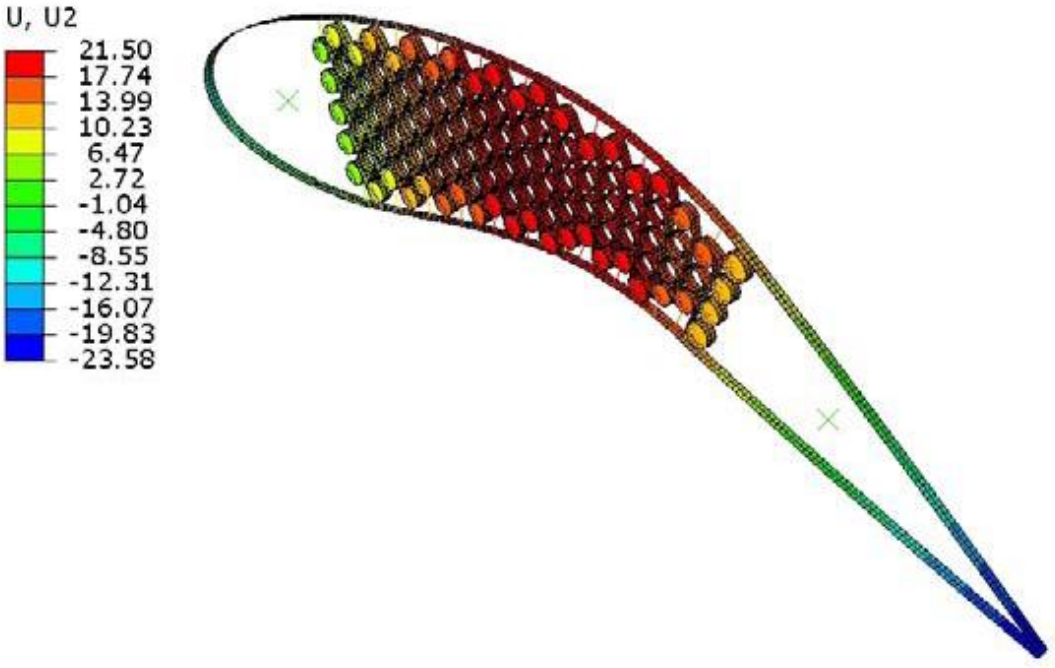

Figure 5.3 – Deformed shape of bi – dimensional model

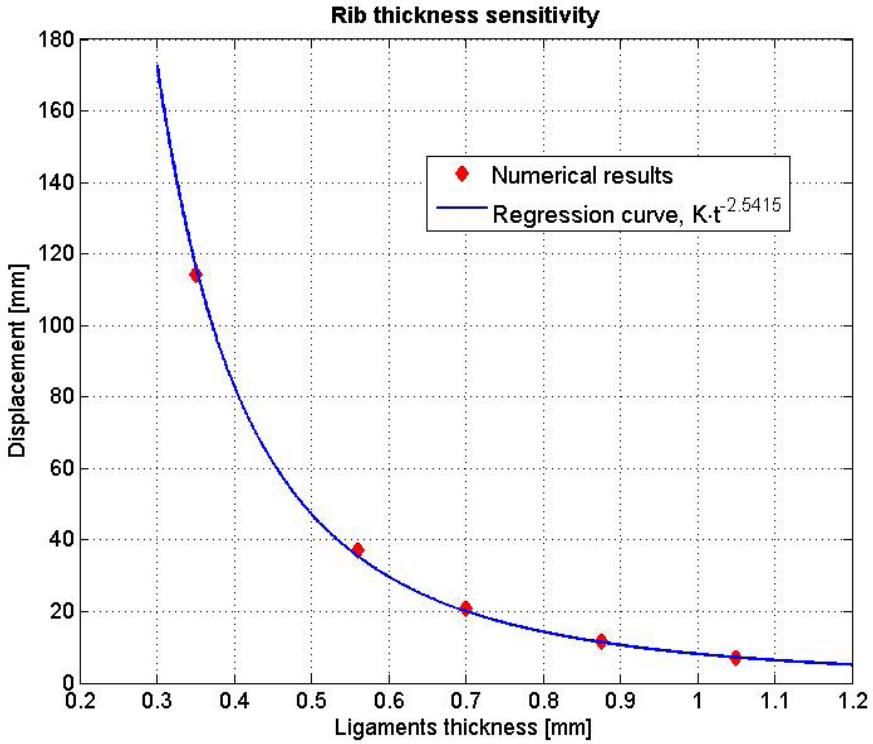

Figure 5.4 – Sensitivity of the rib with the varying thickness of the ligaments

The loads were applied in a concentrated way on all superficial nodes of the posterior and rim specifically for each direction. The extent and distribution of the load is supplied directly by an interpolator. The interpolator is a Matlab code that by accepting a series of values as input related both the geometry of the airfoil and flight conditions as reported in Table 5.3 directly provides the .inp files containing the nodal loads to be applied to the model.

Table 5.3 – Input parameters of the interpolator's aerodynamic loads

Flight Conditions		
V	Velocity of flight	41 m/s
α	Angle of attach	10º
Geometrical Parameters		
c	Chord of the wing	1000 mm
d_z	Spanwise length	1000 mm
x_1	Start of the chiral topology	20%
x_2	End of the chiral topology	66%
	Aerodynamic mesh	file.dat
	Structural mesh	file.mat
Aerodynamical Data		
	Distribution of C_p	file.dat

For the conditions under investigation resulting in the horizontal and vertical directions (with reference to the global axes of the model) are respectively:

Fx = 1346.4 N
Fy = -141.04 N

The code divides the profile into six sections numbered in counter – clockwise starting from the posterior part of the box of the trailing edge (Figure 5.5) and for the calculation of the forces a routine aeroelastic interface is used.

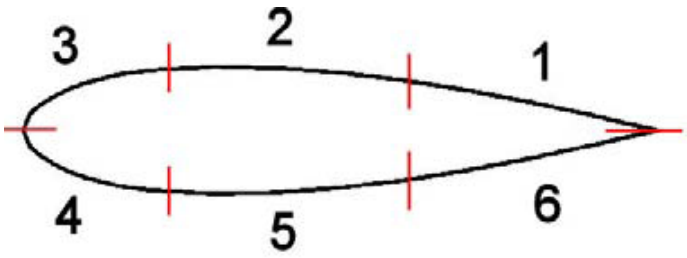

Figure 5.5 – Subdivision of the airfoil for the definition of the loads

Before the calculation is made of the loads on the bi-dimensional model with regard to the aerodynamical mesh, using data on the distribution of pressure coefficient in the file.dat, after which the code proceeds to create the interface between the aerodynamical and structural mesh (described in mat.file, which contains the positions of the nodes related to the finite element model produced in Abaqus). Such determined

nodal forces are then divided for number of nodes in the spanwise and applied on all points of the surface model.
It is possible to find the optimal design point by varying the thickness of ligaments and nodes until a satisfactory solution is obtained. In the Table 5.6 results for sensitivity analysis could be found where the main rib of the technological demonstrator has been studied. The sensitivity analysis was carried out based on the width of the strip and number of plies of the ligament and the node. As it can be seen from the table, three different ratios of number of plies on the ligament to number of ligaments on the node (n_l/n_n) were used. In the optimized solution, the vertical deflection is about 22 mm, so the best solution compared with the reference strip is 7 – plies ligament with a 50 mm wide strip. When reached to 7 – plies ligament with 50 mm wide strip, a sensitivity analysis was conducted by increasing the number of plies on the nodes of the strip. In that sense, 7 – plies ligament with 7 plies on the node is a convenient solution. This solution gives 19.9 mm deflection and 320 MPa of stress in the vertical direction. The Figure 5.6 (a) (b) show deflection levels for this strip, deflection on the Z direction is negligible and would not be given on the table as well. The figures indicate the locations for the configuration where the maximum and minimum deflections are.

Table 5.4 – Sensitivity analysis for different rib configurations

	5 plies **6 plies on node Strip is 30mm dz=500 mm**	**7 plies** **7 plies on node Strip is 30mm dz=500 mm**	**5 plies** **6 plies on node Strip is 50mm dz=500 mm**	**7 plies** **7 plies on node Strip is 50mm dz=500 mm**	**7 plies** **7 plies on node Strip is 15mm dz=250mm**	**7 plies** **7 plies on node Strip is 15 mm dz=500 mm**	**7 plies** **7 plies on node Strip is 30mm dz=500 mm**	**7 plies** **7 plies on node Strip is 50mm dz=500 mm**	**7 plies** **8 plies on node Strip is 50mm dz=500 mm**
U_1 max(mm)	22.5	11.2	13.6	6.8	10.4	19.6	11.2	6.8	6.59
U_1 min(mm)	-22.5	-10	-13.6	-6.0	-9.6	-17.5	-10	-6.0	-5.68
U_2 max(mm)	71	31.9	43.8	19.9	30	54.98	31.9	19.9	18.8
U_2 min(mm)	-80.9	-36.4	-49.3	-21.6	-34.3	-62.6	-36.4	-21.6	-20.3
Ratio of number of plies in the ligament to number of plies in the node(n_l/n_n)	0.83	1	0.83	1	1	1	1	1	0.875
S_{11}max(MPA)	81	76	49.5	44.8	67.7	50.6	76	44.8	35.9
S_{11}min(MPA)	-75	-68.9	-47.1	-42.1	-61.8	-41.6	-68.9	-42.1	-33
S_{22}max(MPA)	908	535.9	559	320	505.7	1030	535.9	320	311
S_{22}min(MPA)	-745	-438.4	-463	-263.7	-413.1	-845	-438.4	-263.7	-259

The Figure 5.7 shows the locations where the maximum and minimum S_{22} stresses (stresses in the Y direction) are located for the same configuration. The S_{11} and S_{12} stresses are negligible since they have relatively small stresses.

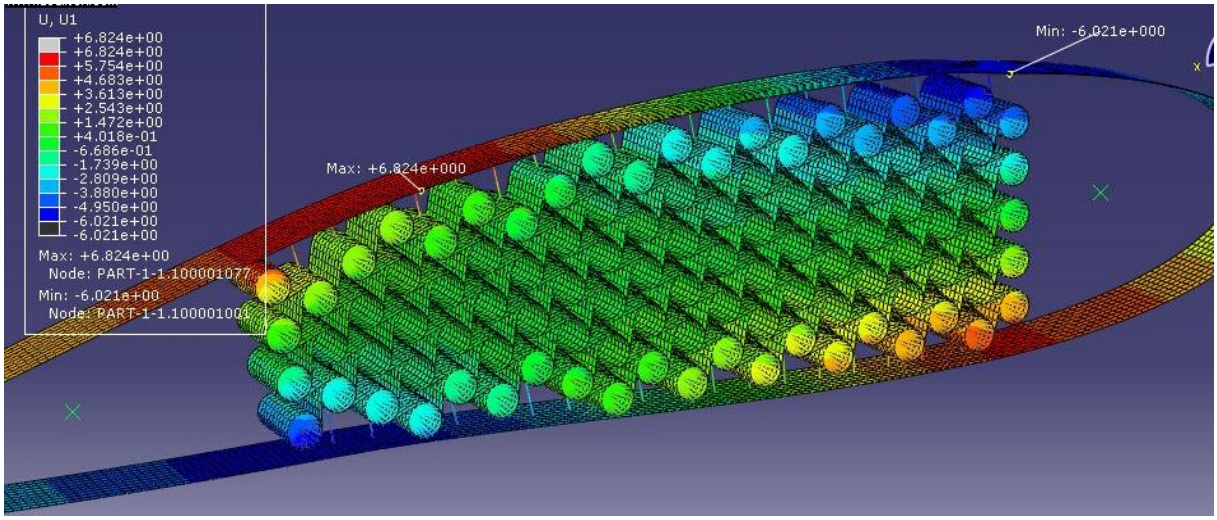

Figure 5.6 (a) – U1 deflection for 7 – plies ligament with 7 plies on node (strip is 50mm)

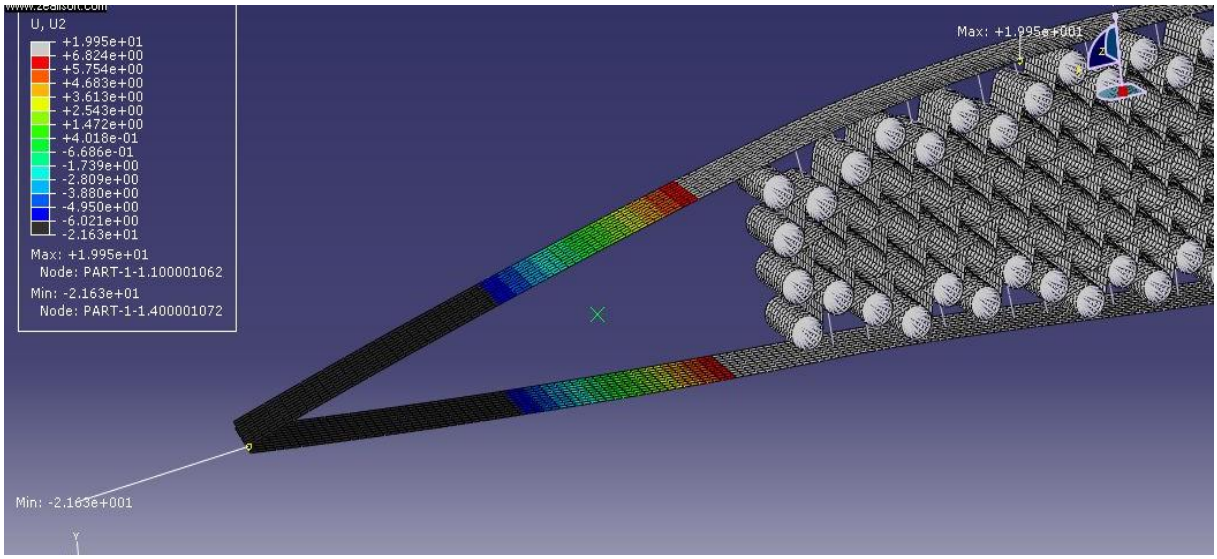

Figure 5.6 (b) – U2 deflection for 7 – plies ligament with 7 plies on node (strip is 50mm)

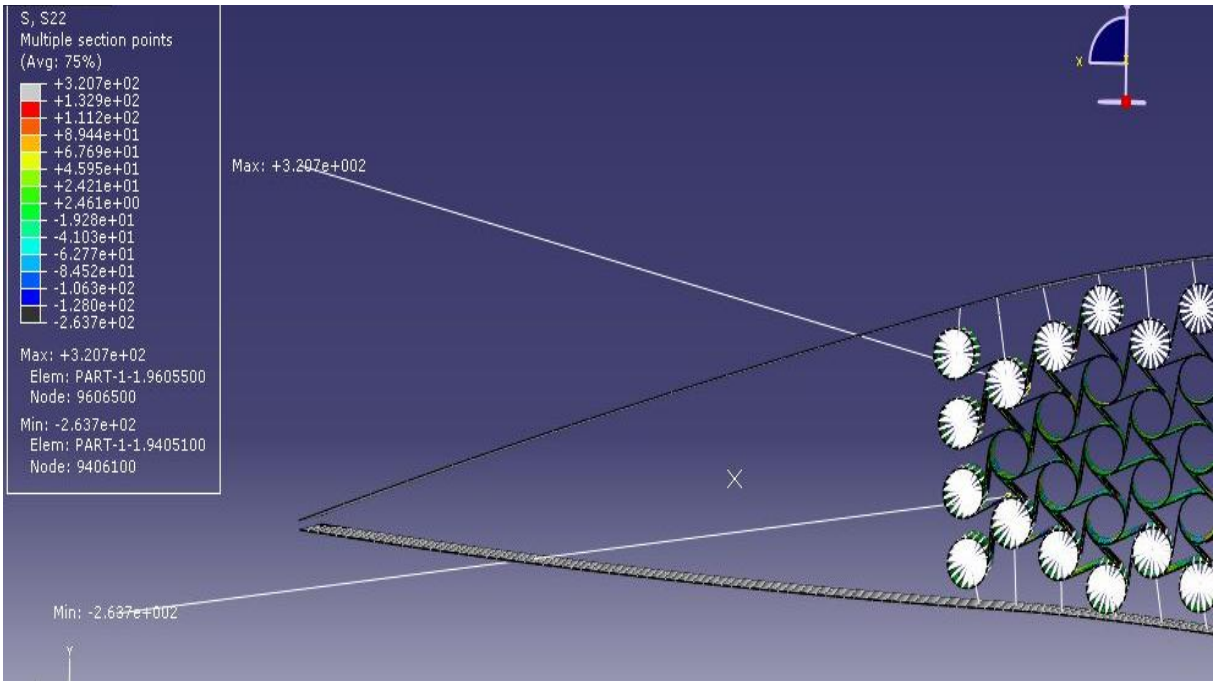

Figure 5.7 – S_{22} stresses for 7 plies ligament with 7 plies on node (strip is 50mm)

5.2 Optimization of the Rib

The analyzes carried out on the model of the demonstrator showed that most of the stress is concentrated in the ligaments of the external nodes of the rib, while the internal part of the structure remains relatively low. As a next step, the possibility of optimizing the thickness of the ligaments would be explored so that the maximum moment flux is reduced and the load is distributed in a more homogenous way. Nevertheless it is also appropriate to consider the issue of the weight of the structure and investigate possible changes in the distribution of the thickness to minimize it.
The initial configuration was a 50 mm wide rib with half of the total load acting on the complete demonstrator to replicate the situation in which the skin collects the load in the influence zone of the rib, to reach the value of deflection close to that of the reference strip; ligament thickness of 0.7 mm was used.
It was then applied a correction factor of the effect of the thickness of the skin K_t, about 0.85 for the three ribs demonstrator configuration; this adopted general approach have been reported by obtained solution of the optimized studies on the reference rib of the actual configuration determining the thicknesses using the appropriate correction factor.
The first operation was the subdivision of the rib in appropriate areas, creating set of elements that contain the ligaments involved in each chosen area. As a preliminary approach three main areas were chosen to identify [36]:

- Exterior ligaments (also including posterior and anterior)
- Intermediate
- Interior

The three main areas are shown in Figure 5.8. In the figure, exterior ligaments are represented by black color while intermediate ligaments are represented by red and interior ligaments are represented by blue color. This selection was the result of a compromise between structural considerations over concentrations of stress/moment and the necessity to limit the number of project variables in the optimization. Even it were possible to define parameters of local thickness numerically (ligament by ligament for example), the solution would further complicate the realization of the rib from the technological point of view.

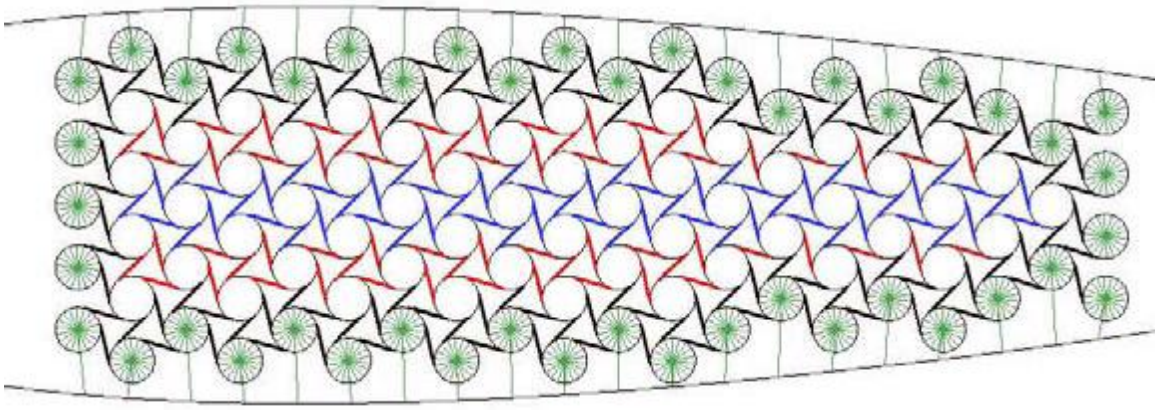

Figure 5.8 – Three main sections of the rib

The design variables chosen for optimization are therefore the total thickness of the ligaments within the three zones. A variation range between 0.1 mm and 1.5 mm was defined, with a default value equal to 0.7 mm, the thickness in correspondence of the nodes was considered dependent on the thickness of the ligaments through a proportionality factor K, maintained as a fixed value in some analysis and considered as the design variable in others. Regarding the technology used for the production of the chiral topology, the factor K depends on how the ligaments are tapered; it is equal to 2 for non – tapered ligaments obtaining nodes twice as the thickness of the ligaments. A summary of the parameters of the model defined for the optimization is reported in Table 5.5.

Table 5.5 – Parameters of the model

	Minimum	**Maximum**
Thickness of the exterior ligaments, t_A	0.1 mm	1.5 mm
Thickness of the intermediate ligaments, t_B	0.1 mm	1.5 mm
Thickness of the interior ligaments, t_C	0.1 mm	1.5 mm
Proportionality factor	0.7	1.5

Regarding the selected quantities to be evaluated as the output, state of stress and deformation of the structure were defined. The first objective considered for the optimization procedure has been consistent in determining a configuration of the rib to reduce the flow of bending moment on the ligaments as much as possible and allowing the load to be transmitted effectively to the whole structure, thus uniforming the stresses inside the rib. To minimize the bending moment, the operation to be performed was to reduce the thickness of the ligaments in the outer zone, this leads an increase of the overall deflection. The optimizations have been performed for different values of the proportionality factor K in order to investigate the effects of the drop – off performance of the rib; despite the stiffness of the structure is mainly linked to the deflection mechanism of the ligaments, during the studies on chiral cells, nodes demonstrated to assume a certain importance. The results show a substantial reduction of the maximum bending moment on the ligaments. It should be noted that the reduction is the price of a significant increase in structural weight due to mainly the adoption of a higher proportionality factor K, and then a substantial increase of the contribution of the total mass of the nodes.

Subsequently in the performed optimizations with the aim of minimizing the stresses on the structure, investigations have also been conducted on the total weight of the rib and on the possibility to reduce it by dealing with the distribution of thickness of the ligaments. The deflection is an important factor in the optimization process and deflection level has been inserted as the upper limit but also in this case the tendency of deflection is in contrast with that of the weight. The analyzes have also been intended to verify the best technique to deal with the reducing the weight and thickness in a harmony.

The obtained solutions, shown in Table 5.6, meet all the requirements of deflection, stress and bending moment, by doing these values have been reduced by more than 10% compared to the original configuration. Although the weight was reduced compared to the configuration in which only the moment was minimized, has never been less than the original configuration. This indicates that it is impossible to obtain a significant reduction of the load on the ligaments while making the structure more lightweight. The reason for this, resides in the fact that in order to reduce the moment it is necessary to use thinner ligaments in the exterior zone, but this must correspond to a proportionally much larger increase of the thicknesses of the interior part to restore the adjusted overall stiffness and comply with the deflection requirement. As can be observed in the Table 5.6, having obtained values of decimal thickness with a precision of hundredths of a millimeter, clearly not manageable by the technological process, it would be necessary to resort to appropriate methods to obtain the same stiffness characteristics using an integer number of composite plies.

In that sense a more feasible configuration to produce the optimized rib could be proposed; In the Table 5.7, the final configuration which is convenient for the technological process is given.

Table 5.6 – Compromised configuration for the rib

	Gradient	**Simplex**
Thickness of the exterior ligaments, t_A	0.66 mm	0.6 mm
Thickness of the intermediate ligaments, t_B	0.6 mm	0.98 mm
Thickness of the interior ligaments, t_C	1.02 mm	0.79 mm
Proportionality factor, K	1.02	1.11
Deflection, U_y	21.5 mm	21.16 mm
Shear stress, τ	324.1 MPa	376.7 MPa
Flux of moment, M	23 N	22.67 N
Weight	0.6227 kg	0.6735

Table 5.7 – Final configuration of the optimized rib

	Exterior ligaments	**Intermediate ligaments**	**Interior ligaments**
Number of plies in the straight section	5	8	7
Number of plies in the node	6 (2 drop – offs)	10 (3 drop – offs)	8 (3 drop – offs)

6 Technological and Experimental Activities of the Rib

Rib is the internal structural frame that deforms under the action of the aerodynamic pressure. The rib should also provide sufficient flexural and torsional stiffness. The production technology of the rib is based on the exploitation of the manufacturing success of the chiral unit with some modifications. This PhD research is mostly concentrated on the design of the technological demonstrator and design/production of the chiral unit and the rib. This chapter is organized in four main sections: the first section presents the design and the manufacturing technology of the rib. The second section concentrates on the static testing of the rib, in which three types of the loading were carried out to perform the tests namely concentrated loading on the middle and the last nodes and distributed loading, the third section describes correlation between the experimental findings and the numerical calculations. The last section defines preliminary design for the Leading Edge (LE) and Trailing Edge (TE), corrugated flexible skin which provides torsional strength to the wing and connections between rib and skin. The connections which link skin to the ribs are pin – hinge mechanisms that can rotate freely around the out – of plane direction.

6.1 Design and Production of the Rib

Four chiral unit cells have been produced and tested to see the compliancy and the manufacturability of the unit structure. It was seen that the success that was already achieved for the chiral units could also be exploited for a rib which is composed of chiral cells inside. Before proceeding the production for the rib structure, some modifications were realized to facilitate the assembly of the ligaments in the mold of the rib; both the material and production method of the cylinders were changed. The assembly molds of the chiral units utilized metallic cylinders to house the ligaments but this brought problems during the extraction of the chiral unit after the autoclave process. The excessive resin on the chiral unit surface stack on the slots of the metallic cylinders, making the chiral units vulnerable to failure during the removal of these units from the assembly mold. In order to solve this problem, a self – lubricating material like Polytetrafluoroethylene (PTFE) – Teflon as it is best known – was replaced with the metallic cylinders. The opening method for the groove of the slots of the cylinders was also modified; instead of electroerosion process for the metallic cylinders, mechanical cutting was employed for the Teflon cylinders. Some pilot productions were also carried out for chiral units using Teflon – made cylinders and it was testified that Teflon provided both comfort in the assembly of the ligaments into the slots of the cylinders and ease of extraction during the removal process of the chiral unit from the assembly mold after the autoclave. In the Figure 6.1 (a) and (b) metallic cylinders and Teflon cylinders could be seen for the assembly mold of the chiral units. The same Teflon – made cylinders were employed for the assembly mold of the rib. The Figure 6.2 shows the Teflon – made cylinders on the assembly mold of the rib.

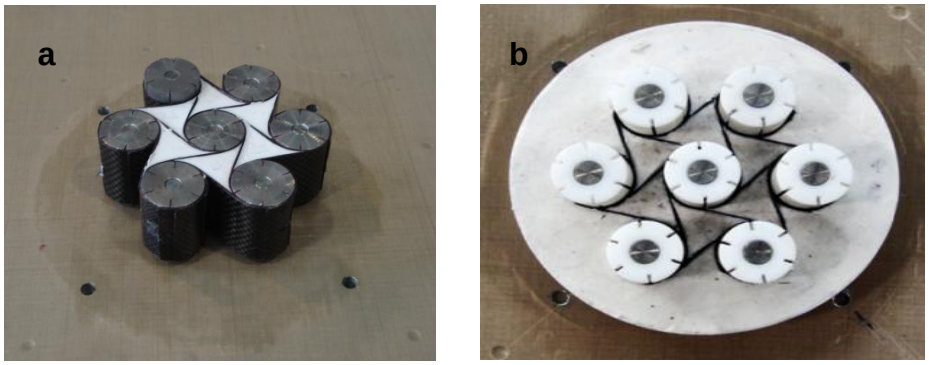

Figure 6.1 – Cylinders for the assembly mold of the chiral units (a) Metallic (b) PTFE (Teflon)

The numerical results showed that 7 plies solution for the chiral rib is the best configuration. The optimization was carried out to redistribute the load without reducing the strength of the rib to failure. The load redistribution yielded a similar deflection based on the varying rib thickness but moment gradient was reduced by one – third. In order to redistribute the load through the rib chiral network, producing the ligaments in different ply laminations instead of having only seven plies solution had to be realized; obtaining different ply thicknesses through the rib where there exist three different ply

laminations: five plies at the outer section, eight plies at the middle section (between five and seven ply laminations) and seven plies at the inner section (core section of the rib). Having thought that it is a complex task to implement this configuration in the technological field, simplification of the technological process has been carried out; two ply thicknesses instead of three would be implemented i.e. five plies at the outer section and eight plies at the inner section of the rib. Before proceeding with the manufacturing of the full rib, pilot manufacturing was realized to see if this methodology is easy to implement and the structure is compliant enough. A portion of rib was produced with two different ply thicknesses. It was seen that the obtained structure is too rigid with regard to the numerical results, with this unexpected experience it was decided to make the structure more compliant i.e. implementing same ply lamination thickness through the whole rib. The Figure 6.3 indicates a portion of the rib with two ply thicknesses; five ply ligaments on the outer section while eight ply ligaments on the inner core. The five ply ligaments were marked with paint to distinguish between two types of ligaments in two different thicknesses. As it can be seen from the figure, five ply were assembled on the outer section of the rib. The ligaments that link the inner nodes with other inner nodes were connected by eight ply ligaments but an inner node which has a connection with an outer node is linked to the outer nodes by five ply ligaments.
It was seen that the obtained structure was too rigid with regard to the numerical results, with this unexpected experience it was decided to make the structure more compliant i.e. implementing same ply thickness through the whole rib. Second pilot manufacturing was made with the all 5 – plies configuration concentrating on the production of a small portion of the rib. After the rib was obtained, it was observed that 5 – plies solution is feasible to proceed with the manufacturing of the whole rib because of the rigidity is compliant enough and production in one shot is relatively easy to handle. Figure 6.4 shows 5 – plies laminated rib portion after it was removed from the autoclave. Based on the experience during the assembly of the rib portion with two different ply thicknesses, some modifications have been done for the convenience of the assembly process of the all 5 – plies rib portion.

Figure 6.2 – Teflon – made cylinders on the assembly mold

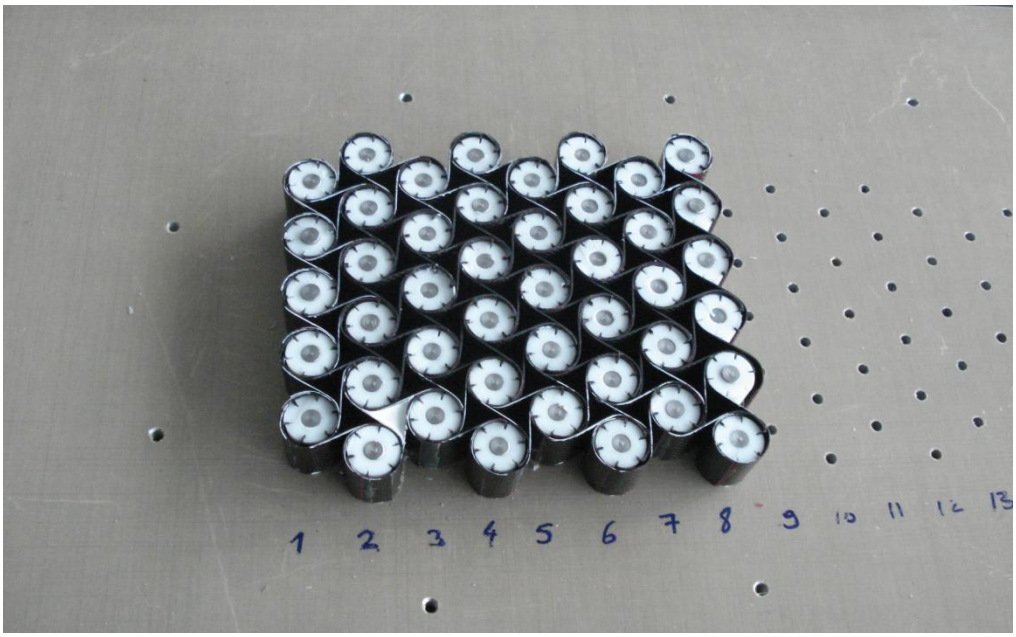

Figure 6.3 – A portion of the rib with two ply thicknesses

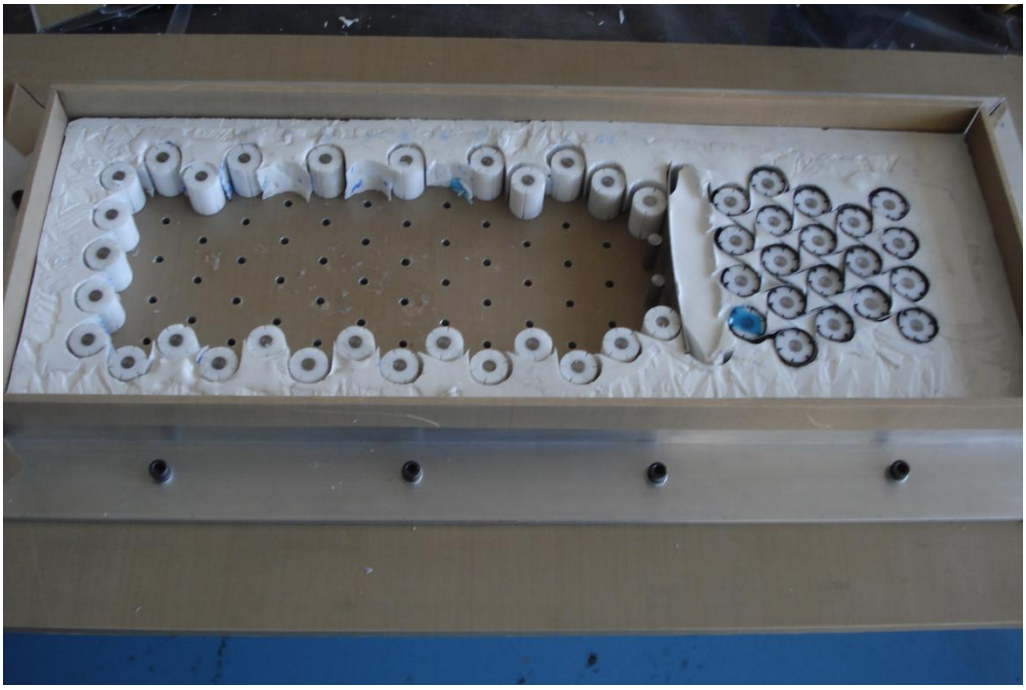

Figure 6.4 – A portion of the rib with all 5 – plies solution

For placing the silicon rubber inserts; in the first practice, the triangular shaped silicon rubber pieces were planned to be inserted after the assembly of the ligaments has been completed. This implementation brought inconveniences because most of the silicon rubber inserts cannot be put to the dedicated gaps after the ligaments were assembled

to their dedicated spots. The reason why these triangular shaped silicon rubber inserts cannot be located to their dedicated spots was the triangular shaped area became even smaller after the assembly of the ligaments. In the Figure 6.5 a small section of the rib with this silicon rubber insert technique could be seen. It can be clearly seen that no silicon rubber piece is inserted in this phase of the assembly.
In case of such an application, silicon rubber was injected in its liquid form to the triangular gaps by using a syringe. The Figure 6.6 shows the application of silicon rubber into the triangular shaped dedicated spots of the rib by using a big syringe. This methodology has been considered as not the best implementation for the silicon rubber inserts because after the autoclave process it was hard to extract these pieces of silicon rubbers without any problem. In order to overcome this problem a new methodology has been implemented. The triangular shaped silicon rubber parts as seen in the Figure 6.7 (a) were inserted during the assembly of the ligaments. This process was achieved when two ligaments are assembled on the PTFE cylinders but the gap of third ligament of the same triangle is idle. Figure 6.7 (b) shows the detail of the process.

Figure 6.5 – Implementation of silicon rubber inserts; Silicon rubber inserts not injected yet

Figure 6.6 – The application of silicon rubber by a syringe

Figure 6.7 – (a) Triangular shaped rubber inserts inside the silicon dam (b) Assembly of rubber inserts on the rib mold

The production of the whole rib with all 5 – ply ligaments has been initiated after seen that this procedure is convenient and production of the rib could be achieved in one shot. Figure 6.8 shows the picture of the whole rib with 5 – ply ligaments before the assembly mold goes into the autoclave. After the removal of the rib from the assembly mold, the complete rib was seen as more complaint than the previous rib configuration with two different ply thicknesses. It has also been proven that employing PTFE cylinders instead of metallic ones has assisted for the robust and quick removal of the rib from the assembly mold.

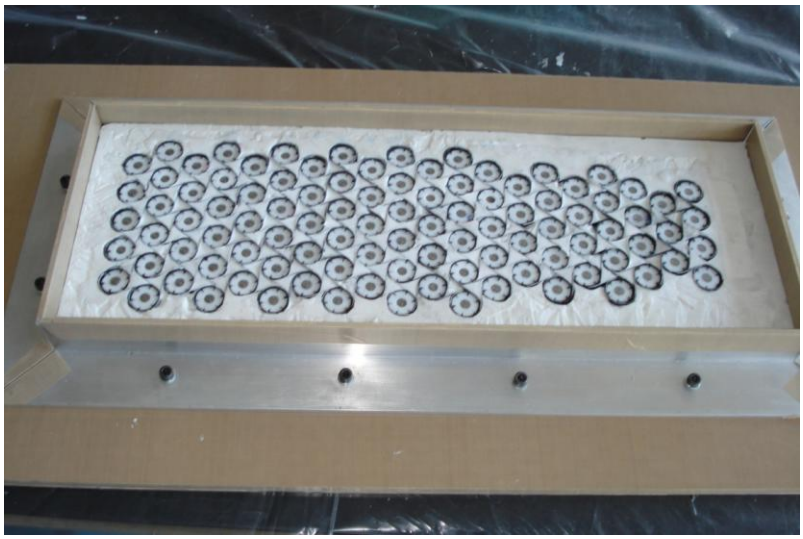

Figure 6.8 – Complete chiral rib with all 5 – ply ligaments

During the manufacturing of the two rib portions and the whole rib, several numbers of ligaments in different ply thicknesses were manufactured. The ligaments were positioned in the assembly mold in three different geometrical configurations; each

ligament follows another ligament in the superpositioned form with a 60º to form a node. As there are six ligaments to form a node, each ligament would be located in one of the three geometrical positions. The Following Table (Table 6.1) summarizes the configuration of the ligaments produced for the ribs and also the geometrical positions of the ligaments in the rib.

Table 6.1 – Configuration of the produced ligaments for the ribs

	Rib No: 1 (5 and 8 ply ligaments)	**Rib No: 2 (All 5 ply ligaments)**	**Rib No: 3 (All 5 ply ligaments, whole rib)**
Number of ligaments in the first position \	36	15	80
Number of ligaments in the second position /	35	14	86
Number of ligaments in the second position |	35	14	86
Number of curved sections of the ligaments (half – like ligaments)	54 (54/2=27 full ligaments)	34 (34/2=17 full ligaments)	96 (96/2=48 full ligaments)
Total number of ligaments	133	60	300

6.2 Testing of the Rib

The static loading experiments have been carried out on the rib by suspending loads to several locations through the nodes. The rib was fixed to the test fixture as it can be seen in the Figure 6.9. The text fixture should be able to sustain the attached loads without creating any relative movement, moment or damage on the fixture body itself and house convenient space for lasers and comparators. The lasers and comparators would be used to measure the deflection by specifying a reference point for each of the devices. The fixture apparatus was designed as a rigid body so that the constrained rib can bend along the direction of the movement of the load without creating a deflection on the fixture body. The measuring devices are attached to the test apparatus either in direct contact with the rib (comparator) or screwed to the supports and then fixed to the fixture (laser). Two different types of deflection measurement techniques are utilized i.e.

contactless measurement method by using laser probes and surface – contact measurement method by using comparators. The comparators are put to the top of the rib and thin shims are glued to three nodes of the rib to create a flat surface for the correct operation of the pins of the comparators. In order to prevent any gap between the pins of the comparators and the thin shims and therefore causing an error in the measurement, a small amount of pre – contact is provided. For the correct operation of the laser probes thin shims are also placed under the nodes of the rib. The surfaces of the shims are painted by black color in order to guarantee the reflection of the laser light so that the laser probe could work properly. The laser probes are set to '0' deflection at the beginning of each test by using the software, this means they are able to measure the deflection in a direct mode. The comparators are set to a specific value (by pre – contact); displacements are measured on the comparators by finding the difference between the last and the first reading on the scale.

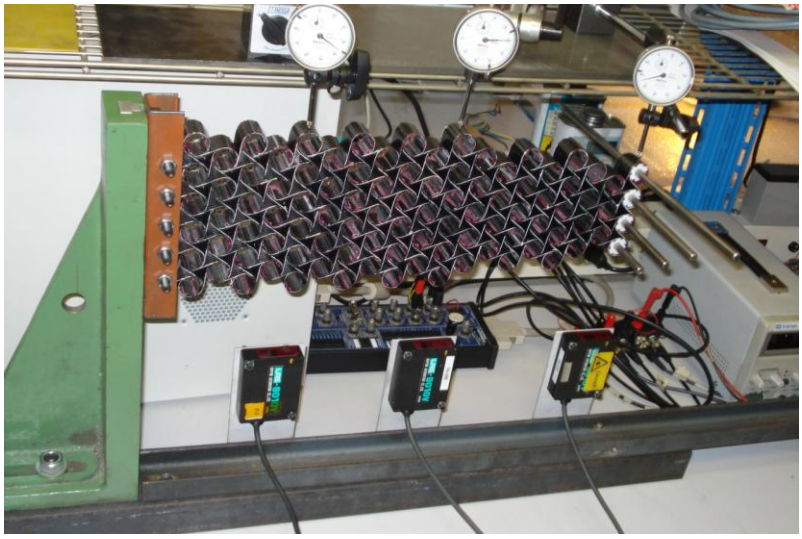

Figure 6.9 – Rib fixed to the test bench

Three types of tests have been planned to assess deflections at different loading conditions. The realized loading conditions on the rib were; loading on the last nodes (Test type 1), distributed loading: (loads distributed on several nodes, Test type 2) and the loads on the middle node (Test type 3). The tables (Tables 6.2, 6.3 and 6.5) show the loading conditions used during the tests.

Table 6.2 – Loading conditions for the test type 1

Loading on the last nodes	**0.5 kg**	**1 kg**	**1.5 kg**	**2 kg**	**2.5 kg**	**3 kg**	**3.5 kg**	**Total Load (kg)**
Test 1	X	X		X	X			2.5
Test 2	X	X	X	X				2
Test 3	X	X	X		X			2.5
Test 4	X	X	X	X	X	X	X	3.5
Test 5	X	X	X	X	X	X		3

Experimental setup was realized for test type 1 in such a way; Teflon – made cylinders were inserted to four nodes of the last column node of the rib and steel bars were placed to each of the Teflon cylinders to carry the iron weights by suspending these iron weights to the steel bars. First half kg weight was put to one side of the bar and then second half kg weight was put to the other side of the bar. As there is another bar on the same column one half kg weight was put to one side of the bar and other half kg weight to the other side of the bar and this way of loading went on to the last weight till the end of the test. The Figure 6.10 shows the suspended loads on the last nodes (concentrated loads) of the rib. Based on the loading levels, graphs were prepared for loads versus deflection values for each testing. Five testing were accomplished for test type 1 and it was seen that the results from test number one to test number five were consistent. In the Figure 6.11, loading versus deflection is given for test number 5 for this type of testing. In this testing, up to 3 kg of loading was tried to obtain the deflection.

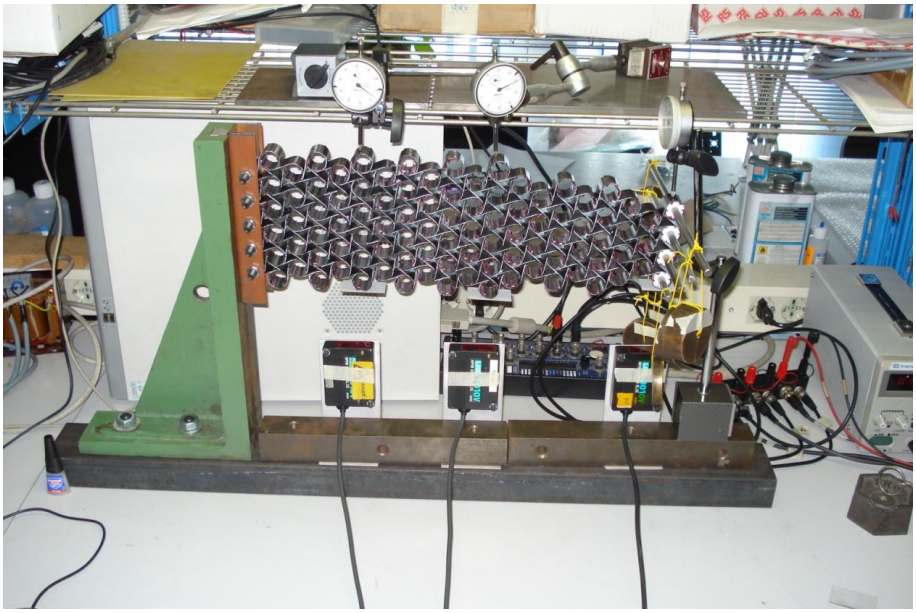

Figure 6.10 – Loads sustained on the last column of the nodes

The loading sequence for the Test type 2 was carried out in this way; Teflon – made cylinders were inserted to several bottom nodes of the rib namely 6th node, 12th node and 20th node(node number 1 is the first node on the constrained edge). The loading sequence in the distributed load testing is somehow different than the concentrated loading testing of test types 1 and 3. Beginning from the middle node (12th node) the weights were distributed to the 6th and 20th node and so on until the last weight suspends on the steel bar. Total loading went up to 5 kg for this testing. The Figure 6.12 shows the suspended loads on the bars attached to three nodes (distributed loads). In the Figure 6.13, values for loading versus deflection could be seen for this testing. Table 6.4 gives measured deflection values for the distributed load testing. It can be noted that for step number 11, comparator 3 (node 20), deflection was measured as ‘0’ because the needle of the comparator was removed for this step and then put again for the next

measurement. The same phenomenon could be observed in the Figure 6.13 where load versus deflection graph has been obtained.

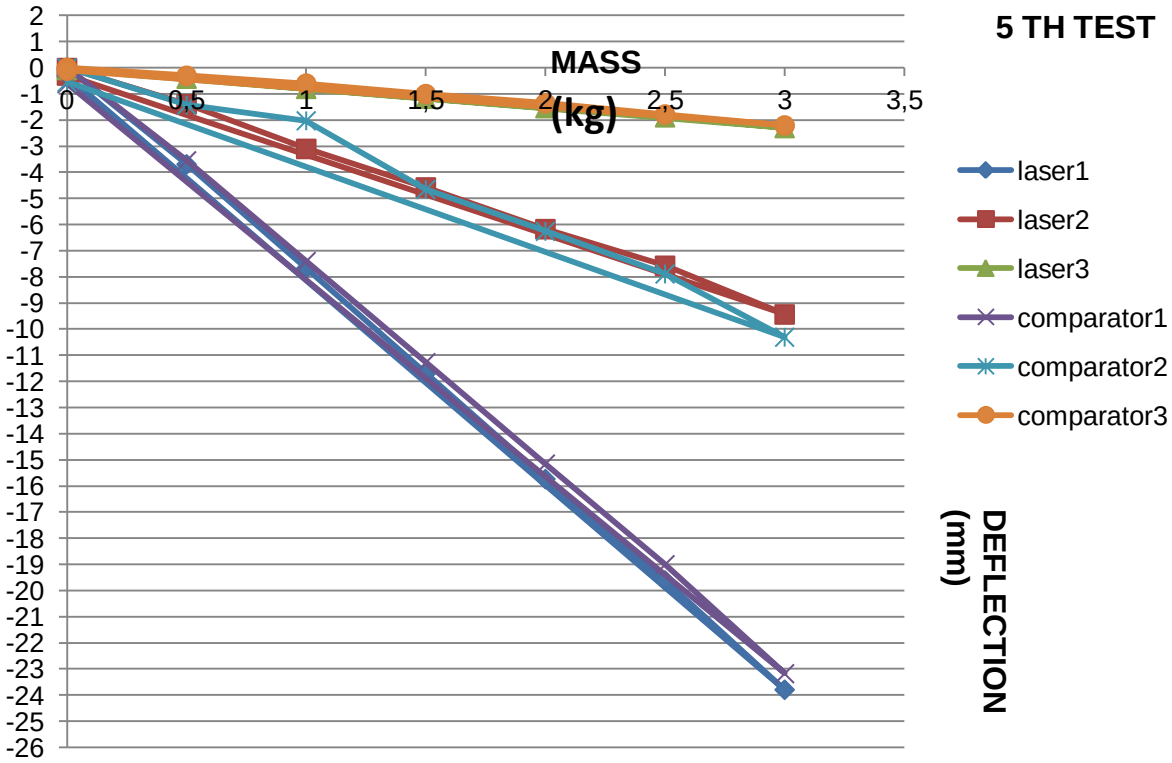

Figure 6.11 – Load versus deflection for test number 5, test type 1

For the Test type 3, the loading sequence was carried out in the following way; As the Teflon – made cylinders were in their dedicated nodes, weights were put to the middle node by adding half kg weights after each time reading the displacement values from the measuring devices. The loading is concentrated on the middle node and this type of loading sequence is the same when the loads were put to the last nodes as it was the case in the first type of testing. In the Figure 6.14 rib is shown while the loads are suspended on the middle node. Loading was concluded when the load reached 3.5 kg. In the Figure 6.15, values for loading versus deflection could be observed for test type 3. Like test type 1, test type 3 was also carried out by using concentrated loading.
To read the output values of the laser probes, an electronic interface was needed. This interface was connected to the PC and dedicated software was running to interpret the data that were collected through these probes. An important point is to control of the vibration on the rib for the proper data collection of the laser probes. If the vibration is too high i.e. as it was the case for the data collection of the probe on the last node of the rib, then the measured value was not correct. The best way to correct the error is to wait for some time and set the '0' value afterwards. The vibration or an external force on the table of the test apparatus were also a problem in the correct reading of the comparators. These devices are precise measurement apparatus and thus are susceptible to any external interference. In order to avoid these problems, the tests

should be carried out when there is nobody working in the close range or no electromechanical devices are working around.

Table 6.3 – Loading conditions for the test type 2

Step	**Node 06 R=Right side of the bar L=Left side of the bar**	**Node 12 R=Right side of the bar L=Left side of the bar**	**Node 20**	**Total load**
	(kg)	(kg)	(kg)	(kg)
1	0	0.5R	0	0.5
2	0	0.5R – 0.5L	0	1
3	0.5R	0.5R – 0.5L	0	1.5
4	0.5R – 0.5L	0.5R – 0.5L	0	2
5	0.5R – 0.5L	0.5R – 0.5L	0.5	2.5
6	0.5R – 0.5L	1R – 0.5L	0.5	3
7	0.5R – 0.5L	1R – 1L	0.5	3.5
8	1R – 0.5L	1R – 1L	0.5	4
9	1R – 1L	1R – 1L	0.5	4.5
10	1R – 1L	1R – 1L	1	5
11	0.5R – 0.5L	1.5R – 1.5L	1	5
12	0	1.5R – 1.5L	2	5
13	0	2R – 2L	1	5
14	0	2R – 2L	0	4
15	0	0	0	0

Table 6.4 – Measured deflections for the test type 2

Step	Deflections on Laser 1 Node 06 (mm)	Deflections on Laser 2 Node 12 (mm)	Deflections on Laser 3 Node 20 (mm)	Deflections on Comparator 1 Node 06 (mm)	Deflections on Comparator 2 Node 12 (mm)	Deflections on Comparator 3 Node 20 (mm)
	-0,181311	-0,757672	-1,290521	-0,22	-0,8	-1,55
1	-0,312592	-1,632947	-3,240216	-0,46	-1,59	-3,15
2	-0,352936	-1,877905	-3,371051	-0,52	-1,79	-3,49
3	-0,503906	-2,185492	-4,08819	-0,68	-2,09	-3,99
4	-0,781201	-3,69007	-8,023773	-1,06	-3,65	-7,78
5	-1,223505	-4,687878	-10,169104	-1,25	-4,42	-9,38
6	-1,530005	-5,578296	-11,501117	-1,51	-5,25	-10,98
7	-1,653992	-5,842743	-12,114282	-1,6	-5,47	-12,4
8	-1,625745	-6,056592	-12,261078	-1,73	-5,75	-12,82
9	-2,077264	-7,531165	-16,177863	-2,1	-7,22	-16,3
10	-2,279218	-8,679626	-18,42406	-2,32	-8,26	-17,66
11	-2,866864	-11,470978	-25,379108	-2,75	-10,68	0
12	-2,755664	-10,383582	-21,468726	-2,72	-9,81	-20,82
13	-2,085376	-7,568683	-14,527673	-2,25	-7,32	-14,25
14	-0,118433	-0,595746	-1,079944	-0,32	-0,78	-1,44
15	-0,181311	-0,757672	-1,290521	-0,22	-0,8	-1,55

Table 6.5 – Loading conditions for the test type 3

Loads on the middle node	0.5 kg	1 kg	1.5 kg	2 kg	2.5 kg	3 kg	3.5 kg	Total load (kg)
Test 1	X	X	X	X	X	X	X	3.5

Figure 6.12 – Loads sustained on three nodes for testing

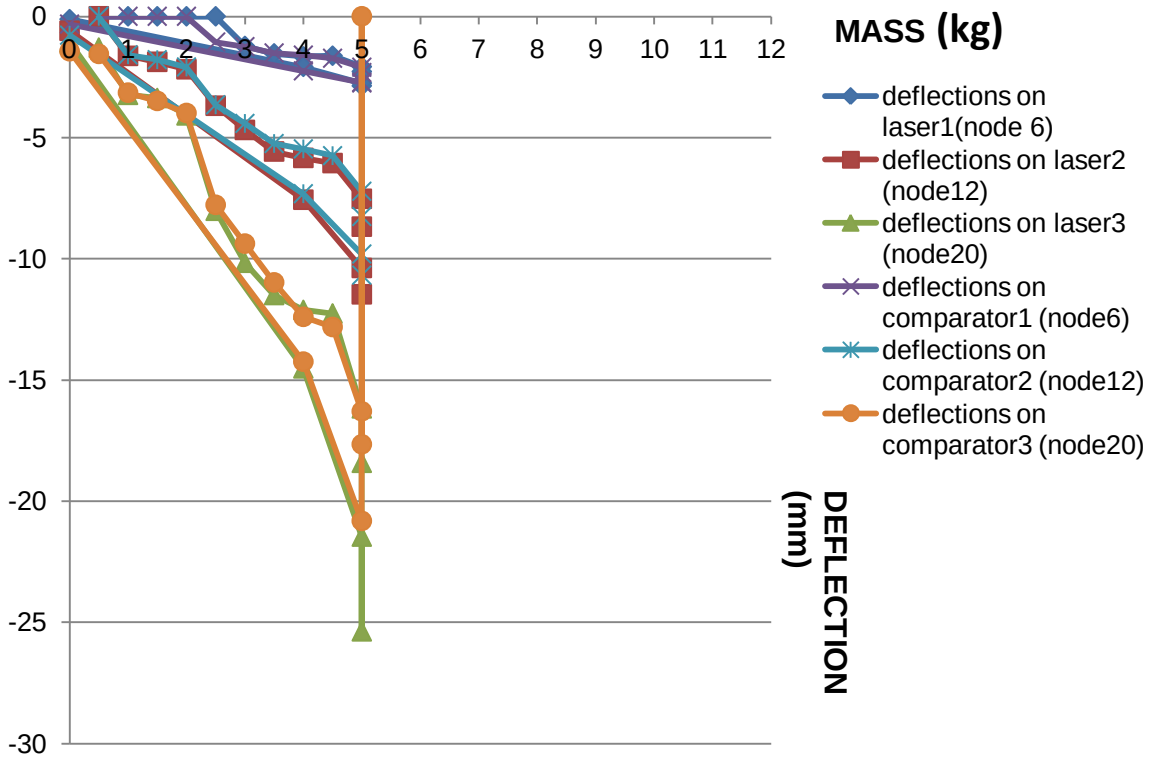

Figure 6.13 – Load versus deflection for test type 2

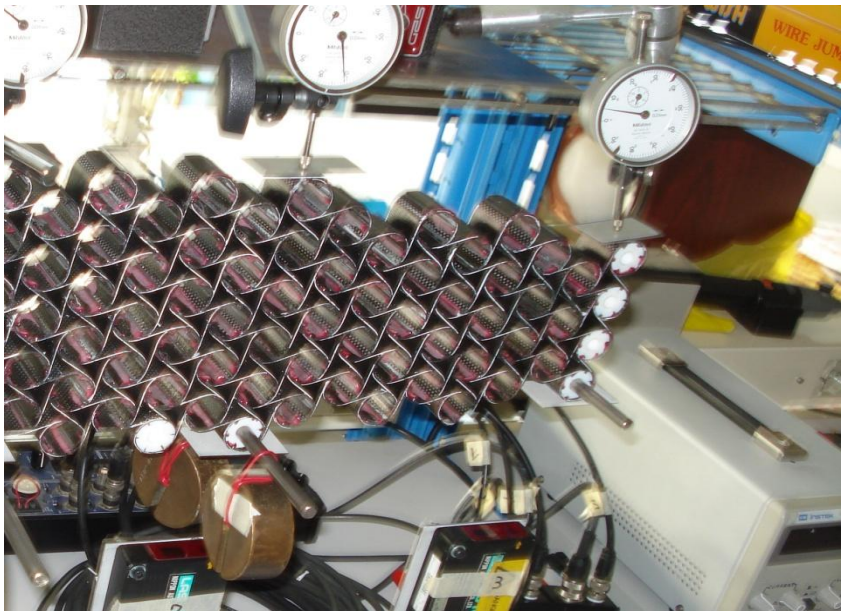

Figure 6.14 – Loads sustained on the middle node for testing

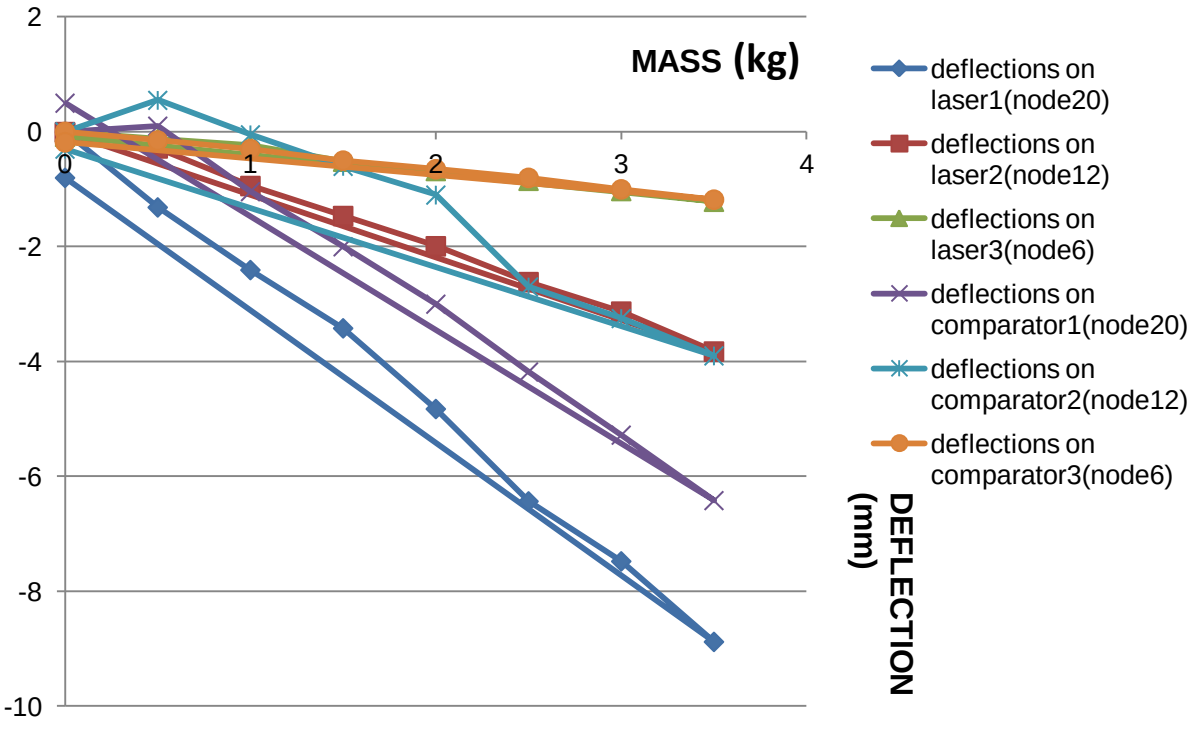

Figure 6.15 – Load versus deflection for test number 1, test type 3

6.3 Numerical and Experimental Correlation

A finite element model of the chiral rib in the testing configuration has been developed in order to obtain a correlation with the experimental tests. Both of the load conditions (concentrated and distributed load) were reproduced in the model. Test type 1 and 3 represent concentrated loading while test type 2 represents the distributed loading. The FE model of the rib is similar to the one employed in the FE model of the technological demonstrator except for the loading configuration and the constraints. Regarding the constraints, the first five nodes were fixed to the ground; therefore they are unable to rotate, reproducing the experimental conditions as it is shown in the Figure 6.16. In the testing however the five nodes that were fixed to the test apparatus have a very small rotation rate preventing failure of the rib during the loading. During the testing, the loads have been applied in the vertical direction by putting weights to the bars attached to the lower nodes of the rib. In the numerical modeling vertical forces, corresponding to the weights employed in the experimental testing were applied to the selected lower nodes (one node for the concentrated load testing i.e. test type 1 and 3, three nodes for the distributed load testing). The displacements of the numerical models and the experimental tests were then compared to verify the correlation. The thickness of the ligaments has been changed by some percentage to see if the numerical model is close to the real life conditions. It was seen that there is good correlation by increasing the thickness of the ligaments about 10-15%.

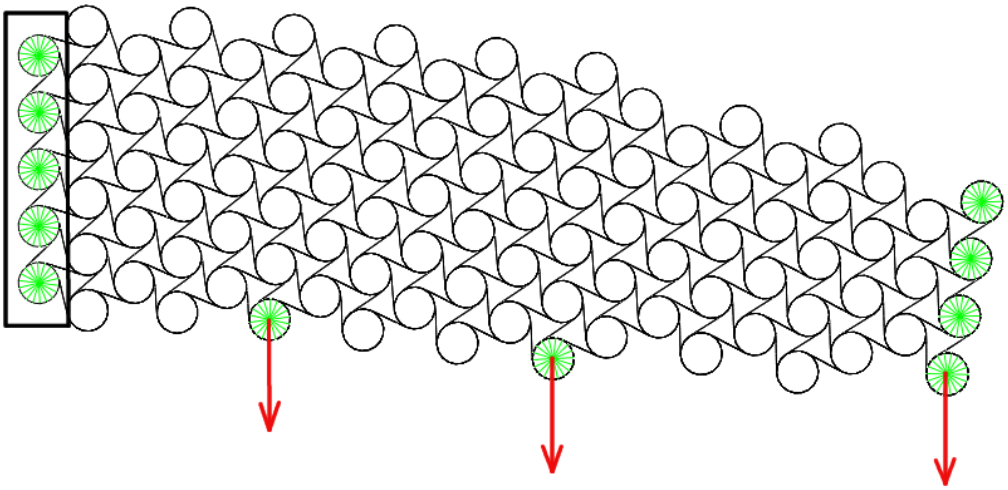

Figure 6.16 – FE model of the static testing of the rib

Comparison between the testing and numerical analysis is given as a graph in the Figure 6.17 for test type 1, test number 5. Comparator measurements are not given in this graph due to the fact that difference between the readings of lasers and comparators are minimal. It can be seen from the graph that as deflection increases, the inconsistency between the numerical and experimental results increases too. In the Table 6.6 numerical – experimental correlation is given for this type of testing as the values of the slopes of the curves. When the thicknesses of the ligaments were

increased by 15%, the numerical values became closer to the experimental values. Numerical – experimental correlations are given in Figure 6.18 (a), (b) and (c) for test type 2; the first graph was prepared by putting the deflection levels of experimental results with the original numerical results [36]. As explained before, comparator 3 (node 20) did not measure in the 11th step by removing the needle of the device, so the deflection value in this step is '0'; so a V – notch type deviation from the curve was observed. In the numerical analysis thickness of the rib has been increased by 10% and 15% respectively to see if the numerical results were in close relation with the experimental measurements and the curves for numerical and experimental findings fit with each other. It was seen that when the thickness was increased up to 15% for the numerical analysis, the curves for the numerical results became close to the curves of the experimental measurements.

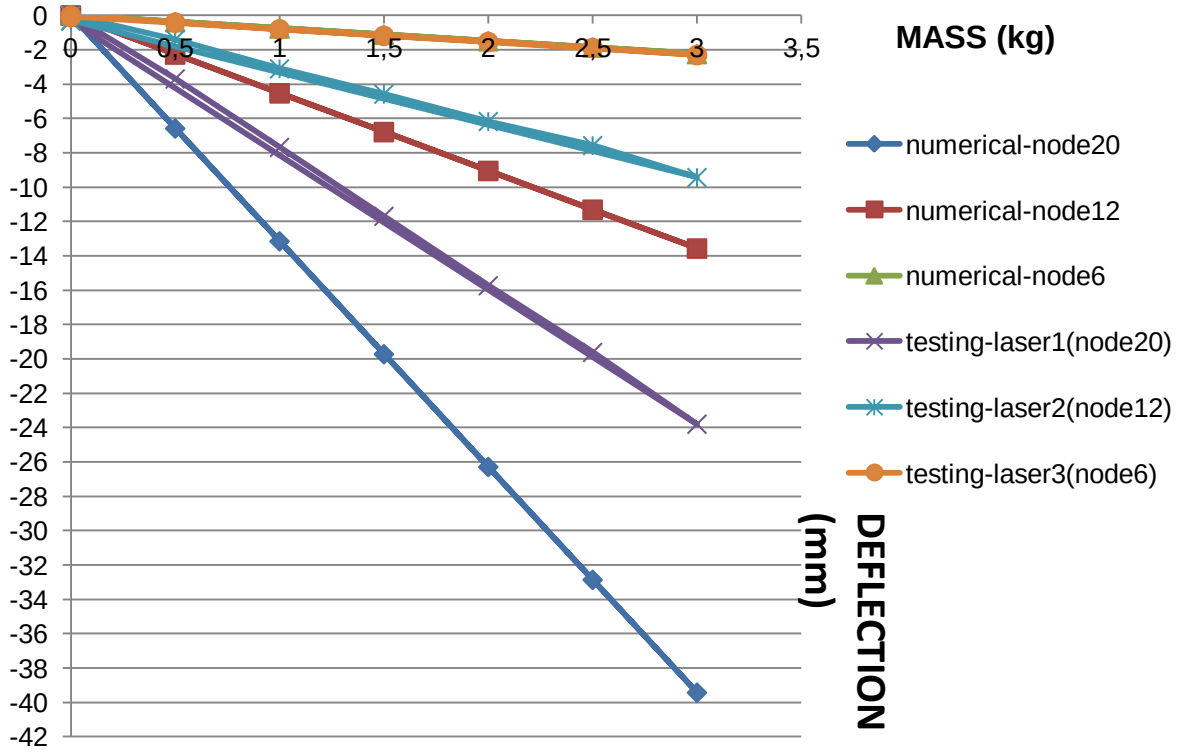

Figure 6.17 – Comparison of test results with the numerical analysis for test type 1

In the Figure 6.19, comparison of test results with the numerical analysis for test type 3 could be observed. The numerical analysis have been realized for 1 kg of loading and since the behavior is linear for the concentrated load testing, deflection results for higher loading were obtained by multiplication of the resultant deflection of 1 kg loading with the corresponding load. In the Table 6.7 numerical – experimental correlation is given for this type of testing as the values of the slopes of the curves. Thicknesses were increased by 10% and 15% for the numerical analysis to see the compliancy of the numerical findings with the experimental results. From the Table 6.7 it can be seen that for the deflection on node number 6, original numerical finding has the closest value to the experimental result while for the deflection on node number 12, 15% increase in the

thickness gives the closest value of the numerical findings to the experimental data and for the deflection on node number 20, 10% increase of the thickness in the numerical analysis gave the closest value to the experimental results.

Table 6.6 – Numerical – experimental correlation for test type 1

	LOAD ON LAST NODE			
	EXPERIMENTAL	**NUMERICAL ORIGINAL**	**NUMERICAL +10%**	**NUMERICAL +15%**
ROOT	-0,721	-0,745	-0,564	-0,496
MIDDLE	-2,889	-4,528	-3,422	-3,003
TIP	-8,631	-13,15	-9,93	-8,714

Table 6.7 – Numerical – experimental correlation for test type 3

	LOAD ON MIDDLE NODE			
	EXPERIMENTAL	**NUMERICAL ORIGINAL**	**NUMERICAL +10%**	**NUMERICAL +15%**
ROOT	-0,347	-0,339	-0,257	-0,225
MIDDLE	-1,043	-1,515	-1,145	-1,005
TIP	-2,537	-2,997	-2,265	-1,989

6.4 Preliminary Definition and Technology for Skin, Leading/Trailing Edges and Connectors

The maximum vertical deflection obtained by the two – dimensional model can be easily defined as an indicator of the rigidity per unit of width of the strip:

$$K'_{airfoil} = \frac{dK_{airfoil}}{dw_{airfoil}} = \frac{1}{w_{airfoil}} \frac{l_{airfoil}\, w_{airfoil}}{\delta_{max}} \qquad 6.1$$

Where $w_{airfoil}$, $l_{airfoil}$, and δ_{max} are width, applied load and the maximum vertical deflection respectively. The total aerodynamic load acting on the rib (taking into account the area of influence) and expressed as:

$$L_{rib} = l_{airfoil} b_{rib} \qquad 6.2$$

Where b_{rib} indicates precisely the dimension of the width where the rib collects loads. Therefore it appears that, to achieve the same maximum deflection, the stiffness per unit width must be equal to:

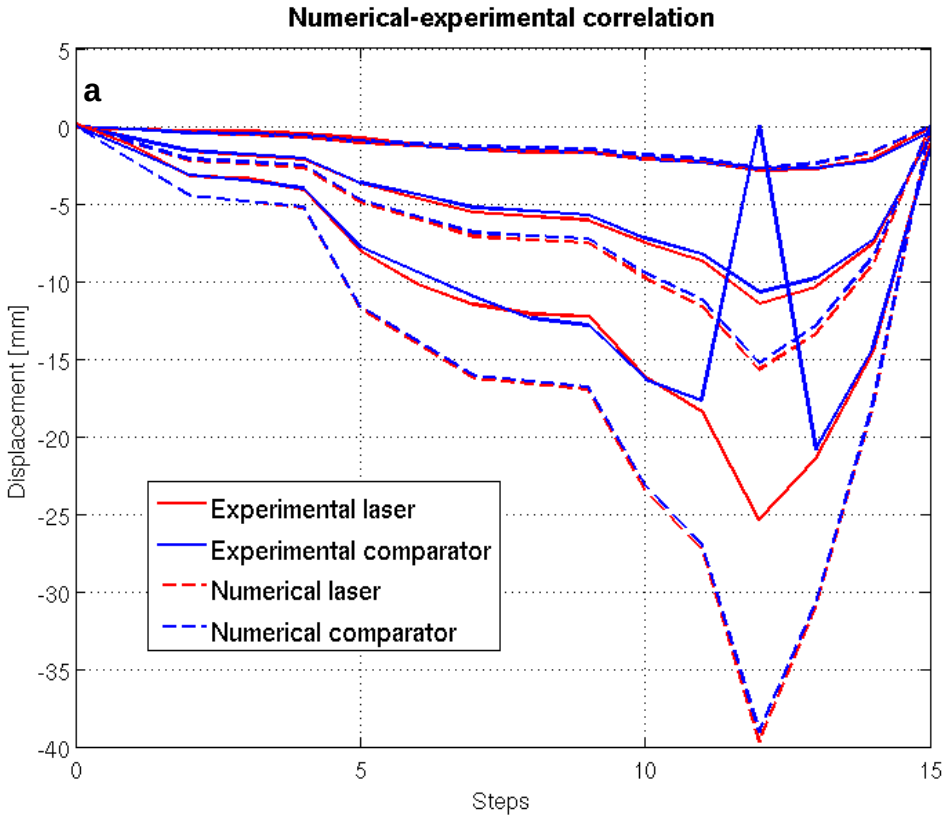
Numerical-experimental correlation
a
Displacement [mm]
Steps
Experimental laser
Experimental comparator
Numerical laser
Numerical comparator

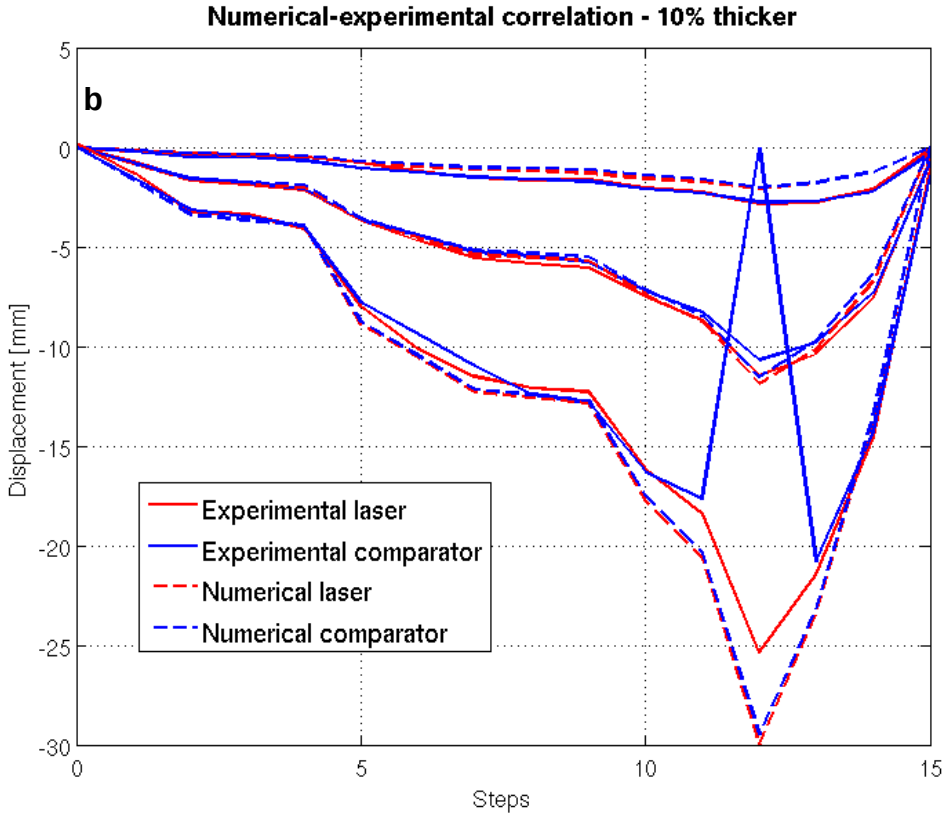
Numerical-experimental correlation - 10% thicker
b
Displacement [mm]
Steps
Experimental laser
Experimental comparator
Numerical laser
Numerical comparator

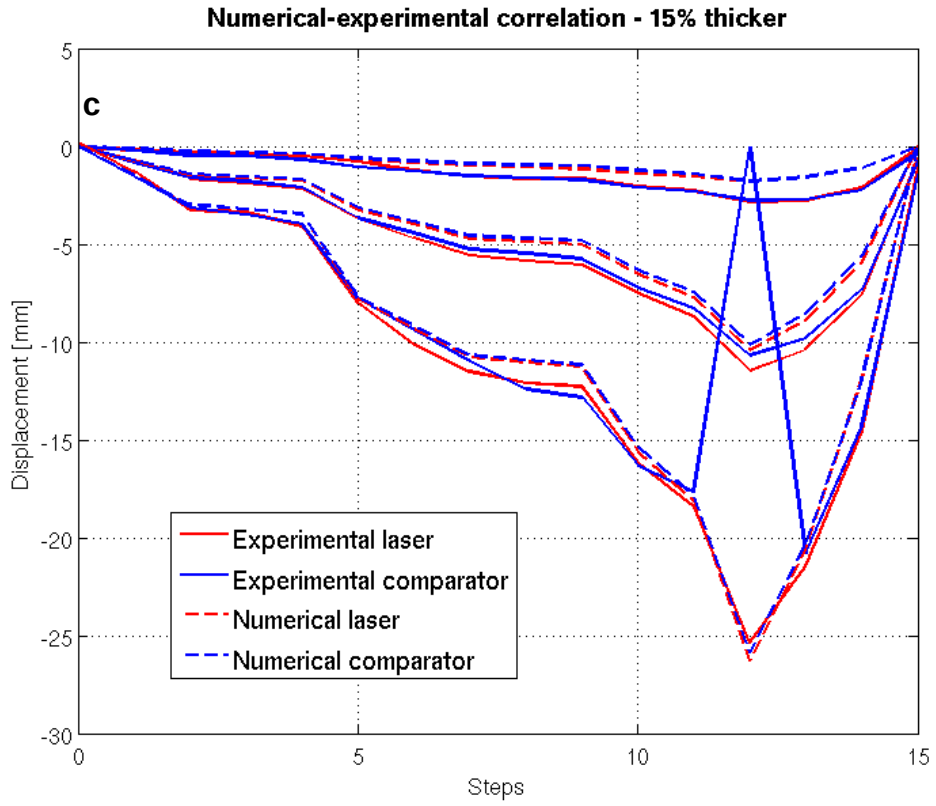

Figure 6.18 – Numerical – experimental correlations for test type 2
(a) Displacement versus test steps for experimental and original numerical values
(b) Displacement versus test steps for experimental and 10% thicker numerical values
(c) Displacement versus test steps for experimental and 15% thicker numerical values

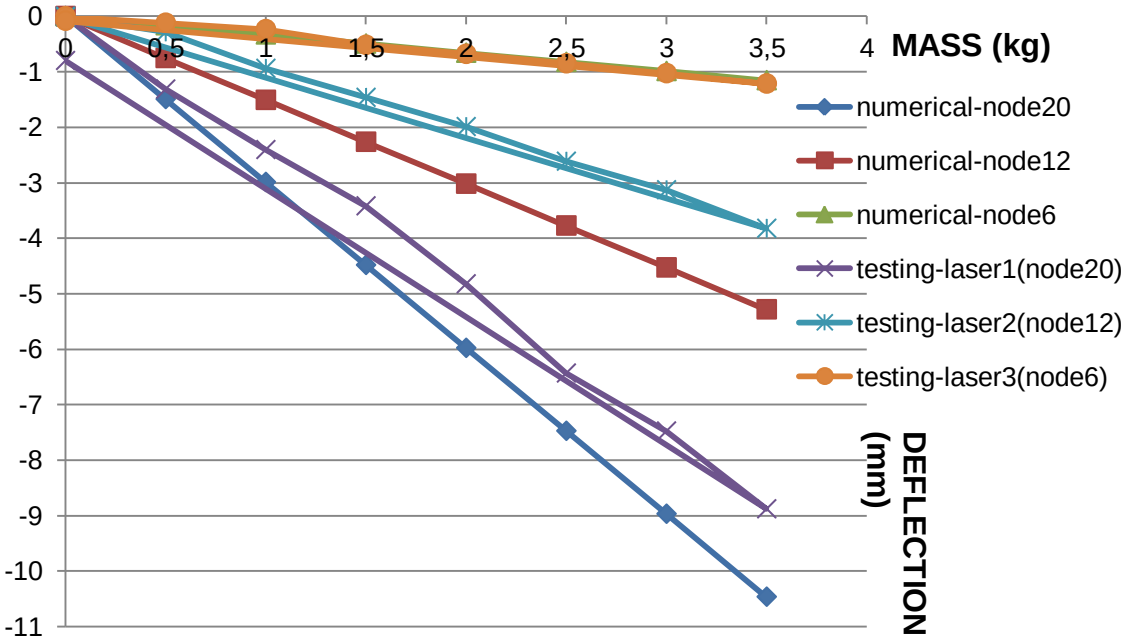

Figure 6.19 – Comparison of test results with the numerical analysis for test type 3

$K'_{rib} = K'_{airfoil}\frac{b_{rib}}{w_{rib}}$ 6.3

Several configurations have been taken into consideration during the design of the morphing wing; number of the ribs changing from three to four, different ply thicknesses (5 and 7 plies) and width of the ribs to be used. The wideness of the ribs is varying from 15, 25 and 30 mm for small ribs to 30, 50 and 60 mm for large ribs. A trade – off analysis was carried out to find the best configuration based on these parameters. According to this trade – off analysis, the best configuration is a morphing wing with three ribs which have 7- plies thickness and 25 – 50 – 25 mm width. This decision was given not only for the rigidity and expected deflection rates but also the ease of technological process. The following table (Table 6.8) indicates the configurations which were tried for the trade – off analysis. The Figure 6.20 shows FE models of the three ribs and four ribs configurations of the technological demonstrator.

Table 6.8 – Trade – off analysis for the rib configurations

Configuration no:	**Rib configuration**		**Rigidity (dimensionless)**	**Expected deflection(mm)**
	Width(mm) of the ribs and their order	**Number of plies**		
1	15 30 30 15	7	1914	21.2
2	30 60 60 30	5	4260	23.6
3	25 50 25	7	1990	19.9
4	25 50 50 25	5	4380	29.2
5	30 60 30	7	1914	15.95

Leading and Trailing Edges that make up the nose and tail of the technological demonstrator help to preserve the shape of the profile but are not of great importance from the structural point of view, and therefore they must be as light as possible without neglecting the fact that they should be able to stabilize the ribs. The material chosen to fill the interior section of the LE/TE is Rohacell. This material is a rigid polymer foam of low density that responds well to the requirements and has the advantage of being easily machined with the tool, in addition to being convenient for technological processes with composite prepreg and RTM techniques up to 130º C and pressure of 0.3 MPa. The mechanical characteristics of different types of Rohacell are reported in Table 6.9.

The ribs would be developed with chiral CFRP structures exploiting the same manufacturing technology used for the chiral unit that was described before. The widths chosen for the ribs which will be inserted in the demonstrator are 25 mm and 50 mm as shown in Figure 6.21 (a) and (b), the rib that is positioned in the central zone of the morphing wing will be wider since it will have to sustain bigger portion of the load transmitted from skin while the 25 mm ribs will be located at the edges.

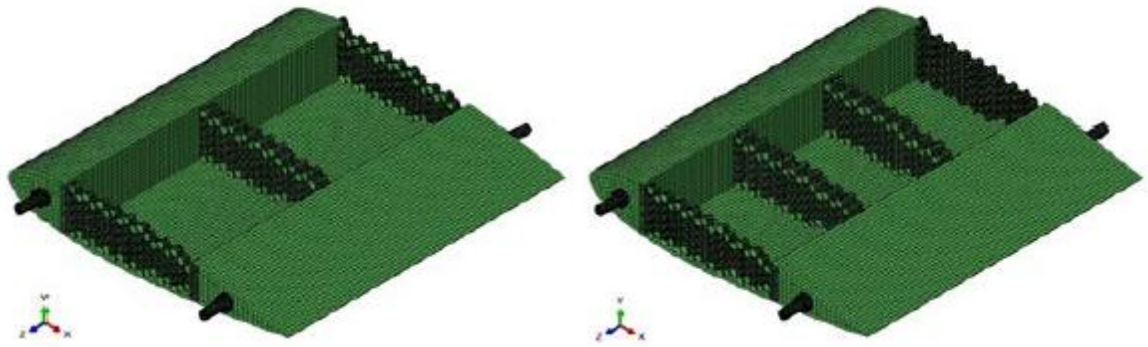

Figure 6.20 – Finite element models of the technological demonstrator

Table 6.9 – Mechanical properties of Rohacell

	ρ	ROHACELL 31	ROHACELL 51	ROHACELL 71	ROHACELL 110
Density	[kg/m^3]	32	52	75	110
Compressive strength	[Mpa]	0,4	0,9	1,5	3
Tensile strength	[Mpa]	1	1,9	2,8	3,5
Shear strength	[Mpa]	0,4	0,8	1,3	2,4
Elastic modulus	[Mpa]	36	70	92	160
Shear modulus	[Mpa]	13	19	29	50
Strain at break	%	3	3	3	3

The flexible skin which is considered to be used for the technological demonstrator consists of a laminated corrugated composite material as shown in Figure 6.22. The corrugated skin will be closed on the top like a lid to comply with the aerodynamic requirements. The geometrical and mechanical characteristics of this configuration have been calibrated in accordance with the requirements and a technological process has been developed for the production of corrugated structure. Table 6.10 indicates the requirements of the skin. Several designs have been studied for the realization of the flexible skin. Some early designs were considered to use Y or S shaped scales with a silicon layer atop. Afterwards, corrugated geometries have been proposed to fulfill the requirements for the skin. The first corrugated design was based on the trapezoidal geometry with a silicon layer at the top. Another design proposal was considered to use a corrugated structure with a carbon – plate reinforced layer to be placed on the top of the corrugated structure. The final geometry however would be trapezoidal corrugated structure with a closed surface. Experimentally measured mechanical properties of the corrugated structure are given in Table 6.11 [37].
Regarding the realization of the connection between the technological demonstrator and the wind tunnel is by using four steel pins inserted inside the ROHACELL which constitutes the Leading/Trailing Edge. The steel pins could be observed in Figure 6.20.

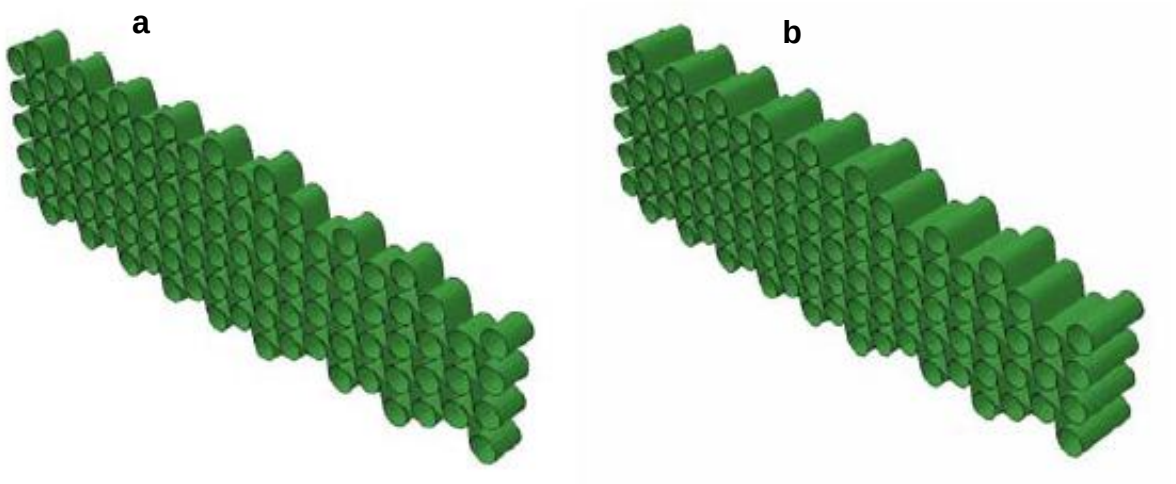

Figure 6.21 – Ribs utilized for the technological demonstrator (a) 25 mm wide rib (b) 50 mm wide rib

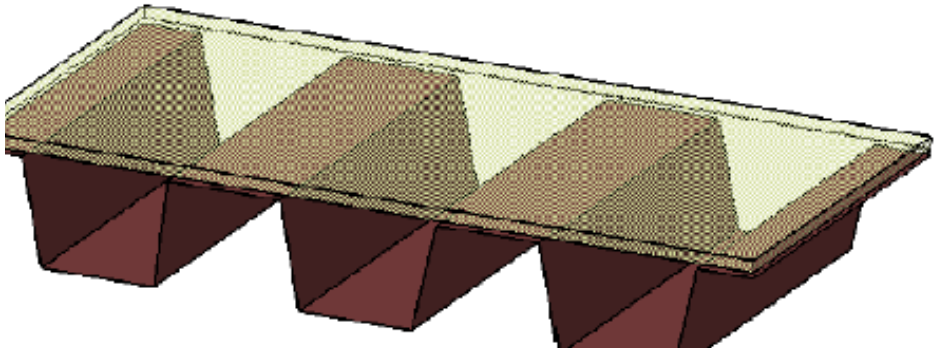

Figure 6.22 – Preliminary skin with a corrugated structure

Table 6.10 – Minimum requirements for the rigidity of the skin

Chordwise axial stiffness, A_{22}	30 N/mm
Chordwise flexural stiffness, D_{22}	500 – 600 Nmm
Spanwise flexural stiffness, D_{11}	10^5 – 10^6 Nmm

Table 6.11 – Experimentally measured mechanical properties for the corrugated composite

Longitudinal tensile modulus	E_L(GPa)	4.26
Transverse tensile modulus	E_T (MPa)	0.92
Longitudinal bending modulus	D_L (Nm)	14.3
Transverse bending modulus	D_T (Nm)	0.0021

A key aspect of the technological demonstrator is the definition of the connections between the different parts of the structure, in order to obtain a kinematic behavior and a transmission of forces to be convenient and consistent with the adopted realization. To connect the leading/trailing edges with the ribs that meet the requirements of the technological demonstrator it is necessary to add the components to the morphing wing. In particular, the constraints must be such that the front and rear nodes of each rib would be permitted a pure rotation about their out – of – plane axis in order to avoid stress concentrations.
Connection between ribs and the skin; for the connection between the ribs and the corrugated skin in the proposal of the preliminary draft is to take advantage of a technique similar to that used in the coupling between the ribs and solid box of leading/trailing edges. In fact, also in this case use of bushings involves allowing the free rotation of certain elements of the structure. In particular, the bushings are inserted in both the outer nodes of the chiral network (where the loads are collected from the skin) and in the gorges of the corrugated structure. The connection is then performed by means of the insertion of hinges in specific shapes and dimensions to be able to fix the bushings located on both sides and positioned in order to close each node on the two sides of the rib. A sketch of the solution described above is shown in Figure 6.23.

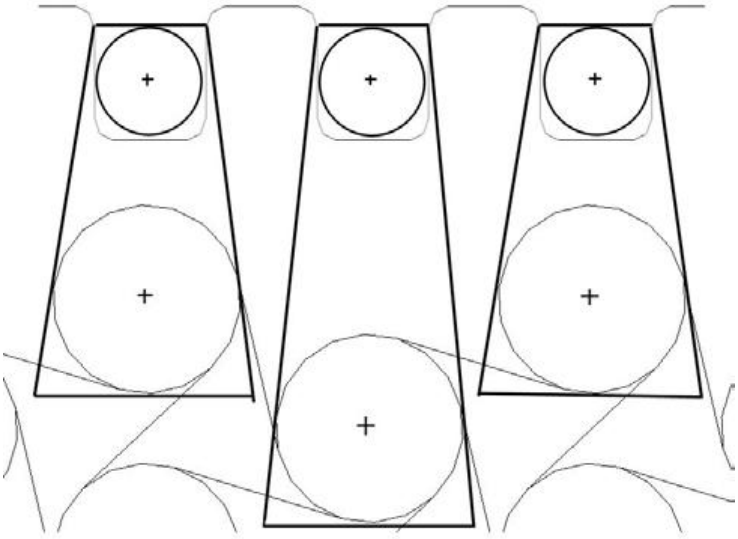

Figure 6.23 – Link between the rib and the skin

7 Conclusions and Recommendations

The chiral units were produced based on the optimized geometry. In the optimization, the geometrical parameters of the chiral geometry (r and L) yielded smaller values than the previous configuration, a miniaturized chiral structure has been obtained with the new optimized geometry. Static testing has been carried out to assess the mechanical response, numerical analysis were accomplished to compare with the experimental data. Based on the success of the miniaturized chiral unit, design and production of the rib was initiated. Finite Element Analysis (FEA) were carried out to find the best solution and production of the rib has been started based on the results obtained during the FEA. Several manufacturing methods have been employed for the production of a rib composed of auxetic chiral units. Amongst them are ribs made of ABS plastics by using rapid prototyping or additive layer manufacturing. The obtained rib was made by employing vacuum bag method in which prepreg CFRP material was used. The curing process was realized by autoclave heat – pressure cycle. Instead of assembling nodes and ligaments separately, nodes were obtained by superimposing six ligaments that reaches to the same cylinder of the assembly mold. The produced rib was seen as more rigid than the anticipated result. The obtained deflection in the vertical direction was less than the expected deflection. This could be due to the material non – linearities which were not taken into account during the FE analysis but instead only geometrical non – linearities were included. For the desired deflection levels; the nodes should be able to rotate around their out – of – plane axis freely but due to the relatively smaller geometrical ratios – L/r was 75/18 = 4.1 in the bigger chiral unit and in the new configuration this ratio became L/r = 19.3/10.3 = 1.8 – the rotation was minimal. The remedy to this problem is either bringing this ratio to a reasonable value or decreasing the ply thickness where the bending moment decreases/increases with the cube of the thickness of the ligament. Instead of 5 – plies thickness for the produced rib, a rib laminated with 3 or even 2 ply ligaments could be a solution for this problem.

The production method in the recent technology is based on the vacuum bag of prepreg composite materials. In order to obtain the final rib geometry, two molds are needed; the first mold for the production of the ligaments and other mold for the assembly of the produced ligaments to form the rib. For the mass production of the ribs however, a distinct production technology could be employed such as RTM or infusion.

The rib is the main part of the morphing wing along with the skin. The first important step in obtaining the morphing wing is perhaps producing the. In the recent work, a rib has been produced with an optimized geometry. For the proposed morphing wing, which has a 50 cm wide span, two ribs of 25 mm deep are needed. In the chordwise direction, each rib has a length 1 m. The second step for obtaining the morphing wing would be the production of the corrugated skin. The silicon made skin could be a preliminary solution to the morphing wing in the laboratory testing but in the real life operation, flexible skin with better mechanical properties and self healing features would be needed for the qualification of such a morphing wing. For an active wing smart materials/systems are required. In that sense, SMPs are promising candidates to convert the passive morphing wing to the active morphing wing. As it is the case for a passive wing, self healing feature is also required for an active morphing wing utilizing SMP made flexible skin. This skin could be stimulated by means of embedded wires inside the SMP made skin. Some laboratory studies have already proven that this

method of stimulating the SMP material is a convenient way to employ but in the real life conditions more reliable technology to embed the wires is needed. There are also other methods to stimulate the SMPs but stimulating these polymeric materials by means of heating seems the most reliable method. Developing a heat transfer system for the SMP made skin with less heat loss (dissipation is a major problem during heating of the SMP material) would be a remedy for a more reliable heating system. Instead of embedding the wires to the host material, an array of heating elements could be mounted underside of the SMP material. Other methods of stimulation by heating through different means such as light, magnet or laser could also be thought. After its glass transition temperature, an SMP material loses its mechanical properties very considerably. Some methods to strengthen the SMP materials are already underway. SMPs could be reinforced by using high modulus organic or inorganic fillers such as carbon nanotube/nanofiber, nano SiC, carbon block, etc. Instead of utilizing SMP as bare material for the flexible skin, SMP could be used as the matrix material for a composite material. In this way SMP composites are introduced into the market. Polystyrene or polyurethane based SMP could be used as the matrix material and carbon or glass fiber could be used as reinforcement to form the SMP composites.

During flight a morphing wing needs to demonstrate repeated shape changes and an SPM made flexible skin is required to keep its memory effect in the long term. In order to qualify an SMP made skin, performing experiments are needed to study the repeatability of SMP memory effect. Thermo – mechanical effects on response characteristics of SMP materials are not well understood; thermo – mechanical testing should be carried out. A thermo – mechanical fatigue testing will help to understand the properties of these materials in a wide range of temperatures.

The transition time is also very important to convert the material from solid state to soft state and vice – versa. For the laboratory research, some minutes elapse for the transition of SMP material but in the real life operations the time required will be seconds not minutes. The flexible skin should be transitioned from one state to another in seconds.

Other smart materials like Electro Active Polymers (EAPs) such as polyvinylidene fluoride (PVDF) or Macro Fiber Composites (MFC) are also promising candidates for flexible skin. PVDF material is the most studied and utilized piezoelectric polymer. They change their shape or size when stimulated by an electric field. EAP materials can be easily manufactured into various shapes due to the ease in processing many polymeric materials, making them very versatile materials. They have high fracture toughness, large actuation strain and inherent vibration damping that makes them suitable for the application as flexible skin. Very recently, MFCs started coming into market. They are a kind of piezoelectric materials that offer high actuation authority and sensing over a wide range of frequencies. A Macro Fiber Composite is a type of piezoelectric device that offers structural flexibility and high actuation authority. The use of MFCs become feasible in small platforms such as unmanned air vehicles or micro air vehicles.

In the design of the technological demonstrator, flexible skin is housed by the Leading and Trailing Edges. The material for the LE/TE are planned to be GFRP. This material could be laminated over a mandrel and a flexible mold could be needed to exert pressure on the surfaces of the material during the autoclave. To simplify the process, dry material instead of peel ply could be utilized for the lamination over the mandrel.

After the material is laminated, resin will be applied by a brush as the matrix material before it goes inside the autoclave. Leading and Trailing Edges have also connections with the ribs. The ribs are connected to the corrugated flexible skin by means of pin – hinge mechanisms which can rotate around their axis. LE and TE are filled with a foam material to provide shear and pressure resistance. The foam material thought to be utilized is called Rohacell and this material offers high strength/weight ratio.
After the production of all components, the next phase for the realization of the technological demonstrator would be the attachment of two ribs to the Leading and Trailing Edges. The ribs should also be connected to the skin through pin – hinge mechanism. The last experimental assignment will be the wind tunnel testing of the technological demonstrator. Technical infrastructure of the wind tunnel allows the velocity of the air to be 50 m/s and the morphing wing is required to withstand to the aerodynamic loads generated by the blowing air. The flexible skin will have pre – stressed corrugated geometry to function as the passive wing.

References

[1] Gillanders A.M., Kerr S., Martin T.J., Determination of prepreg tack, International Journal of Adhesion and Adhesives, January 1981, Volume 1, Issue 3, Pages 125 – 134

[2] Baier Horst, Mueller Uwe C. and Rapp Stephan, Optical fiber sensor networks in smart structures, Proc. SPIE, 2008

[3] Kreuzer Manfred, Strain measurement with Fiber Bragg Grating Sensors, HBM Company

[4] Leng J. S., Asundi A., Non – destructive evaluation of smart materials by using extrinsic Fabry – Perot interferometric and Fiber Grating Sensors, NDT&E International 35 (2002), 273 – 276

[5] Leng et al., Shape memory polymers and their composites: Stimulus methods and applications, Progress in Materials Science, 56 (2011), 1077 – 1135

[6] Ratna Debdatta, Kocsis J. Karger, Recent advances in shape memory polymers and composites: a review, J. Mater Sci (2008) 43:254 – 269

[7] Gern Frank H., Inman Daniel J. and Kapania Rakesh K., Structural and aeroelastic modeling of general planform wings with morphing airfoils, 2002

[8] Bettini Paolo et al., Composite chiral structures for morphing airfoils: Numerical analyses and development of a manufacturing process, Composites Part B, 2010

[9] Sofla A.Y.N. et al., Shape morphing of aircraft wing: Status and challenges, Materials and Design, 2009

[10] Reich Gregory and Sanders Brian, Introduction to morphing aircraft research, Journal of Aircraft, 2007

[11] M. Frecker D. S. Ramrakhyani, G. A. Lesieutre and S. Bharti. Aircraft structural morphing using tendon-actuated compliant cellular trusses. Journal of Aircraft, 42(6), 941–952, Nov – Dic 2005

[12] Gibson Rauscher Scott, Testing and analysis of shape memory polymers for morphing aircraft skin application, MSc Thesis, University of Pittsburgh, 2006

[13] Gross Korey Edward, Mechanical characterization of shape memory polymers to assess candidacy as morphing aircraft skin, MSc Thesis, University of Pittsburgh, 2006

[14] Jee Soo Chan, Development of morphing aircraft structure using SMP, MSc Thesis, Air Force Institute of Technology, 2010

[15] Megson T.H.G., Aircraft structures for engineering students, Butterworth – Heinemann, Third edition, 1999

[16] http://www.ausairpower.net/AADR-FBW-CCV.html

[17] Bettini P. et al., Carbon fiber reinforced smart laminates with embedded SMA actuators – part 1: Embedding techniques and interface analysis, Journal of materials engineering and performance, 2008

[18] L. Sun , W.M. Huang , Z. Ding , Y. Zhao, C.C. Wang, H. Purnawali , C. Tang, Stimulus-responsive shape memory materials: A review, Materials and Design 33 (2012) 577 – 640

[19] Huang WM, Ding Z, Wang CC, Wei J, Zhao Y, Purnawali H. Shape memory materials. Mater Today 2010; 13 (7 – 8):54 – 61

[20] Klinger D, Landfester K. Photo-sensitive PMMA microgels: light-triggered swelling and degradation. Soft Matter 2010;7(4):1426 – 40

[21] Sun L, Huang WM. Wet to shrink: An approach to realize negative expansion upon wetting. Adv Compos Mater 2009; 18(2): 95 – 103
[22] Leng et al., Shape memory polymers and their composites: Stimulus methods and applications, Progress in Materials Science, 56 (2011), 1077 – 1135
[23] Yin et al., Deformation analysis of shape memory polymer for morphing wing skin under airflow, Front.Mech.Eng.China, 2009, 4(4):447 – 449
[24] Bornengo D., Scarpa F., and Remillat C., Evaluation of hexagonal chiral structure for morphing airfoil concept, Proc. IMechE Vol. 219 Part G: J. Aerospace Engineering, 2005
[25] Hassan M.R., Scarpa F., Ruzzene M. , Mohammed N.A., Smart shape memory alloy chiral honeycomb, Materials Science and Engineering A 481 – 482 (2008) 654 – 657
[26] Sypeck David J., Cellular Truss Core Sandwich Structures, Applied Composite Materials (2005) 12: 229 – 246, 2005
[27] Sypeck, D. J., Wadley, H. N. G., Bart – Smith, H., Koehler, S. and Evans, A. G., Structure and Deformation of Aluminum Foams Through Computed Tomography, in Review of Progress in Quantitative Nondestructive Evaluation 17, D. O. Thompson and D. E. Chimenti (eds.), Plenum Press, New York, 1998, pp. 1443 – 1450
[28] Prall D., Lakes R., Properties of a chiral honeycomb with a Poisson's ratio of -1, Int. J. Mech. Sci. 39 (1996) 305 – 314
[29] Bettini P., Airoldi A., Sala G., Di Landro L., Ruzzene M. and Spadoni A., Composite chiral structures for morphing airfoils: Numerical analyses and development of a manufacturing process, In Composites: Part B, 2009
[30] Airoldi Alessandro et al., Design of a Morphing Wing Using a Composite Chiral Structure, RAeS 2nd Structural and Design Conference, London, UK, October 26 – 28, 2010
[31] Foston Marvin and Adams R.C., Elastomeric tooling, Lockheed – Georgia Company
[32] Seal CC90 ET445 and Seal EE48 REM technical data sheet, Saati Composites
[33] 3M Scotch – Weld Structural adhesive film AF 163-2K technical data sheet
[34] Oktem Mehmet Fatih et al., Structural design of a technological demonstrator of a morphing wing, 6th Ankara International Aerospace Conference (AIAC – 2011), 14-16 September, 2011 - METU, Ankara – Turkey
[35] Crespi Marco, Multidisciplinary optimization of an airfoil with a morphing capacity, MSc Thesis, Politecnico di Milano, 2009
[36] Bolgiani Luca, Experimental studies and numerical analysis for the design of a wing structure with morphing capability, MSc Thesis, Politecnico di Milano, 2011
[37] Borlandelli Elena, Corrugated composite laminates for morphing structures: design and technological development, MSc Thesis, Politecnico di Milano, 2011